creative commons
COMMONS DEED

저작자표시-비영리 2.0 대한민국

이용자는 아래의 조건을 따르는 경우에 한하여 자유롭게

- 이 저작물을 복제, 배포, 전송, 전시, 공연 및 방송할 수 있습니다.
- 이차적 저작물을 작성할 수 있습니다.

다음과 같은 조건을 따라야 합니다:

저작자표시. 귀하는 원저작자를 표시하여야 합니다.

비영리. 귀하는 이 저작물을 영리 목적으로 이용할 수 없습니다.

- 귀하는, 이 저작물의 재이용이나 배포의 경우, 이 저작물에 적용된 이용허락조건을 명확하게 나타내어야 합니다.
- 저작권자로부터 별도의 허가를 받으면 이러한 조건들은 적용되지 않습니다.

저작권법에 따른 이용자의 권리는 위의 내용에 의하여 영향을 받지 않습니다.

이것은 이용허락규약(Legal Code)을 이해하기 쉽게 요약한 것입니다.

Disclaimer

dCollection

[UCI]I804:48009-200000171109

Doctor of Philosophy

The first-principles study on phononic thermal transport properties in two-dimensional materials and its applications in thermoelectric and thermal management

The Graduate School

of the University of Ulsan

Department of Physics

Aamir Shafique

The first-principles study on phononic thermal transport properties in two-dimensional materials and its applications in thermoelectric and thermal management

Supervisor: Prof. Young-Han Shin

This dissertation is submitted to University of Ulsan in partial fulfillment of

the requirements for the degree of

Doctor of Philosophy in physics

by

Aamir Shafique

Department of Physics

University of Ulsan

February, 2019

University of Ulsan

Department of Physics

This dissertation, “The first-principles study on phononic thermal transport in two-dimensional materials and its applications in thermoelectric and thermal management” is hereby approved in partial fulfillment of the requirements for the degree of Doctor of Philosophy in physics.

Sunglae Cho

Committee Chair: Prof. Sung Lae Cho
Department of Physics, University of Ulsan

External Examiner: Prof. Ji Hoon Shim
Department of Chemistry & Physics,
Division of Advanced Nuclear Engineering,
Pohang University of Science and Technology

Kim Yong Soo

Examiner: Prof. Yong Soo Kim
Department of Physics, University of Ulsan

Examiner: Dr. Hye Jung Kim
Department of Physics, University of Ulsan

Young Han Shin

Supervisor: Prof. Young-Han Shin
Department of Physics, University of Ulsan

Dedicated to my loving parents

Declaration

I hereby declare that except where specific reference is made to the work of others, the contents of this dissertation are original and have not been submitted in whole or in part for consideration for any other degree or qualification in this, or any other university.

Aamir Shafique
December 17, 2018

Acknowledgements

It is surely a great feeling to finish my thesis, but it definitely would not have been possible without the assistance, patience, guidance, and support of many people. This thesis, as well as the time I spent here, has been a great learning experience for me and I would like to acknowledge all the persons who have helped me during this time.

First, and foremost I am grateful to my thesis supervisor Prof. Young-Han Shin for his substantial support, guidance, and granting me the opportunity to work in the Multiscale Materials Modeling Laboratory (M3L) at the department of physics, University of Ulsan. His tireless efforts in helping me become a better researcher. I am also grateful to all other members of the M3L and special thanks to Dr. Hye Jung Kim for sharing her knowledge and helping me to expand my research capabilities. I am also thankful to BrainKorea21 (BK21) Plus for the funding to carry out my thesis work.

Last but not least I wish to express my thanks to my dear family and my friends for their unconditional support and love through the years.

Abstract

The lattice thermal conductivity is an intrinsic and essential transport property that plays an important role in thermoelectric devices and thermal management of electronics. We use density functional theory (DFT) combined phonon Boltzmann transport equation (PBTE) to predict the lattice thermal conductivity of two-dimensional materials. The second and third order derivatives of the energy with respect to the atomic position are the most important ingredients in the calculation of lattice thermal conductivity, and we obtain these derivatives from DFT through finite differences method. The approach is applied to compute phononic thermal transport in the variety of two-dimensional material.

We studied the electronic structures, Seebeck coefficients, electrical conductivities, lattice thermal conductivities, and figures of merit of two-dimensional IV–VI compounds, which showed that the thermoelectric performance of these two-dimensional compounds is improved in comparison to their bulk phases. High figures of merit (ZT) are predicted for SnSe (ZT = 2.63, 2.46), SnS (ZT = 1.75, 1.88), GeSe (ZT = 1.99, 1.73), and GeS (ZT = 1.85, 1.29) at 700 K along armchair and zigzag directions, respectively. We also calculate the lattice thermal conductivity of the monolayer SnX_2 and monolayer InX and It is found that the lattice thermal conductivity of these monolayers at room temperature is very low, which is attributed to the heavy atomic masses of Sn, In, S, Se, and Te and its strong phonon anharmonicity.

The strain is a handy and useful tool to enhance the performance of the semiconducting devices. We find that the lattice thermal conductivity is reduced approximately 2.5 times at 8% tensile strain for the two-dimensional 2H-$MoTe_2$ contrary to graphene, germanene, silicene, germanene, and Penta-SiC_2. The reduction in lattice thermal conductivity attributes to the reduction in the phonon group velocity, the phonon heat capacity, and the phonon scattering time.

Heat removal has become a significant challenge in the miniaturization of electronic devices, especially in power electronics, so semiconducting materials with suitable bandgap and high lattice thermal conductivity are highly desired. Here, we theoretical predict an ultra-high and anisotropic lattice thermal conductivity in the monolayer BC_2N. The predicted values of lattice thermal conductivity at room-temperature are 893.90 W/mK and 1275.79 W/mK along armchair and zigzag directions, respectively. These values are probably the highest that have

ever been reported for the two-dimensional semiconducting materials.

Contents

Contents **xi**

List of Figures **xv**

List of Tables **xxi**

1 Introduction **1**
- 1.1 Motivation and objective 1
- 1.2 A brief history of the phonon thermal transport in the two-dimensional materials 2
  - 1.2.1 Graphene 2
  - 1.2.2 Silicene 3
  - 1.2.3 Monolayer MoS_2 4
- 1.3 Thermoelectrics 6
  - 1.3.1 Thermoelectric effects 6
  - 1.3.2 Figure of merit 7
- 1.4 Strain effect 8
- 1.5 Thermal management 9
- 1.6 Thesis overview 9

2 Theoretical background **11**
- 2.1 Theory of the phonon thermal transport 11
  - 2.1.1 Thermal flux 11
  - 2.1.2 Boltzmann transport equation 12
  - 2.1.3 Lattice dynamics 13
  - 2.1.4 Phonon scattering mechanisms 22
- 2.2 Density functional theory 32
  - 2.2.1 The many-body Schrödinger equation 32
  - 2.2.2 Born-Oppenheimer approximation 33
  - 2.2.3 Independent electron approximation 34

2.2.4 Hartree and Hartree-Fock approximation 35
2.2.5 Hohenberg-Kohn theorems 35
2.2.6 The Kohn-Sham equations 36
2.2.7 Exchange-correlation approximations 37
2.2.8 Pseudopotentials 38

3 Thermoelectric and phonon transport properties of two–dimensional IV–VI compounds 41
3.1 Introduction 41
3.2 Methodology 42
3.3 Results and discussions 44
3.3.1 Structure optimization and electronic structure 44
3.3.2 Carrier mobility and relaxation time 45
3.3.3 Thermoelectric properties 46
3.4 Summary 55

4 Ultra low lattice thermal conductivity and high carrier mobility of monolayer SnX_2 57
4.1 Introduction 57
4.2 Computational method 58
4.3 Results and discussions 59
4.3.1 Structure optimization and phonon spectra 59
4.3.2 Phonon group velocities, Grüneisen parameters, and Debye temperatures 60
4.3.3 Lattice thermal conductivity 63
4.3.4 Carrier mobility 65
4.4 Summary 68

5 Phononic thermal transport in two-dimensional indium chalcogenide compounds (InX, X=S, Se, Te) 69
5.1 Introduction 69
5.2 Methodology 71
5.3 Results and Discussions 71
5.3.1 Structure and phonon dispersion 71
5.3.2 Lattice thermal conductivity 74
5.3.3 Debye temperature, phonon group velocity, Grüneisen parameter, and phonon lifetime 75
5.3.4 Size-dependent lattice thermal conductivity 78

5.4 Summary 79

6 Strain engineering of phonon thermal transport properties in monolayer 2H-MoTe$_2$ 81
6.1 Introduction 81
6.2 Methodology 82
6.3 Results and discussions 83
6.3.1 Role of tensile strain on the lattice thermal conductivity 83
6.3.2 Phonon dispersion and Raman shift under tensile strain 85
6.3.3 Effect of strain on phonon group velocity, phonon heat capacity, and Grüneisen parameter 87
6.3.4 Strain-dependent phonon lifetime 88
6.3.5 Effect of strain on phonon mean free path 89
6.4 Summary 90

7 Superior and anisotropic thermal transport in the hybridized monolayer (BC$_2$N) of boron nitride and graphene 93
7.1 Introduction 93
7.2 Methodology 95
7.3 Results and Discussions 96
7.3.1 Geometry optimization, electron charge density, and band structure . 96
7.3.2 Total and mode-dependent lattice thermal conductivity 97
7.3.3 Phonon dispersion and group velocity 98
7.3.4 Phonon lifetime 100
7.3.5 Lattice thermal conductivity as a function of the size 101
7.3.6 Electronic thermal transport properties 102
7.4 Summary 102

8 Conclusions and future research directions 105
8.1 Conclusions 105
8.2 Future research directions 107

References 109

List of Figures

1.1 (a) Top and side views of the graphene crystal structure. (b) Comparison of the lattice thermal conductivity collected from experiments and theoretical published results. The values of the lattice thermal conductivity are taken from ref.[5, 7–11, 13–20]. . . . 3

1.2 (a) Crystal structure of the silicene (top view and side), silicene has buckled structure. (b) Comparison of lattice thermal conductivity obtained from first-principles and molecular dynamics. The values of the lattice thermal conductivity are taken from ref.[17, 21–28]. . . . 4

1.3 (a) Top and side view of the monolayer MoS_2 crystal structure, and (b) the predicted values of lattice thermal conductivity for mono and few layers MoS_2 using different experimental and theoretical approaches. The values of the lattice thermal conductivity are taken from ref.[30–40]. . . . 5

1.4 Schematic representation of the thermoelectric modules used for power generation (a) and refrigeration applications. . . . 7

2.1 Three-phonon scattering (a) coalescence and (b) decay processes which obey the energy conservation law. (c) Normal and (d) Umklapp processes for the phonon coalescence scattering. . . . 24

2.2 Comparison of a wavefunction within the strong Coloum potential of the nucleus (blue dotted lines) to the one within pseudopotential (solid red lines). The real and pseudopotential meet beyond the cutoff radius r_c. This figure is adapted from ref. [102] . . . 40

3.1 Crystal structure of two-dimensional monochalcogenides SnSe, SnS, GeSe, and GeS. (a) Side view perpendicular to the zigzag direction, (b) top view, (c) side view perpendicular to the armchair direction. . . . 43

3.2 Band structures along the high-symmetry k-points Γ, X, S, and Y and density of states of (a) SnSe, (b) SnS, (c) GeSe, and (d) GeS . . . 45

3.3 Elastic constants are calculated by fitting the energy difference ($E_{equ}-E_{str}$), where E_{equ} is the total energy in the equilibrium state and E_{str} is the total energy in the strained state, to quadratic polynomial functions for (a, b) SnSe, (c, d) SnS, (e, f) GeSe, and (g, h) GeS monolayers along armchair and zigzag directions. 47
3.4 Calculated deformation constants for group IV–VI compounds: (a, b) SnSe, (c, d) SnS, (e, f) GeSe, and (g, h) GeS monolayers. The conduction band minima (CBM) at uniaxial strains are fitted to straight lines. 48
3.5 Electrical (σ) and electronic thermal (κ_e) conductivities for the (a,e) SnSe, (b,f) SnS, (c,g) GeSe, and (d,h) GeS along the armchair (solid lines) and zigzag (dashed lines) directions at 300 K, 500 K, and 700 K. 50
3.6 Calculated Seebeck coefficients (S) as a function of the carrier concentration (n) along the armchair (solid lines) and zigzag (dashed lines) directions at 300 K, 500 K, and 700 K for the group IV–VI monolayers (a) SnSe, (b) SnS, (c) GeSe, and (d) GeS. 51
3.7 Phonon dispersions along high symmetry k-points for (a) SnSe, (b) SnS, (c) GeSe, and GeS 52
3.8 Lattice thermal conductivity (κ_l) for the group IV–VI monolayers are calculated as a function of the temperature using iterative (solid lines) and SMRTA (dashed lines) method. 53
3.9 Calculated Figures of merit (ZT) as a function of the carrier concentration (n) for the monolayer of (a,b) SnSe, (c,d) SnS, (e,f) GeSe, and (g,h) GeS along armchair and zigzag directions at temperature 300 K, 500 K, and 700 K. 54

4.1 (a) Top and (b) side views of the monolayer SnX_2 (X = S, Se). The dashed lines show the primitive unit cell (with lattice vectors $\vec{a}$ and $\vec{b}$). 59
4.2 Phonon band structure of (a) monolayer SnS_2 and (b) monolayer $SnSe_2$. The red, black, green, and blue lines represent the ZA , TA, LA, and the optical modes, respectively. 60
4.3 Phonon group velocities along (a) Γ-K, (c) Γ-M directions for monolayer SnS_2 and along (b) Γ-K, (d) Γ-M directions for monolayer $SnSe_2$ 62
4.4 Mode-dependent Grüneisen parameters of (a) monolayer SnS_2 and (b) monolayer $SnSe_2$ 63
4.5 Lattice thermal conductivities as a function of temperature for the monolayer (a) SnS_2 and (b) $SnSe_2$ 64
4.6 The cumulative lattice thermal conductivity as a function of phonon MFP for (a) monolayer SnS_2 and (b) monolayer $SnSe_2$ at room temperature 65

4.7 Electronic band structure of monolayer (a) SnS_2 and (b) $SnSe_2$ along high symmetry points Γ, K, and M. (c) Shift in the valence band maxima under uniaxial strain and (d) shift in the conduction band minima under uniaxial strain. 67

5.1 Atomic crystal structure of monolayer InX (X=S,Se,Te) from (a) top and (b) side views. The arrows indicate lattice vectors and the dash lines represent a unit cell. Blue and brown spheres, respectively represent the In and X atoms. (c) The representation of optical branches vibration in the long-wavelength limit. 72

5.2 Phonon band structures of the monolayer (a) InS, (b) InSe, and (c) InTe along high-symmetry points Γ-K-M-Γ. Solid lines represent the phonon spectra in which non-analytical correction is included, and yellow dash lines represent the optical branches without non-analytical corrections. 74

5.3 Lattice thermal conductivities of the monolayer InS, InSe, and InTe as a function of temperature calculated using iterative solutions of the phonon Boltzmann transport equation, lattice thermal conductivity (κ_l) with non-analytical corrections, and lattice thermal conductivity (κ_l') without non-analytical corrections. Solid lines are from the fitting of lattice thermal conductivities to $1/T$. 75

5.4 Branch-dependent phonon group velocities with non–analytical corrections in monolayer (a,d) InS, (b,e) InSe and (c,f) InTe along the Γ-K and Γ-M directions, respectively. 77

5.5 Mode dependent Grüneisen parameters and phonon lifetimes at room temperature as a function of frequency for the monolayer InS (a,d), InSe (b,e), and InTe (c,f), respectively. 78

5.6 Cumulative lattice thermal conductivity with non-analytical corrections as a function of phonon mean free path for monolayer InX at room temperature. The Equ.5.3 fits the curves, and they are plotted with solid lines. 79

6.1 (a) Top view and (b) side view of the 2H-$MoTe_2$ monolayer structure, Mo and Te atoms are represented by grey and skyblue spheres, respectively. The arrows indicates stretching of the monolayer. 83

6.2 (a) Lattice thermal conductivity of monolayer 2H-$MoTe_2$ as a function of temperature, (b) total lattice thermal conductivity, contribution of the ZA and TA/LA modes to the lattice thermal conductivity at 300 K as a function of tensile strain. 84

6.3 The phonon spectra of the monolayer 2H-MoTe$_2$ under different biaxial strains: (a) 0%, (b) 2%, (c) 4%, (d) 6%, and (e) 8% strains, and (f) the acoustic phonon dispersion relation along the Γ-X direction at different tensile strains 86

6.4 (a) Prominent peaks E' and A_1' in the Raman spectra under biaxial tensile strain and (b) schematic representation of the Raman/Infrared active modes $A_2''(I)$, $E'(I+R)$, $A_1'(R)$, and $E''(R)$ of the monolayer 2H-MoTe$_2$. 87

6.5 (a) Phonon group velocities of the monolayer 2H-MoTe$_2$ (a) ZA mode, (b) TA mode, (c) LA mode, and (d) optical modes under different tensile strains. . . 88

6.6 Phonon heat capacity (C_{ph}) and Grüneisen parameter as a function of strain at room temperature. 89

6.7 Phonon lifetimes as a function of phonon vibrational frequency under different strains at 300 K. 90

6.8 Cumulative lattice thermal conductivity with respect to MFP under different tensile strains at 300 K for the monolayer 2H-MoTe$_2$. Solid lines show the fitting curves. 91

7.1 Crystal structure of the monolayer BC$_2$N (a) top view (b) side view. The golden, white and green spheres represent carbon, nitrogen, and boron atoms, respectively, and The arrows indicate armchair and zigzag directions (c) electron localization function of the monolayer BC$_2$N starts from 0 (blue) to 1 (red). 95

7.2 Electronic band structure of the monolayer BC$_2$N calculated using the HSE06 method. The black lines in the band structure represent the valence band and conduction band. 97

7.3 (a) Lattice thermal conductivity (κ_l) and contribution of ZA, TA, LA, and optical modes to the lattice thermal along the armchair (a) and zigzag (b) directions as a function of the temperature of the monolayer BC$_2$N. 98

7.4 (a) Phonon spectrum along the high symmetric path Γ-X-S-Y-Γ in the first Brillouin zone, (b) phonon group velocities along the Γ-X direction, and (c) phonon group velocities along the Γ-Y direction of the monolayer BC$_2$N. The red, blue, green and navy colors correspond to ZA, TA, LA and optical branches, respectively. 99

7.5 Phonon relaxation time (τ) as a function frequency at 300K for the monolayer BC$_2$N. 100

7.6 (a) Lattice thermal conductivity as a function of phonon mean free path (PMFP)(Λ) at different temperatures, and (b) lattice thermal conductivity as a function of temperature at different sample sizes. Solid lines represent the armchair direction, and dash lines represent the zigzag direction. 101

7.7 Scaled Electrical (σ/τ) and electronic thermal (κ_e/τ) conductivities, and Seebeck coefficients of the monolayer BC_2N as a function of chemical potential along the zigzag (solid line) and armchair directions (dash line) at 300K, 500K, and 700K. 103

List of Tables

3.1 Calculated lattice parmeters and band gaps of SnSe, SnS, GeSe, and GeS. The values in the parentheses are from the Refs. [116, 138]. 44

3.2 Deformation potential constant (E_1), two dimensional elastic constant (C_{2D}), effective mass (m^*), carrier mobility (μ) and relaxation time (τ) at 300 K, 500 K, and 700 K, in the armchair and zigzag directions of the group IV–VI compounds. 49

3.3 The largest values of Seebeck coefficients (S) of bulk and monolayer SnSe, SnS, GeSe and GeSe at 300 K (unit: μVK^{-1}) 50

3.4 Comparison of lattice thermal conductivities κ_l of group IV-VI monolayers with other two-dimensional materials at room temperature 53

4.1 The percentage contribution of acoustic modes (ZA, TA, LA) and optical modes toward the lattice thermal conductivity at room temperature, and the Debye temperature 61

4.2 Effective mass ($m^*_{\Gamma-\mathrm{M}}$, $m^*_{\mathrm{K}-\mathrm{M}}$), average effective mass (m_d), in-plane stiffness (C^{2D}), deformation constant (E_1), and mobility (μ) for hole and electron in single layer SnX_2at 300 K. The unit of effective masses is m_e. 68

5.1 The calculated lattice constants (a), the distance between Indium atoms (d_{In-In}), the distance between Indium and chalcogen atoms (d_{In-X}), and the vertical distance between chalcogen atoms of the monolayer InX. The values in parentheses are taken from ref.[200] 72

5.2 The dielectric constants and Born effective charges of the monolayer InX. . . . 73

5.3 Debye temperature (Θ_D^α), representative mean free path (rMFP), specific heat (C_v), lattice thermal conductivity (κ_l) with non-analytical corrections, and lattice thermal conductivity (κ_l') without non-analytical corrections of the monolayer InS, InSe, and InTe. 76

5.4 Percentage contribution of the ZA, TA, LA, and optical phonon branches to lattice thermal conductivity at room temperature for the monolayer InS, InSe, and InTe. 76

Chapter 1

Introduction

1.1 Motivation and objective

In the light of recent developments, a considerable amount of fundamental research and engineering applications is focused on the energy efficiency. One broad area of such scientific researches is based on the fundamental understanding of thermal transport processes of heat and how to employ it in our environment and materials[1–4]. Thermal transport research has promoted a diverse spectrum of the applications include high-performance thermoelectric materials to convert waste heat into useful electrical energy, thermal management in the nanoscale electronics, thermal barrier, and the proposed use of nanoparticles in thermal medical therapies. Therefore, understanding the thermal transport is very important for our basic knowledge of solid state physics and science.

In semiconductors and insulators, the lattice vibrations called phonons are the responsible for the thermal conduction, while the electrons are contributed very little. However, calculating lattice thermal conductivity (κ_l) is a very challenging job, and no universal or comprehensive theory suits at all temperatures or includes all possible effects. The scientific community has developed several theoretical approaches and practical implementations. Each method is developed at its level of refinement and limitations. The equilibrium molecular dynamics (EMD)[5] and non-equilibrium molecular dynamics (NEMD)[6] simulations have been adopted in the past to study temperature-dependent lattice thermal conductivity and other phonon thermal transport properties of the two-dimensional and conventional three-dimensional materials. The accuracy of the molecular dynamics depends on the interatomic force fields, and the force fields can be either calculated from the empirical potential or the first principles calculations. The empirical potentials are restricted in their scope because of their low accuracy and relatively straightforward design. Although, first-principles molecular dynamics are accurate but computationally expensive.

The primary goal of this thesis is to study and understand the phonon thermal transport and electronic properties in a vast range of two-dimensional materials and their potential applications in thermoelectric and thermal management. We will obtain the lattice thermal conductivity by solving the phonon Boltzmann transport equation based on density functional theory. We will study strain-dependent lattice thermal conductivity and other phonon properties such as phonon group velocity, phonon anharmonicity, phonon lifetime. We will also calculate the electronic properties such as electronic band structure, electronic thermal and electrical conductivities and electrons/holes mobilities. Our calculations will give the underlying physics to understand thermal transport properties and will guide to the experimentalist.

1.2 A brief history of the phonon thermal transport in the two-dimensional materials

Two-dimensional materials have been widely investigated in past decade due to their extraordinary electrical, thermal, chemical and optical properties, and diverse spectrum of applications such as energy conversion, energy storage, nanoelectronics, and thermal management. The thermal transport of two-dimensional materials is often essential in these applications, for example, low lattice thermal conductivity is required to convert waste energy into useful electricity and high lattice thermal conductivity is required for the thermal interface material. In this section, we review the available theoretical calculations on the phonon thermal transport of the various two-dimensional materials including graphene, phosphorene, silicene and monolayer MoS_2.

1.2.1 Graphene

Phonon thermal transport properties in graphene have been intensively studied in the past few years. The reported values of the lattice thermal conductivity for graphene at room temperature is ranging from 2000 to 5500 W/mK, and most of the experimental results and theoretical results are shown in Fig.1.1 (b). Balandin et al.[7] measured the lattice thermal conductivity of the graphene using the optothermal Raman technique for the first time and they found lattice thermal conductivity to be 5300 W/mK at 300K. Later, Faugeras et al.[8], Cai et al.[9], Chen et al.[10] and Li et al.[11] employed the more refined experimental method and they obtained a much lower lattice thermal conductivity than previously reported values.

In order to explain the high lattice thermal conductivity in graphene, many theoretical calculations were performed. Nika et al.[12] calculated the lattice thermal conductivity using the relaxation time approximation and the flexural acoustic phonons are neglected due to their

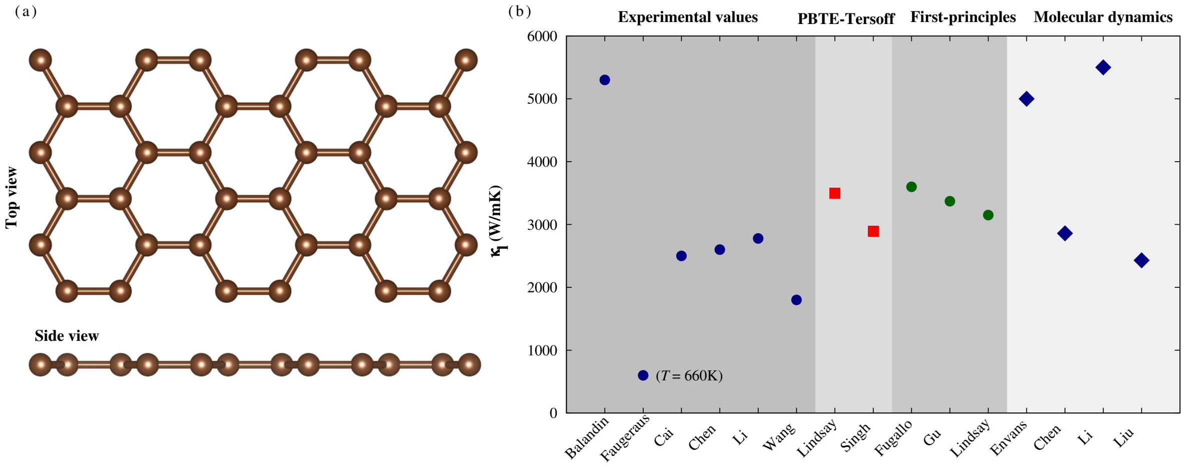

Figure 1.1: (a) Top and side views of the graphene crystal structure. (b) Comparison of the lattice thermal conductivity collected from experiments and theoretical published results. The values of the lattice thermal conductivity are taken from ref.[5, 7–11, 13–20].

limited group velocity. However, Lindsay et al.[13] adopted the phonon Boltzmann transport equation (PBTE) to obtained the lattice thermal conductivity of graphene using the modified Tersoff potential, and they showed that the flexural acoustic (ZA) mode is responsible for the 70-80% of heat conduction which is confirmed by Singh et al.[14] and the various first-principles studies[15–17]. The significant contribution of the ZA mode is due to the reflection symmetry in graphene which prevents the three-phonon scattering with phonon modes and hence the ZA mode phonons lifetimes are increased. Many classical molecular dynamics simulations have also been performed to predict the lattice thermal conductivity of graphene but the results are scattered and not reliable due to parameterized potentials[5, 10, 18, 19].

1.2.2 Silicene

Silicene possesses a low-buckled two-dimensional honeycomb crystal structure as shown in Fig. 1.2 (a) and has fascinating chemical and physical properties. Silicene can be more compatible with silicon-based devices and technologies as compared to graphene. Silicene and graphene have shared similar electronic properties because of their similar band structures. For example, the charge carriers in both structures are massless fermion due to the presence of Dirac cone in their band structures and high electrical conductivity similar to graphene. However, silicene has buckled structure, unlike graphene which breaks the reflection symmetry and results in lattice thermal conductivity.

The lattice thermal conductivity of the silicene has been widely studied based on the solution of PBTE coupled with first-principles and classical molecular dynamics and the predicted

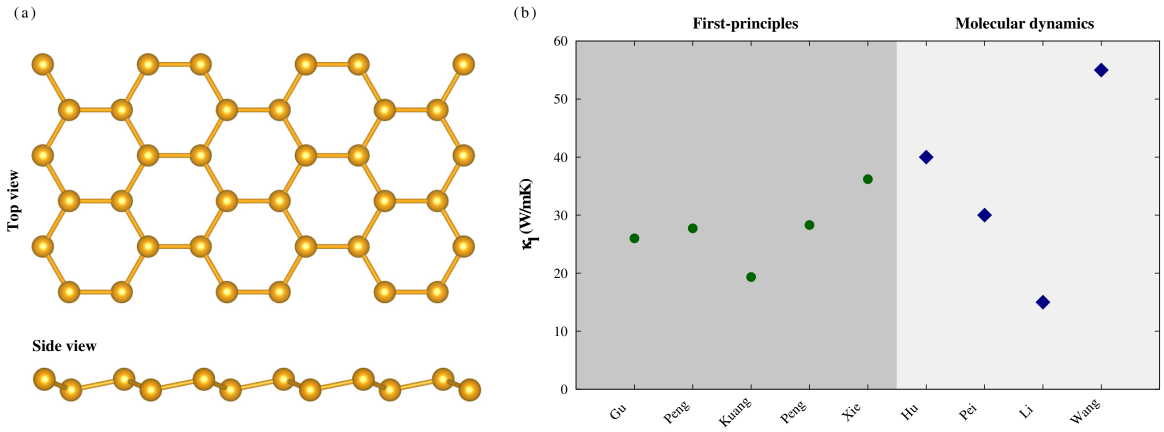

Figure 1.2: (a) Crystal structure of the silicene (top view and side), silicene has buckled structure. (b) Comparison of lattice thermal conductivity obtained from first-principles and molecular dynamics. The values of the lattice thermal conductivity are taken from ref.[17, 21–28].

values range from 9.4 to 55 W/mK as shown in Fig. 1.2 (b). Although there is no experimental value of lattice thermal conductivity available for silicene because it is harsh to synthesized freestanding silicene. Gu and Yang et al.[17] calculated the lattice thermal conductivity of silicene using the iterative solution PBTE based on the first principle and they found the lattice thermal conductivity of silicene is surprisingly an order of magnitude lower from the lattice thermal conductivity value for bulk silicon. Peng et al.[21] and Xie et al.[22] also calculated the lattice thermal conductivity using the same method and found similar results. Kaung et al.[23] obtained the lattice thermal conductivity using the single mode relaxation time approximation (SMRTA) solution of PBTE based on first-principles they got a much smaller value. The lattice thermal conductivity of silicene has also been predicted using the classical molecular dynamics by Hu et al.[24], Pei et al.[25], Li et al.[26] and Wang et al.[27], and they found very scattered result similar to graphene.

1.2.3 Monolayer MoS_2

Monolayer MoS_2 has a three-layer structure as shown in Fig.1.3 (a) in which one layer of Mo atoms is sandwiched between two layers of S atoms. Monolayer MoS_2 has received considerable attention during the past decade because of the broad range of applications including nanoelectronics, catalysts, optoelectronics, and thermoelectrics. For example, the on/off switching ratio of the MoS_2 field-effect transistor can reach up to 10^8 at room temperature, which is hard to accomplish in a graphene transistor. According to Slack's theory[29], the lattice thermal conductivity of monolayer MoS_2 is considered to be low because of the heavy

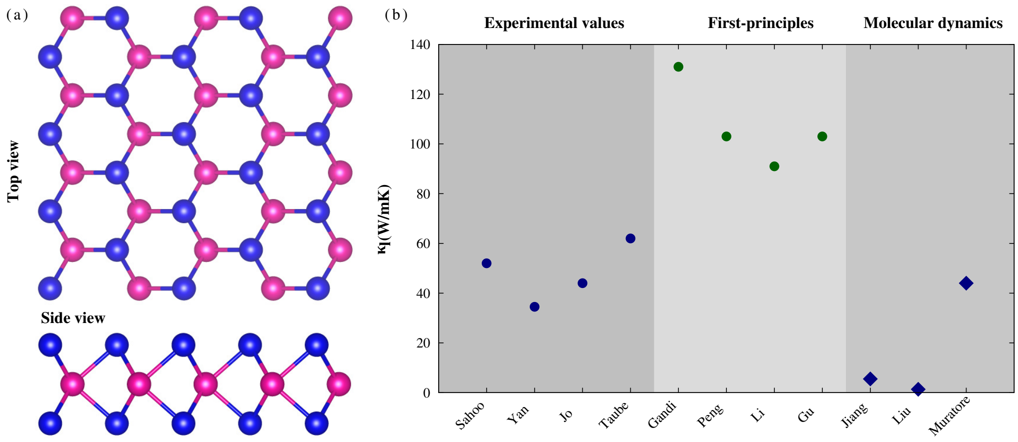

Figure 1.3: (a) Top and side view of the monolayer MoS_2 crystal structure, and (b) the predicted values of lattice thermal conductivity for mono and few layers MoS_2 using different experimental and theoretical approaches. The values of the lattice thermal conductivity are taken from ref.[30–40].

mass of the Mo atom and low Debye temperature. Therefore, monolayer MoS_2 has been extensively investigated as a promising thermoelectric material.

Many experimental and theoretical studies have been performed to explore the lattice thermal conductivity of monolayer MoS_2 and the predicted value of the lattice thermal conductivity is ranging from 1.35 to 131 W/mK as shown in Fig.1.3 (b). Sahoo and coworkers have measured the lattice thermal conductivity for the eleven layers of MoS_2 is 52 W/mK at room temperature using the temperature-dependent Raman spectroscopy[30]. Later, Yan et al.[31] has predicted the lattice thermal conductivity for monolayer MoS_2 using the similar technique and found the lattice thermal conductivity to be 34.5 W/mK. Jo et al.[32] also measured the lattice thermal conductivity for four layers of MoS_2 using the microbridge device. Taube et al.[33] used monolayer MoS_2 on SiO 2 substrate to measure the lattice thermal conductivity and it is found that the lattice thermal conductivity for the supported monolayer is higher than the suspended monolayer. Gandi et al.[34] , Peng et al.[35] and Gu et al.[36] have obtained the lattice thermal conductivity using the iterative solution of PBTE based on the first-principles and the calculated values are higher from the experimentally measured value by Yan. Li. Molecular dynamics simulations have been carried out by Jiang et al.[37], Liu et al.[38] and Muratore et al.[39] using different empirical potential. The calculated values of lattice thermal conductivity from the molecular dynamics range widely from 1.35 to 44 W/mK which are much lower from first-principles.

1.3 Thermoelectrics

After the second industrial revolution, the world has been maintained the increasing demand for energy by burning more fossil fuels. The world's critical dependence on fossil fuels and the carbon emissions during combustion of fossil fuels are bringing both natural and human systems at stake[41–44]. On the other hand, the energy we waste as heat is more than 60% of the world's energy and heat can be considered a renewable energy source[42]. Thermoelectrics is a straightforward technology which converts the waste heat into the useful electricity via Seebeck effect. A thermoelectric device is a solid-state device without moving parts, no noises, and environmentally friendly. The efficiency of a thermoelectric material, η, is defined as[41]:

$$\eta = \eta_c \left[\frac{\sqrt{1+ZT_{avg}} - 1}{\sqrt{1+ZT_{avg}} + \left(\frac{T_C}{T_H}\right)} \right], \tag{1.1}$$

where η_c is the Carnot efficiency, ZT_{avg} is an average value of the figure of merit between cold and hot temperatures, T_C is the temperature of cold end, and T_H is the temperature of hot end. The efficiency of thermoelectric converters is still only a fraction (10–20%) of the theoretical possible Carnot efficiency because of the poor thermoelectric properties of the materials.

1.3.1 Thermoelectric effects

Thermoelectric devices have relied on two important thermoelectric effects, i.e. the Seebeck effect and the Peltier effect. When two dissimilar semiconducting materials are joined, and temperature difference (ΔT) is applied to the junctions, then a potential difference (ΔV) is developed as shown in Fig.1.4. This phenomenon is called Seebeck or thermopower effect, and Seebeck discovered it in 1821. The Seebeck effect generates a potential difference that is proportional to applied temperature difference, and the proportionality constant is called the Seebeck coefficient (S). It is defined as:

$$S \equiv \frac{\Delta V}{\Delta T}. \tag{1.2}$$

The Seebeck effect originates from the diffusion of electrons and holes from the hot end to the cold end of the material as shown in Fig.1.4, and therefore, when a material is placed in a temperature gradient, the charge carriers are accumulated on the cold end creating a potential difference. The value of the Seebeck coefficient predicts the average entropy transported by a charge carrier (electrons/holes) divided by its charge at thermal equilibrium.

The Peltier effect is the reverse processes of the Seebeck effect: When the electrical current

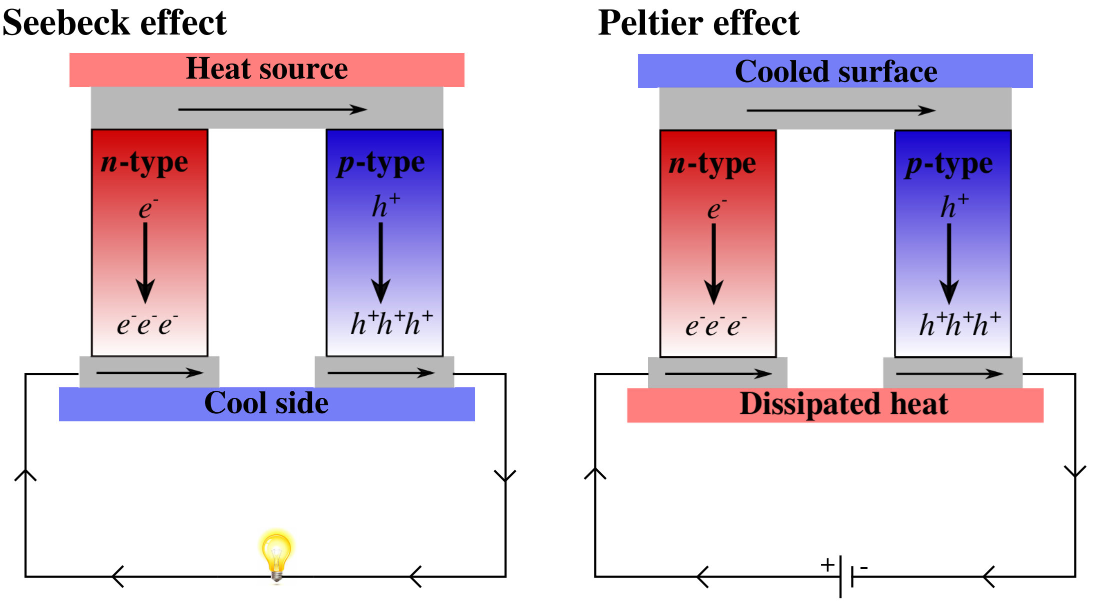

Figure 1.4: Schematic representation of the thermoelectric modules used for power generation (a) and refrigeration applications.

(I)flows through a circuit material containing two dissimilar semiconductors materials, then a temperature gradient is created between the junctions as shown in Fig.1.4. The heat absorption and generation (Q) at the junctions are dependent on the direction of the current. The Peltier coefficient (Π) is defined as:

$$\Pi \equiv \frac{Q}{I}. \tag{1.3}$$

The relationship between the Seebeck and Peltier coefficients, also called Kelvin relationship, can be derived using irreversible thermodynamics which can be written as:

$$S = \frac{\Pi}{T} \tag{1.4}$$

The Peltier effect has been used in many applications, such as temperature controlled automobile seats, picnic cooler and solid-state cooler for scientific instruments.

1.3.2 Figure of merit

The performance of a thermoelectric material is described by the dimensionless quantity called the figure of merit (ZT). It can be defined as[44]:

$$ZT = \frac{S^2 \sigma T}{\kappa_e + \kappa_l},$$

where σ denotes the electrical conductivity, κ_e is the electronic thermal conductivity and T is the temperature. Many schemes have been developed for maximizing the power factor ($S^2\sigma$) and minimizing the thermal conductivity ($\kappa_e + \kappa_l$) to obtain enhanced ZT. The electrical conductivity and electronic thermal are directly proportional to the charge carrier concentration. However, the Seebeck coefficient is decreased with increasing the carrier concentration. Semiconducting materials have the highest ZT values because of the excellent combination of S, σ, and κ_e. The interdependence of S, σ, and κ_e prevails a challenging barrier toward further developments.

Several classical approaches have been developed to enhance the ZT either by improving the power factor or reducing the lattice thermal conductivity. The approaches used to improve ZT include the use of the materials contained heavy elements, band structure engineering, alloy-point defect scattering and materials with the complicated crystal structure[44–47]. Hicks et al. and Dresselhaus et al.[48] discovered an efficient method to increase ZT by reducing the dimensionality of the material, which increases the Seebeck coefficient due to the increased density of states near the Fermi level. They found that the ZT of bulk Bi_2Te_3 is improved 13 times by converting into the quantum well.

1.4 Strain effect

The strain is a handy and effective tool to enhance the performance of the semiconducting devices. It can tune electronic, optical, and thermoelectric properties. When two or more different kinds of two-dimensional crystals are laterally connected or vertically stacked together (heterostructure), strain always presents because of the lattice mismatch. Strain changes the phonon spectra and the phonon scattering rate. It could also produce structure instability and defects. However, the effect of tensile strain on the phonon thermal transport of two-dimensional materials is unpredictable because the flexural acoustic (ZA) mode becomes harder and transverse acoustic (TA) and longitudinal acoustic (LA) modes become softened. The lattice thermal conductivities of graphene[49], *h*-BN[50], silicene[22], antimonene[51], germanene[23], stanene[23], monolayer penta-SiC_2[52], and multilayer graphene[53] are increased under tensile strain and the enhancement in the lattice thermal conductivities are attributed to the anomalous behavior of the ZA mode and the increase in lifetime of the ZA mode phonons under tensile strain. While the lattice thermal conductivities for monolayer MoS_2[54] and penta-Gr[52] are decreased.

1.5 Thermal management

Over the past decades, modern electronic technologies have sustained significant miniaturization which increases the power density, and the tendency is continuing. Effective heat ejection in the electronic devices has become a critical issue in the development of information, energy storage, and communication technologies because of the rapid increase in the power density[55, 56]. The extra heat produced during the device operation can reduce the reliability and performance of the device[57]. For example, high-frequency devices generate a tremendous amount of heat in small confined areas, and therefore produce hotspots which result in the weak performance of the devices[58].

Thermal management is the attempt to regulate the operating temperature of the devices. A thermal management system is composed of a cooling setup, thermal interface materials, temperature controller, and heat sink[7, 56, 59]. Thermal management techniques for the removal of hotspot contain a selection of high thermal conductivity materials and heat sink designing. The exploration of two-dimensional materials brings new exciting opportunities for the thermal management. Among the two-dimensional materials, the thermal transport properties of the graphene and hexagonal boron nitride (h-BN) have been intensively investigated. It has been determined that the thermal conductivities are significantly higher from their bulk counterpart. Graphene, with predicted thermal conductivities ranging 3000-5300 W/mK at room temperature (see Fig.1.1), has received considerable attention but it is not suitable for the practical application because of the zero bandgap. On the other hand, h-BN also has very high thermal conductivity, but the problem with h-BN is large bandgap[50]. Two-dimensional materials with high thermal conductivity and suitable bandgap are promising for both thermal management applications and fundamental understanding of heat transfer.

1.6 Thesis overview

After this introductory chapter, the overview of the remaining thesis is arranged as follows. In Chapter 2, the phonon thermal transport and the density functional theories are introduced. The phonon-scattering mechanisms are discussed in detail. Method to solve the PBTE is also studied.

In Chapter 3, the structural, electronic, thermoelectric, and phonon-transport properties of the two-dimensional mono-chalcogenide compounds SnSe, SnS, GeSe, and GeS are studied using density functional theory combined with Boltzmann transport theory. The predicted values of ZT these monolayers are very high due to their high S and low lattice thermal conductivity as compared to other two-dimensional materials.

In Chapter 4, the lattice thermal conductivity and electronic mobility of monolayers SnS_2 and $SnSe_2$ are investigated. The calculated values of lattice thermal conductivity are very as compare to other two-dimensional materials such as phosphorene, silicene, stanene, and monolayer MoS_2. In order to understand the ultra-low lattice thermal conductivity, the phonon dispersion, phonon group velocity, Gruneisen parameter, and Debye temperature are studied in detail. The lattice thermal conductivity as a function of phonon mean free path is also explored.

In Chapter 5, the phonon transport properties and the lattice thermal conductivity of the monolayers InX are explored. The lattice thermal conductivity trend ($\kappa_{\mathrm{InS}}>\kappa_{\mathrm{InSe}}>\kappa_{\mathrm{InTe}}$) is explained with help of the phonon spectra, phonon group velocities, Grüneisen parameters, Debye temperatures and phonon-phonon scattering processes. Furthermore, the contribution of each mode toward total lattice thermal conductivity is extracted, and temperature and size dependence are also discussed. Monolayer InX can be used as a thermoelectric material because of the low lattice thermal conductivity.

In Chapter 6, the effect of tensile strain on the phonon thermal transport properties of the monolayer 2H-$MoTe_2$ is studied. By applying the biaxial tensile strain, the LA and TA modes are softened, which decreases phonon group velocity. The phonon lifetime reduces under the tensile strain due to the increase in the phonon-phonon scattering rate. The role of strain on Grüneisen parameter and heat capacity is also discussed. The lattice thermal conductivity is reduced approximately 2.5 times under 8% tensile strain for the monolayer 2H-$MoTe_2$ contrary to graphene, germanene, silicene, germanene, and Penta-SiC_2.

In Chapter 7, the thermal transport properties of the monolayer BC_2N are systematically investigated by solving the Boltzmann transport equation iteratively based on first-principles calculations. The lattice thermal conductivity along the zigzag direction is very high as compared to armchair direction due to the strong C-C bonding along the zigzag direction. To explain ultra-high lattice thermal conductivity of the monolayer BC_2N, the phonon dispersion, phonon lifetimes and phonon group velocities are studied. The electronic thermal transport properties are also very high value at room temperature. Due to the high thermal conductivity, monolayer BC_2N can be used as a promising material for thermal management and heat dissipation in the nano-electronic devices.

In Chapter 8, the summaries of the current research work are provided, and directions for the future research are also discussed.

Chapter 2

Theoretical background

2.1 Theory of the phonon thermal transport

2.1.1 Thermal flux

When a material is placed in a temperature gradient (∇T), thermal energy is transported through a material by both the phonons (crystal lattice vibration) and the electrons. In semiconducting materials, the large part of the heat is transported by the phonons, while electrons carry a small amount of heat. The temperature gradient induces heat flux (Q) (because of the phonons flow) through a material which is given by[60]:

$$\vec{Q} = \frac{1}{\Omega}\sum_{\alpha q}\hbar\omega_{\alpha q}\vec{v}_{\alpha q}n_{\alpha q}, \tag{2.1}$$

where α is phonon mode, q is the phonon wavevector, Ω is the crystal volume. $\omega_{\alpha q}$, $\vec{v}_{\alpha q}$, and $n_{\alpha q}$ are the phonon frequency, phonon group velocity and phonon distribution function (phonon obeys Bose-Einstein distribution function) in α mode respectively. Heat flux can also be calculated from the Fourier's law for the small temperature gradient. The heat flux is directly related to the temperature gradient, and the proportionality constant is defined as the lattice thermal conductivity κ_l. For the temperature gradient along the y-direction, the heat flux along the x-direction is given by:

$$\vec{Q} = -\sum_{y}\kappa_l^{xy}\frac{\partial T}{\partial y}. \tag{2.2}$$

The minus indicates that the thermal conductivity tensor is a positive quantity. Comparing the thermal fluxes given by Equ.2.1 and Equ.2.2 obtains the following equation which contains the lattice thermal conductivity:

$$\vec{Q} = -\kappa_l^{xx}\frac{\partial T}{\partial x} = \frac{1}{V}\sum_{\alpha q}\hbar\omega_{\alpha q}\vec{v}_{\alpha q}^{x}(\vec{q})n_{\alpha q}. \tag{2.3}$$

The κ_l^{xx} is the symmetric rank-two tensor, and non-diagonal elements are zero. In this work κ_l^{xx}, κ_l^{yy}, and κ_l^{zz} denote the lattice thermal conductivity along the x, y, and z directions, respectively. For cubic materials, the x , y , and z directions are identical and therefore κ_l^{xx}, κ_l^{yy}, and κ_l^{zz} should be same.

2.1.2 Boltzmann transport equation

Boltzmann transport equation (BTE) calculates the change in the phonon distribution function ($n_{\alpha q}$) through phase space at any time (t), when a material is placed in a temperature gradient ∇T. The general form of BTE can be written as[60–62]:

$$\frac{\partial n_{\alpha q}}{\partial t} = -\vec{v}_{\alpha q}.\vec{\nabla}_r n_{\alpha q} - \vec{F}_{ext}.\vec{\nabla}_p n_{\alpha q} + (\frac{\partial n_{\alpha q}}{\partial t})_{scatt.}. \tag{2.4}$$

According to this general form of BTE, three terms on the right side of Eqn.2.4 are responsible for changing the phonon distribution function with time. The first term is the rate of change of the distribution function due to phonon motion, the second term represents the change in distribution function by the external force F_{ext}, and the third term is due to the collisions of phonons with each other, impurities, crystal boundary, and defects. Several assumptions are made to predict the κ_l. In phonon thermal transport, the driving force is the temperature gradient. Therefore, we need to write temperature-dependent phonon distribution function. If no external forces are acting on the phonons and the system is under a steady state condition ($\frac{\partial n_{\alpha q}}{\partial t} = 0$)[62, 63]. The reformulated BTE is given by:

$$\vec{v}_{\alpha q}.\vec{\nabla}T\frac{\partial n_{\alpha q}}{\partial T} = (\frac{\partial n_{\alpha q}}{\partial t})_{scatt.}. \tag{2.5}$$

This equation (2.5) is called the phonon Boltzmann transport equation (PBTE). Under the relaxation time approximation (RTA), the PBTE can be written as:

$$\vec{v}_{\alpha q}.\vec{\nabla}T\frac{\partial n_{\alpha q}}{\partial T} = \frac{n_{\alpha q} - n_{\alpha q}^0}{\tau_{\alpha q}}, \tag{2.6}$$

where $\tau_{\alpha q}$ is the phonon relaxation time, and $n_{\alpha q}^0$ is phonon distribution function at the equilibrium which obeys the Bose-distribution function:

$$n_{\alpha q}^{0} = \frac{1}{exp[\hbar\omega_{\alpha q}/k_B T] - 1}. \tag{2.7}$$

We define the change in the phonon population as:

$$\delta_{\alpha q} = n_{\alpha q} - n_{\alpha q}^{0}, \tag{2.8}$$

where $\delta_{\alpha q}$ represents the change in phonon population, and it is minimal compared to $n_{\alpha q}^{0}$. Using the Eqn.2.8 , the Eqn.2.7 can be written as:

$$\vec{v}_{\alpha q}.\vec{\nabla}T\frac{\partial n_{\alpha q}^{0}}{\partial T} + \vec{v}_{\alpha q}.\vec{\nabla}T\frac{\partial \delta_{\alpha q}}{\partial T} = \frac{n_{\alpha q} - n_{\alpha q}^{0}}{\tau_{\alpha q}}. \tag{2.9}$$

The second term on the left-hand side is dropped because it is very small. The above equation can be written as:

$$n_{\alpha q} = n_{\alpha q}^{0} - \tau_{\alpha q}(\vec{v}_{\alpha q}.\vec{\nabla}T\frac{\partial n_{\alpha q}^{0}}{\partial T}). \tag{2.10}$$

The Eqn.2.3 and Eqn.2.10 can be solved simultaneously to get an equation for the lattice thermal conductivity along the x-direction:

$$\kappa_l^{xx} = \frac{1}{V}\sum_{\alpha q} C_{\alpha q} v_{\alpha q}^{2} \tau_{\alpha q}, \tag{2.11}$$

where $C_{\alpha q}$ is the phonon heat capacity of the α mode, which is defined as:

$$C_{\alpha q} = \frac{(\hbar\omega_{\alpha q})^2}{k_B T^2} n_{\alpha q}^{0}(n_{\alpha q}^{0} + 1). \tag{2.12}$$

2.1.3 Lattice dynamics

The phonon frequency, phonon group velocity, and phonon lifetime are required to obtain the κ_l from the Eqn. 2.11. Here, we focus on the calculation of these phonon quantities from the harmonic (2^{nd} order) and anharmonic (3^{rd} order) interatomic force constants (IFCs) calculations. The lattice dynamic is well discussed in many excellent books[63–68] and articles[69–72]. The crystal potential V can be expanded in terms atomic displacements using Taylor series as:

$$\begin{aligned}V =&V_0+\sum_{lb}\sum_{x}\Pi_x u_x(lb)+\frac{1}{2!}\sum_{lbl'b'}\sum_{xy}\Phi_{xy}(lb,l'b')u_x(lb)u_y(l'b')\\&+\frac{1}{3!}\sum_{lbl'b'l"b"}\sum_{xyz}\Psi_{xyz}(lb,l'b',l''b'')u_x(lb)u_y(l'b')u_z(l''b'')+...,\end{aligned} \tag{2.13}$$

where $u_x(lb)$, $u_y(l'b')$, and $u_z(l''b'')$ are instantaneous atomic displacements and x, y, and z are the Cartesian axes. The unit cell is located by the vectors l, l', and l'' and the atoms in the unit cell are represented by the b, b', and b'' position vectors. The first term V_0 on the right side of Eqn.2.13 is reference energy which is constant energy and the second term is the first derivative of the potential energy, $\Pi_x = \frac{\partial V}{\partial u_x(lb)}$, which is zero at equilibrium. The Φ and Ψ are represented the second (second order IFCs matrix contains nine elements) and third (third order IFCs matrix contains twenty-seven elements) derivatives of the potential energy, respectively. The second and third order force constants can be expressed as:

$$\Phi_{xy}(lb,l'b') = \frac{\partial^2 V}{\partial u_x(lb)\partial u_y(l'b')}, \tag{2.14}$$

and

$$\Psi_{xyz}(lb,l'b',l''b'') = \frac{\partial^3 V}{\partial u_x(lb)\partial u_y(l'b')\partial u_z(l''b'')}. \tag{2.15}$$

Harmonic lattice dynamics

The vibrational phonon frequency and phonon group velocity of the crystal are obtained from the harmonic IFCs. For the harmonic lattice dynamics, we only consider the potential up to second order term in Eqn.2.13, the harmonic potential can be written as[64]:

$$V = V_0+\frac{1}{2!}\sum_{lbl'b'}\sum_{xy}\Phi_{xy}(lb,l'b')u_x(lb)u_y(l'b'). \tag{2.16}$$

We have introduced a new variable $h = l-l'$ (relative position between unit cells) by assuming that the crystal has translation symmetry. The matrix for the harmonic force constants can be written as:

$$\Phi_{xy}(lb,l'b') = \Phi_{xy}(0b,(l'-l)b') = \Phi_{xy}(0b,hb').$$

The force $F_x(0b)$ experienced by the atom b in x-direction due to the displacement (with magnitude u) of another atom b' in the y-direction in a crystal can be expressed as:

$$F_x(0b) = -\sum_{hb'y} \Phi_{xy}(0b, hb')u_y(hb'). \tag{2.17}$$

Using the Eqn.2.17, the equation of motion for each atom under harmonic approximation can be written as:

$$m_b \ddot{u}_x(0b,t) = -\sum_{hb'y} \Phi_{xy}(0b, hb')u_y(hb',t), \tag{2.18}$$

where m_b is the mass of the atom at the b position in the unit cell. The atomic-vibrations in the unbound crystal are treated as a plane wave which covers the whole crystal. Therefore, the atomic-displacement, the solution of the Eqn.2.18, can be expressed as:

$$u_x(hb,t) = \frac{1}{\sqrt{m_b}} \sum_q e_x(b|q)e^{i(qh-\omega t)}, \tag{2.19}$$

where $e_x(b/q)$ represents the amplitude and direction of motion of the atom b in unit cell l produced by a plane wave with vector q and frequency ω. Substituting the atomic-displacement in Eqn.2.19 into Eqn.2.18 leads to the eigenvalue equation:

$$\omega^2(q)e_x(b|q) = \sum_{b'y} D_{xy}(bb'|q)e_y(b'|q). \tag{2.20}$$

The non-trivial solution to the Eqn.2.20 can be found from the secular equation:

$$|D_{xy}(bb'|q) - \omega^2 \delta_{xy}\delta_{bb'}| = 0, \tag{2.21}$$

where $D_{xy}(bb'/q)$ is the dynamical matrix, which can be written as:

$$D_{xy}(bb'|q) = \frac{1}{\sqrt{m_b m_{b'}}} \sum_h \Phi_{xy}(0b, hb')e^{iqh}. \tag{2.22}$$

The phonon frequencies, $\omega(\alpha q)$, and polarization vectors, $e(b/\alpha q)$, are calculated by diagonalizing the Eqn.2.22 for each value of the q. The term αq represents the particular phonon mode with α^{th} phonon branch and q wavevector. The dynamical matrix can be shown that it is a Hermitian matrix for any value of q:

$$D_{xy}(bb'|q) = ((D_{xy}(b'b|q)^*)^T. \tag{2.23}$$

This Eqn.2.23 indicates that the phonon dispersion squared are real. Therefore, the phonon frequency for any value of q is either real or purely imaginary and from the Eqn.2.19, the atomic-displacement rises exponentially to infinity or drops exponentially to zero for the purely imaginary phonon frequency. Imaginary value of the phonon frequency indicates that the crystal structure is not stable.

The polarization vector ($e_x(b|\alpha q)$) describes the collective motion of the atom b in the x-, y- or z-direction for the phonon in α-branch with a wavevector q. It is a $3n \times 1$ column matrix, and can be written as:

$$e_x(b|\alpha q) = \left\{ \begin{array}{c} e_1(1|\alpha q) \\ e_2(1|\alpha q) \\ e_3(1|\alpha q) \\ e_1(2|\alpha q) \\ \vdots \\ e_3(n|\alpha q) \end{array} \right\}.$$

The polarization vector is a phonon eigenvector contains n independent vectors, and it obeys the closure and orthogonality conditions, given as:

$$\sum_{\alpha} e_x^*(b/\alpha q) e_y(b|\alpha' q) = \delta_{xy}\delta_{\alpha\alpha'} \tag{2.24}$$

$$\sum_{bx} e_x^*(b/\alpha q) e_x(b|\alpha' q) = \delta_{\alpha\alpha'}, \tag{2.25}$$

which means that the eigenstates of the phonon do not interact with each other and decoupled. The harmonic approximation is very useful to simplify the equations of motion allowing an analytical solution of the system dynamics. Using the phonon frequencies calculated from Eqn.2.21, the harmonic Hamiltonian for an atom with mass m_b and momentum operator $p(lb)$ at position b in the unit cell l can be written as:

$$H^{harm} = \sum_{lb} \frac{p(lb).p(lb)}{2m_b} + \frac{1}{2!} \sum_{lbl'b'} \sum_{xy} \Phi_{xy}(lb, l'b') u_x(lb) u_y(l'b'). \tag{2.26}$$

The Fourier transform of u and p can be written as:

$$u(lb) = \frac{1}{\sqrt{N_0\Omega}} \sum_{q} U(qb) e^{iql} \tag{2.27}$$

$$p(lb) = \frac{1}{\sqrt{N_0\Omega}} \sum_{q} P(qb) e^{-iql}, \tag{2.28}$$

where $N_0\Omega$ represents the crystal volume having N_0 unit cells. The Fourier representations of $U(qb)$ and $P(qb)$ satisfy the following commutation relation:

$$\begin{aligned}[U(qb),P(q'b')] &= \frac{1}{N_0\Omega}\sum_{ll'} e^{-i(ql-q'l')}\hat{I}i\hbar\delta_{ll'}\delta_{bb'} \\ &= \hat{I}i\hbar\delta_{qq'}\delta_{bb'},\end{aligned} \tag{2.29}$$

where I is the identity matrix. Now, we plugin the Eqn.2.27 and Eqn.2.28 into Eqn.2.26, the harmonic Hamiltonian can be rewritten as:

$$\begin{aligned}H^{harm} &= \frac{1}{N_0\Omega}\sum_{qq'lb}\frac{P(qb).P(q'b)}{2m_b}e^{-i(q+q')l} \\ &+ \frac{1}{2!}\frac{1}{N_0\Omega}\sum_{qq'lbl'b'}\sum_{xy}\Phi_{xy}(lb,l'b')U_x(qb)U_y(q'b')e^{i(ql+q'l')}.\end{aligned} \tag{2.30}$$

We can simplify the right-hand side of the Eqn.2.30 by operating the summation over l. The first term can be written as:

$$\hat{K} = \sum_{qq'b}\frac{P(qb).P(q'b)}{2m_b}\frac{1}{N_0\Omega}\sum_{l}e^{-i(q+q')l}.$$

Using the relation $\sum_l e^{-i(q+q').l} = N_0\Omega\delta_{q+q',0}$

$$\hat{K} = \sum_{qb}\frac{P(qb).P\dagger(qb)}{2m_b}. \tag{2.31}$$

Similarly, we can simplify the second term on the right side of Eqn. 2.30 using $h = l' - l$:

$$\hat{V}_2 = \frac{1}{2}\sum_{qbhb'}\sum_{xy}\Phi_{xy}(0b,hb)U_x(qb)U_y^{\dagger}(qb')e^{-iqh}, \tag{2.32}$$

where $U(qb)$ and $P(qb)$ are the Hermitian matrices. To further simplify we introduce $\Phi_{xy}(bb'|q)$:

$$\begin{aligned}\Phi_{xy}(bb'|q) &= \sum_{h}\Phi_{xy}(0b,hb')e^{-iqh} \\ &= \sqrt{m_b m_{b'}}D_{xy}(bb'|-q),\end{aligned} \tag{2.33}$$

where D_{xy} represents the dynamical matrix. Therefore, Eqn.2.32 can be rewritten as:

$$\hat{V}_2 = \frac{1}{2}\sum_{qbb'}\sum_{xy}\Phi_{xy}(bb'|q)U_x(qb)U_y^{\dagger}(qb'). \tag{2.34}$$

Putting Eqn.2.31 and Eqn.2.34 into Eqn.2.30, the harmonic Hamiltonian can be written as:

$$H^{harm} = \sum_{qb}\frac{P(qb).P\dagger(qb)}{2m_b} + \frac{1}{2}\sum_{qbb'}\sum_{xy}\Phi_{xy}(bb'|q)U_x(qb)U_y^{\dagger}(qb'). \tag{2.35}$$

We can further transform the normal coordinates $U(qb)$ and $P(qb)$ to use the phonon eigenvectors $e(b|\alpha q)$ which depends on the phonon vibrational modes (α) instead of atomic-position vectors (b). The transformation of $U(qb)$ and $P(qb)$ are given below:

$$U(\alpha q) = \sum_b \sqrt{m_b}e^*(b|\alpha q)U(qb), \tag{2.36}$$

$$P(\alpha q) = \sum_b \frac{1}{\sqrt{m_b}}e(b|\alpha q)P(qb). \tag{2.37}$$

To make our life easy, we introduce the phonon annihilation $(a_{\alpha q})$ and creation $(a_{\alpha q}^{\dagger})$ operators:

$$a_{\alpha q} = \frac{1}{\sqrt{2\hbar\omega(\alpha q)}}P(\alpha q) - i\sqrt{\frac{\omega(\alpha q)}{2\hbar}}U^{\dagger}(\alpha q), \tag{2.38}$$

$$a_{\alpha q}^{\dagger} = \frac{1}{\sqrt{2\hbar\omega(\alpha q)}}P^{\dagger}(\alpha q) + i\sqrt{\frac{\omega(\alpha q)}{2\hbar}}U(\alpha q). \tag{2.39}$$

The phonon annihilation and creation operators follow the commutation relation:

$$[a_{\alpha q}, a_{\alpha' q'}^{\dagger}] = \hat{I}\delta_{qq'}\delta_{\alpha\alpha'}. \tag{2.40}$$

The $U(\alpha q)$ and $P(\alpha q)$ can be written in terms of phonon annihilation and creation operators using $U^{\dagger}(\alpha q) = U(-\alpha q)$, $P^{\dagger}(\alpha q) = P(-\alpha q)$ and $\omega^{\dagger}(\alpha q) = \omega(-\alpha q)$:

$$U(\alpha q) = -i\sqrt{\frac{\hbar}{2\omega(\alpha q)}}(a_{\alpha q}^{\dagger} - a_{-\alpha q}) \tag{2.41}$$

$$P(\alpha q) = \sqrt{\frac{\hbar\omega(\alpha q)}{2}}(a_{\alpha q} + a_{-\alpha q}^{\dagger}), \tag{2.42}$$

so from Eqn.2.36, Eqn.2.37, Eqn.2.41, and Eqn.2.42, we have obtained the following equations for $U(qb)$ and $P(qb)$:

$$\begin{aligned} U(qb) &= \frac{1}{\sqrt{m_b}} \sum_{\alpha} e(b|\alpha q) U(\alpha q) \\ &= -i \sum_{\alpha} \sqrt{\frac{\hbar}{2 m_b \omega(\alpha q)}} e(b|\alpha q)(a^{\dagger}_{\alpha q} - a_{-\alpha q}), \end{aligned} \tag{2.43}$$

$$\begin{aligned} P(qb) &= \sqrt{m_b} \sum_{\alpha} e^{*}(b|\alpha q) P(\alpha q) \\ &= \sum_{\alpha} \sqrt{\frac{m_b \hbar \omega(\alpha q)}{2}} e^{*}(b|\alpha q)(a_{\alpha q} + a^{\dagger}_{-\alpha q}). \end{aligned} \tag{2.44}$$

We have substituted the Eqn.2.43 and Eqn.2.44 into Eqn.2.30 , the harmonic Hamiltonian can be written as:

$$\begin{aligned} H^{harm} &= \frac{1}{4} \sum_{\alpha q b} \hbar \omega(\alpha q) e(b|\alpha q) e^{*}(b|\alpha q)(a_{\alpha q} + a^{\dagger}_{-\alpha q})(a^{\dagger}_{\alpha q} + a_{-\alpha q}) \\ &+ \frac{1}{2} \sum_{qbb'} \sum_{\alpha xy} \Phi_{xy}(bb'|q) \frac{\hbar}{2\omega(\alpha q)} \frac{1}{\sqrt{m_b m_{b'}}} e_x(b|\alpha q) e^{*}_y(b'|\alpha q)(a^{\dagger}_{\alpha q} - a_{-\alpha q})(a_{\alpha q} - a^{\dagger}_{-\alpha q}). \end{aligned}$$

Substituting the Φ_{xy} as given in Eqn.2.33 and using the relation $D_{xy}(bb'|-q) = D^{*}_{xy}(bb'|q)$, we get the harmonic Hamiltonian as:

$$\begin{aligned} H^{harm} &= \frac{1}{4} \sum_{\alpha q b} \hbar \omega(\alpha q) e(b|\alpha q) e^{*}(b|\alpha q)(a_{\alpha q} + a^{\dagger}_{-\alpha q})(a^{\dagger}_{\alpha q} + a_{-\alpha q}) \\ &+ \frac{1}{2} \sum_{qb} \sum_{\alpha x} \frac{\hbar}{2\omega(\alpha q)} \left[\sum_{b'y} D^{*}_{xy}(bb'|q) e^{*}_y(b'|\alpha q) \right] e_x(b|\alpha q)(a^{\dagger}_{\alpha q} - a_{-\alpha q})(a_{\alpha q} - a^{\dagger}_{-\alpha q}). \end{aligned}$$

Using the eigenequation $\omega^2(\alpha q) e_x(b|\alpha q) = \sum_{b'y} D(bb'|q) e_y(b'|\alpha q)$ and the equality $\omega^2(\alpha q) = \omega^2(-\alpha q)$, we obtain:

$$
\begin{aligned}
H^{harm} = &\frac{1}{4}\sum_{\alpha q b}\hbar\omega(\alpha q)e(b|\alpha q)e^{*}(b|\alpha q)(a_{\alpha q}+a^{\dagger}_{-\alpha q})(a^{\dagger}_{\alpha q}+a_{-\alpha q}) \\
&+\frac{1}{4}\sum_{qb}\sum_{\alpha x}\hbar\omega(\alpha q)e^{*}_{x}(b|\alpha q)e_{x}(b|\alpha q)(a^{\dagger}_{\alpha q}-a_{-\alpha q})(a_{\alpha q}-a^{\dagger}_{-\alpha q}).
\end{aligned}
$$

We have realized that the summation over q is similar to summation over $-q$ and Eqn.2.24 and Eqn.2.25 are used to simplify the H^{harm} as:

$$
\begin{aligned}
H^{harm} = &\frac{1}{4}\sum_{\alpha q}\hbar\omega(\alpha q)\left[(a_{\alpha q}+a^{\dagger}_{-\alpha q})(a^{\dagger}_{\alpha q}+a_{-\alpha q})+(a^{\dagger}_{\alpha q}-a_{-\alpha q})(a_{\alpha q}-a^{\dagger}_{-\alpha q})\right] \\
= &\frac{1}{4}\sum_{\alpha q}\hbar\omega(\alpha q)(a_{\alpha q}a^{\dagger}_{\alpha q}+a^{\dagger}_{\alpha q}a_{\alpha q}+a_{-\alpha q}a^{\dagger}_{-\alpha q}+a^{\dagger}_{-\alpha q}a_{-\alpha q}) \\
= &\frac{1}{2}\sum_{\alpha q}\hbar\omega(\alpha q)(a_{\alpha q}a^{\dagger}_{\alpha q}+a^{\dagger}_{\alpha q}a_{\alpha q}).
\end{aligned}
\tag{2.45}
$$

Commutation relation of the phonon annihilation and creation operators given in Eqn.2.40 is used to get final form of the H^{harm} as:

$$
H^{harm} = \sum_{\alpha q}\hbar\omega(\alpha q)\left(a_{\alpha q}a^{\dagger}_{\alpha q}+\frac{1}{2}\right)
\tag{2.46}
$$

The method, we have used to obtained Eqn.2.46 is called second quantization because it contains a two-step transformation. In the first step, the atomic coordinates (lb) are replaced with wave vectors (αq). The annihilation ($a_{\alpha q}$) and creation ($a^{\dagger}_{\alpha q}$) operators are introduced in the second step. When we apply the harmonic Hamiltonian on a state $\left|n_{\alpha q}\right\rangle$ having n number of phonons in mode αq gives the total energy of phonons in that mode.

Anharmonic lattice dynamics

The harmonic approximation is precisely fulfilled in a classical system at zero Kalvin temperature, but it does not satisfy in the quantum systems. The atomic motion is increased with increasing the temperature, and the average spacing between atoms in a crystal is also increased due to the thermal expansion. This problem is solved by using quasi-harmonic lattice dynamics. The second problem is the infinite lifetime of the phonons because phonons do not interact with each other in harmonic approximation for a crystal[64, 67, 73]. This problem can be solved by including the higher-order terms in Hamiltonian which produced interaction between phonons and hence phonons have the finite lifetime. The anharmonic Hamiltonian can be expressed as:

$$H = H^{harm} + \frac{1}{3!}\sum_{lbl'b'l''b''}\sum_{xyz}\Psi_{xyz}(lb,l'b',l''b'')u_x(lb)u_y(l'b')u_z(l''b''). \tag{2.47}$$

We have taken the contributions up to third order term in Eqn.2.47. The higher order terms are not taken because their contributions are not significant at low temperature. Using Eqn.2.27 and Eqn.2.28, the Hamiltonian can be written as:

$$\begin{aligned} H =& H^{harm} + \frac{1}{3!}\frac{1}{(N_0\Omega)^{3/2}}\sum_{qq'q''}\sum_{lbl'b'l''b''}\sum_{xyz}\Psi_{xyz}(lb,l'b',l'',b'') \\ & U_x(qb)U_y(q'b')U_z(l''b'')e^{i(ql+q'l'+q''l'')} \\ =& H^{harm} + \hat{V}_3 \end{aligned} \tag{2.48}$$

New variables $h'' = l - l''$ and $h' = l - l'$ are introduced, the second term ($\hat{V}_3$) on the right side of Eqn.2.48 can be written as:

$$\begin{aligned} \hat{V}_3 =& \frac{1}{3!}\frac{1}{(N_0\Omega)^{3/2}}\sum_{qq'q''}\sum_{hbh'b'h''b''}\sum_{xyz}\sum_{l}e^{i(q+q'+q'').l}\Psi_{xyz}(0b,h'b',h''b'')e^{i(q'h'+q''h'')} \\ & \times U_x(qb)U_y(q'b')U_z(q''b'') \\ =& \frac{1}{3!}\frac{1}{(N_0\Omega)^{3/2}}\sum_{qq'q''}\sum_{bb'b''}\sum_{xyz}\sum_{l}e^{i(q+q'+q'').l}\Psi_{xyz}(qb,q'b',q''b'') \\ & \times U_x(qb)U_y(q'b')U_z(q''b''). \end{aligned} \tag{2.49}$$

Now, we solve the summation over l, Eqn.2.49 can be rewritten as:

$$\begin{aligned} \hat{V}_3 =& \frac{1}{3!}\frac{1}{\sqrt{N_0\Omega}}\sum_{qbq'b'q''b''}\delta_{G,q+q'+q''}\sum_{xyz}\Psi_{xyz}(qb,q'b',q''b'') \\ & \times U_x(qb)U_y(q'b')U_z(q''b''), \end{aligned} \tag{2.50}$$

where $\sum_l e^{i(q+q'+q'').l} = N_0\Omega\delta_{G,q+q'+q''}$ and here G represents the reciprocal lattice vector. The $U(qb)$ (in terms of phonon annihilation and creation operator) given in Eqn.2.41 is substituted in Eqn.2.50, the term $\hat{V}_3$ can be written as:

$$
\begin{aligned}
\hat{V}_3 = & \frac{1}{3!}\frac{i}{\sqrt{N_0\Omega}} \sum_{\alpha q\alpha' q'\alpha'' q''} \sum_{bb'b''}\sum_{xyz}\sqrt{\frac{\hbar^3}{8m_b m_{b'} m_{b''}\omega(\alpha q)\omega(\alpha' q')\omega(\alpha'' q'')}} \\
& \times \delta_{G,q+q'+q''}\Psi_{xyz}(qb,q'b',q''b'')e_x(b|\alpha q)e_y(b'|\alpha' q')e_z(b''|\alpha'' q'') \\
& \times (a^\dagger_{\alpha q} - a_{-\alpha q})(a^\dagger_{\alpha' q'} - a_{-\alpha' q'})(a^\dagger_{\alpha'' q''} - a_{-\alpha'' q''}). \qquad (2.51)
\end{aligned}
$$

To simplify the Eqn.2.51 , we introduce $\tilde{\Psi}$ and it is defined as:

$$
\begin{aligned}
\tilde{\Psi}(\alpha q, \alpha' q, \alpha'' q'') = & \frac{i}{\sqrt{N_0\Omega}}\sqrt{\frac{\hbar^3}{8\omega(\alpha q)\omega(\alpha' q')\omega(\alpha'' q'')}} \sum_{bb'b''}\sum_{xyz}\Psi_{xyz}(qb,q'b',q''b'') \\
& \times \frac{e_x(b|\alpha q)}{\sqrt{m_b}}\frac{e_y(b'|\alpha' q')}{\sqrt{m_{b'}}}\frac{e_z(b''|\alpha'' q'')}{\sqrt{m_{b''}}} \qquad (2.52)
\end{aligned}
$$

Plugin Eqn.2.52 into Eqn.2.51 , we get:

$$
\begin{aligned}
\hat{V}_3 = & \frac{1}{3!}\sum_{\alpha q\alpha' q'\alpha'' q''} \delta_{G,q+q'+q''}\tilde{\Psi}(\alpha q, \alpha' q, \alpha'' q'') \\
& \times (a^\dagger_{\alpha q} - a_{-\alpha q})(a^\dagger_{\alpha' q'} - a_{-\alpha' q'})(a^\dagger_{\alpha'' q''} - a_{-\alpha'' q''}). \qquad (2.53)
\end{aligned}
$$

The eigenstates of $a^\dagger_{\alpha q}a_{\alpha q}$ are not anymore the eigenstates of the anharmonic Hamiltonian, and thus, the solution to the anharmonic Hamiltonian is more difficult to find. To simplify the solution, we add anharmonic term as a perturbation to the harmonic Hamiltonian. This anharmonic term produces couplings between the phonons; therefore it is possible that a phonon can be excited from one mode to another by scattering with other phonons in the crystal. The detailed scattering mechanisms are explained in the following section 2.1.4.

2.1.4 Phonon scattering mechanisms

Inside a semiconducting/insulating crystal, phonons can be scattered by the other phonons, isotopes, and boundaries. At room temperature and above, three-phonon scattering rates are the dominant and boundary scattering rates are minimal. However, boundary scattering rates are dominated at low temperature. According to Matthiessen's rule, the total scattering rate is obtained from the sum of the individual scattering rates[64]. It can be written as:

$$
\frac{1}{\tau_t} = \frac{1}{\tau_{three-phonon}} + \frac{1}{\tau_{iso}} + \frac{1}{\tau_b}, \qquad (2.54)
$$

where $1/\tau_t$ is the total scattering rate, $1/\tau_{three-phonon}$ is the three-phonon scattering rate, $1/\tau_{iso}$ is the isotope scattering rate, and $1/\tau_b$ is the boundary scattering rate.

Three-phonon scattering processes

The phonon-phonon scattering is the principal mechanism defining heat transport by lattice vibrations in crystals. In this thesis, we will study only the three-phonon scattering processes that are sufficient to obtain the phonon lifetimes. The fourth-order terms have no imaginary part and, therefore, do not add to the phonon lifetime[67, 74, 75]. Three-phonon scattering rate can be obtained using the Fermi's golden rule. The transition probability, P_i^f , from initial state $|n_i\rangle$ to final state $|n_f\rangle$ due to three phonons scattering is given as[62]:

$$P_{n_i}^{n_f} = \frac{2\pi}{\hbar} \left|\langle n_f | \hat{V}_3 | n_i\rangle\right|^2 \delta(E_{n_f} - E_{n_i}), \tag{2.55}$$

where $\langle n_f | \hat{V}_3 | n_i\rangle$ represents the anharmonic matrix element of the Hamiltonian between initial and final states. E_{n_i} is the energy of the initial state, E_{n_f} is the energy of final state and $\delta(E_{n_i} - E_{n_f})$ represents the validation of the energy conservation. If we consider all possible initial and final states, then the number of transitions is substantial. However, The Fermi's golden rule takes particular combinations of final and initials states which have non-zero transition probability. The initial and final states of the three-phonon scattering processes are given as:

$$|n_i\rangle = |n_{\alpha q}, n_{\alpha' q'}, n_{\alpha'', q''}\rangle \tag{2.56}$$

$$|n_f\rangle = |n_{\alpha q} - 1, n_{\alpha' q'} - 1, n_{\alpha'' q''} + 1\rangle \tag{2.57}$$

$$|n_f\rangle = |n_{\alpha q} - 1, n_{\alpha' q'} + 1, n_{\alpha'' q''} + 1\rangle . \tag{2.58}$$

In the coalescence processes, two phonons diffuse into one phonon, while one phonon is split into two phonons in the decay processes as shown in Fig.2.1(a,b). The energy and momentum conservation laws must be obeyed in both processes[62].

For coalescence processes:

$$q + q' = q'' + G \tag{2.59}$$

$$\omega(\alpha q) + \omega(\alpha' q') = \omega(\alpha'' q''), \tag{2.60}$$

also, for decay processes:

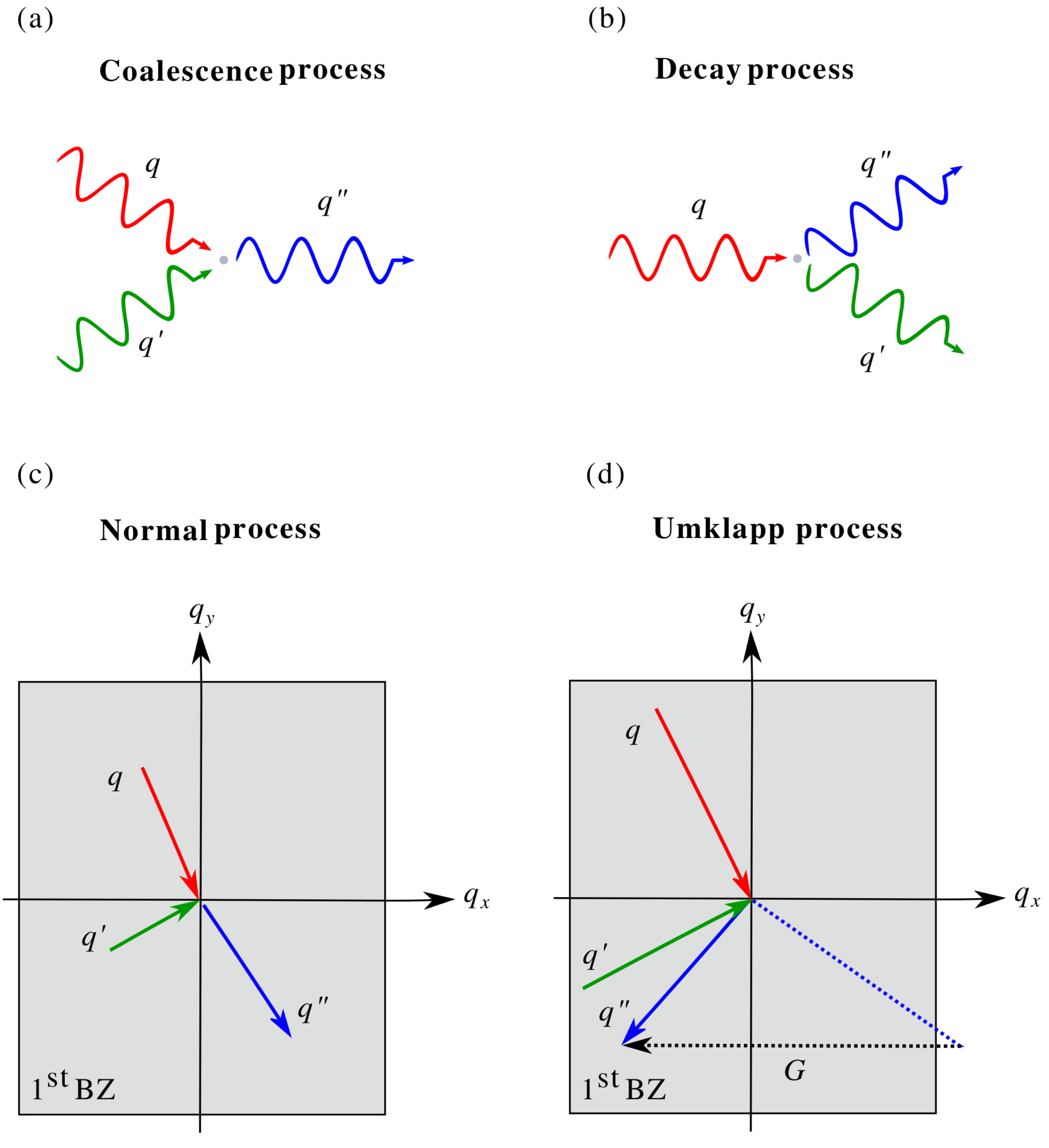
(a)
Coalescence process
q
q''
q'
(b)
Decay process
q
q''
q'
(c)
Normal process
q_y
q_x
q
q'
q''
1^{st} BZ
(d)
Umklapp process
q_y
q_x
q
q'
q''
G
1^{st} BZ

Figure 2.1: Three-phonon scattering (a) coalescence and (b) decay processes which obey the energy conservation law. (c) Normal and (d) Umklapp processes for the phonon coalescence scattering.

$$q + G = q' + q'' \tag{2.61}$$
$$\omega(\alpha q) = \omega(\alpha' q') + \omega(\alpha'' q''). \tag{2.62}$$

No transition is possible between the initial and final states if these laws are not obeyed. Peierls brought in a further difference between three-phonon scattering processes. The scattering process which strictly obeys the law of conservation of momentum ($G = 0$) is known as a normal process, whereas if the law of conservation of momentum is not strictly followed ($G \neq 0$) then it is called Umklapp process, and these processes are shown in Fig.2.1(c,d).

The transition probability for the coalescence processes can be expressed as:

$$\begin{aligned} P_{\alpha q,\alpha' q'}^{\alpha'' q''} = \frac{2\pi}{\hbar} \left| \langle n_{\alpha q} - 1, n_{\alpha' q'} - 1, n_{\alpha'' q''} + 1 \right| \hat{V}_3 \left| n_{\alpha q}, n_{\alpha' q'}, n_{\alpha'' q''} \rangle \right|^2 \\ \times \hbar \delta(\omega(\alpha'' q'') - \omega(\alpha' q') - \omega(\alpha q)). \end{aligned} \tag{2.63}$$

The value of $\hat{V}_3$ in Eqn.2.53 is plugin into Eqn.2.63 , we get $P_{\alpha q,\alpha' q'}^{\alpha'' q''}$ as:

$$\begin{aligned} P_{\alpha q,\alpha' q'}^{\alpha'' q''} =& 2\pi \Bigg| \frac{1}{3!} \sum_{\alpha q \alpha' q' \alpha'' q''} \delta_{G,-q-q'+q''} \tilde{\Psi}(-\alpha q, -\alpha' q', \alpha'' q'') \left\langle n_{\alpha q} - 1, n_{\alpha' q'} - 1, n_{\alpha'' q''} + 1 \right| \\ & (a_{\alpha q}^{\dagger} - a_{-\alpha q})(a_{\alpha' q'}^{\dagger} - a_{-\alpha' q'})(a_{\alpha'' q''}^{\dagger} - a_{-\alpha'' q''}) \left| n_{\alpha q}, n_{\alpha' q'}, n_{\alpha'' q''} \right\rangle \Bigg|^2 \\ & \times \delta(\omega(\alpha q) + \omega(\alpha' q') - \omega(\alpha'' q'')). \end{aligned} \tag{2.64}$$

The term $(a_{\alpha q}^{\dagger} - a_{-\alpha q})(a_{\alpha' q'}^{\dagger} - a_{-\alpha' q'})(a_{\alpha'' q''}^{\dagger} - a_{-\alpha'' q''})$ in Eqn.2.64 can be expanded as:

$$\begin{aligned} & a_{\alpha q}^{\dagger} a_{\alpha' q'}^{\dagger} a_{\alpha'' q''}^{\dagger} - a_{\alpha q}^{\dagger} a_{\alpha' q'}^{\dagger} a_{-\alpha'' q''} - a_{\alpha q}^{\dagger} a_{-\alpha' q'} a_{\alpha'' q''}^{\dagger} - a_{-\alpha q} a_{\alpha' q'}^{\dagger} a_{\alpha'' q''}^{\dagger} \\ & + a_{\alpha q}^{\dagger} a_{-\alpha' q'} a_{\alpha'' q''} + a_{-\alpha q} a_{\alpha' q'}^{\dagger} a_{-\alpha'' q''} + a_{-\alpha q} a_{-\alpha' q'} a_{\alpha'' q''}^{\dagger} - a_{-\alpha q} a_{-\alpha' q'} a_{-\alpha'' q''}. \end{aligned} \tag{2.65}$$

The only fifth term in Eqn.2.65 remains and all other terms become zero. The summation over $qq'q''$ in Eqn.2.64 gives 3! which cancel out by the 1/3!, the $P_{\alpha q,\alpha' q'}^{\alpha'' q''}$ can be written as:

$$\begin{aligned} P_{\alpha q,\alpha' q'}^{\alpha'' q''} =& 2\pi \left| \tilde{\Psi}(-\alpha q, -\alpha' q', \alpha'' q'') \right|^2 n_{\alpha q} n_{\alpha' q'} (n_{\alpha'' q''} + 1) \\ & \times \delta(\omega(\alpha q) + \omega(\alpha' q') - \omega(\alpha'' q'')). \end{aligned} \tag{2.66}$$

Similarly, we can express the transition probability for the decay processes as:

$$\begin{aligned} P_{\alpha q}^{\alpha' q', \alpha'' q''} =& 2\pi \left|\tilde{\Psi}(-\alpha q, \alpha' q', \alpha'' q'')\right|^2 n_{\alpha q}(n_{\alpha' q'}+1)(n_{\alpha'' q''}+1) \\ & \times \delta(\omega(\alpha q) - \omega(\alpha' q') - \omega(\alpha'' q'')). \end{aligned} \tag{2.67}$$

The net scattering rate is obtained from the difference between forward and backward scattering for coalescence and decay processes as:

$$\begin{aligned} P_{\alpha q, \alpha' q'}^{\alpha'' q''} - P_{\alpha'' q''}^{\alpha q, \alpha' q'} =& 2\pi \delta(\omega(\alpha q) + \omega(\alpha' q') - \omega(\alpha'' q'')) \left|\tilde{\Psi}(-\alpha q, -\alpha' q', \alpha'' q'')\right|^2 \\ & \left[n_{\alpha q} n_{\alpha' q'} (n_{\alpha'' q''}+1) - (n_{\alpha q}+1)(n_{\alpha' q'}+1) n_{\alpha'' q''}\right], \end{aligned} \tag{2.68}$$

$$\begin{aligned} P_{\alpha q}^{\alpha' q', \alpha'' q''} - P_{\alpha' q', \alpha'' q''}^{\alpha q} =& 2\pi \delta(\omega(\alpha q) - \omega(\alpha' q') - \omega(\alpha'' q'')) \left|\tilde{\Psi}(-\alpha q, \alpha' q', \alpha'' q'')\right|^2 \\ & \left[n_{\alpha q}(n_{\alpha' q'}+1)(n_{\alpha'' q''}+1) - (n_{\alpha q}+1) n_{\alpha' q'} n_{\alpha'' q''}\right]. \end{aligned} \tag{2.69}$$

The net scattering rate for the coalescence processes is zero at equilibrium, so the Eqn.2.68 can be written as:

$$n^0_{\alpha q} n^0_{\alpha' q'} (n^0_{\alpha'' q''}+1) = (n^0_{\alpha q}+1)(n^0_{\alpha' q'}+1) n^0_{\alpha'' q''}, \tag{2.70}$$

which can also be expressed as:

$$n^0_{\alpha' q'} - n^0_{\alpha'' q''} = \frac{n^0_{\alpha' q'}(n^0_{\alpha'' q''}+1)}{(n^0_{\alpha q}+1)}. \tag{2.71}$$

Similarly, the net scattering rate for the decay processes is also zero at equilibrium, so the Eqn.2.69 can be expressed as:

$$n^0_{\alpha q}(n^0_{\alpha' q'}+1)(n^0_{\alpha'' q''}+1) = (n^0_{\alpha q}+1) n^0_{\alpha' q'} n^0_{\alpha'' q''}, \tag{2.72}$$

the Eqn.2.72 can be rewritten as:

$$1 + n^0_{\alpha' q'} + n^0_{\alpha'' q''} = \frac{n^0_{\alpha' q'} n^0_{\alpha'' q''}}{n^0_{\alpha q}}. \tag{2.73}$$

Perturbed phonon population $n_{\alpha q}$ is expanded around equilibrium using first-order perturbation $\psi_{\alpha q}$:

$$n_{\alpha q} = \frac{1}{exp\left[\hbar\omega(\alpha q)/k_B T - \psi_{\alpha q}\right] - 1} \simeq n^0_{\alpha q} - \frac{\partial n^0_{\alpha q}}{\partial \omega(\alpha q)} \psi_{\alpha q}. \tag{2.74}$$

The Eqn.2.74 can be further simplified as:

$$n_{\alpha q} = n^0_{\alpha q} + n^0_{\alpha q}(n^0_{\alpha q}+1)\psi_{\alpha q}. \tag{2.75}$$

Eqn.2.75 is substituted in Eqn.2.68 and it gives:

$$P^{\alpha'' q''}_{\alpha q,\alpha' q'} - P^{\alpha q,\alpha' q'}_{\alpha'' q''} = \tilde{P}^{\alpha'' q''}_{\alpha q,\alpha' q'}(\psi_{\alpha q} + \psi_{\alpha' q'} - \psi_{\alpha'' q''}), \tag{2.76}$$

where

$$\begin{aligned}\tilde{P}^{\alpha'' q''}_{\alpha q,\alpha' q'} =& 2\pi n^0_{\alpha q} n^0_{\alpha' q'}(n^0_{\alpha'' q''}+1)\left|\tilde{\Psi}(-\alpha q,-\alpha' q',\alpha'' q'')\right|^2 \\ & \times \delta(\omega(\alpha q)+\omega(\alpha' q')-\omega(\alpha'' q'')),\end{aligned} \tag{2.77}$$

and substituting Eqn.2.75 in Eqn.2.69:

$$P^{\alpha' q',\alpha'' q''}_{\alpha q} - P^{\alpha q}_{\alpha' q',\alpha'' q''} = \tilde{P}^{\alpha' q',\alpha'' q''}_{\alpha q}(\psi_{\alpha q} - \psi_{\alpha' q'} - \psi_{\alpha'' q''}),$$

where

$$\begin{aligned}\tilde{P}^{\alpha' q',\alpha'' q''}_{\alpha q} =& 2\pi n^0_{\alpha q}(n^0_{\alpha q'}+1)(n^0_{\alpha'' q''}+1)\left|\tilde{\Psi}(-\alpha q,\alpha' q',\alpha'' q'')\right|^2 \\ & \times \delta(\omega(\alpha q)-\omega(\alpha' q')-\omega(\alpha'' q'')).\end{aligned}$$

The sum of the phonon transition probabilities gives the final phonon scattering rate due to the three-phonon interactions as:

$$\begin{aligned}\left.\frac{\partial n_{\alpha q}}{\partial t}\right|_{three-phonon} &= \sum_{\alpha' q' \alpha'' q''}\left[\left(P^{\alpha'' q''}_{\alpha q,\alpha' q'} - P^{\alpha q,\alpha' q'}_{\alpha'' q''}\right) + \frac{1}{2}\left(P^{\alpha' q',\alpha'' q''}_{\alpha q} - P^{\alpha q}_{\alpha' q',\alpha'' q''}\right)\right] \\ &= \sum_{\alpha' q' \alpha'' q''}\left[\tilde{P}^{\alpha'' q''}_{\alpha q,\alpha' q'}(\psi_{\alpha q}+\psi_{\alpha' q'}-\psi_{\alpha'' q''}) + \tilde{P}^{\alpha' q',\alpha'' q''}_{\alpha q}(\psi_{\alpha q}-\psi_{\alpha' q'}-\psi_{\alpha'' q''})\right],\end{aligned} \tag{2.78}$$

where we use the factor $1/2$ to prevent double counting during the summation. The scattering rate of a specific phonon mode does not depend on the other phonon mode perturbations under the RTA. Therefore, the perturbations due to the $\alpha' q'$ and $\alpha'' q''$ are set to zero ($\psi_{\alpha' q'} = \psi_{\alpha'' q''} = 0$) for calculating scattering rate of αq mode within RTA. Using Eqn.2.71 and Eqn.2.73 , the Eqn.2.78 can be written as:

$$\begin{aligned}\left.\frac{\partial n_{\alpha q}}{\partial t}\right|_{three-phonon} =& n^0_{\alpha q}(n^0_{\alpha q}+1)\psi_{\alpha q}\pi \sum_{\alpha' q' \alpha'' q''} \left|\tilde{\Psi}(-\alpha q, -\alpha' q', \alpha'' q'')\right|^2 \\ & \times [2(n^0_{\alpha' q'} - n^0_{\alpha'' q''})\delta(\omega(\alpha q)+\omega(\alpha' q')-\omega(\alpha'' q''))+ \\ & (1+n^0_{\alpha' q'}+n^0_{\alpha'' q''})\delta(\omega(\alpha q)-\omega(\alpha' q')-\omega(\alpha'' q''))]. \end{aligned} \tag{2.79}$$

The Eqn.2.79 can be simplified using the Eqn.2.75 as:

$$\begin{aligned}-\left.\frac{\partial n_{\alpha q}}{\partial t}\right|_{three-phonon} &= \frac{n^0_{\alpha q}(n^0_{\alpha q}+1)\psi_{\alpha q}}{\tau_{\alpha q}} \\ &= \frac{n_{\alpha q}-n^0_{\alpha q}}{\tau_{\alpha q}},\end{aligned}$$

which represents that the perturbed phonon population is decayed exponentially to equilibrium. The phonon relaxation time ($\tau_{three-phonon}$) can be written as:

$$\begin{aligned}\frac{1}{\tau_{three-phonon}} =& \pi \sum_{\alpha' q' \alpha'' q''} \left|\tilde{\Psi}(-\alpha q, -\alpha' q', \alpha'' q'')\right|^2 \\ & \times [2(n^0_{\alpha' q'} - n^0_{\alpha'' q''})\delta(\omega(\alpha q)+\omega(\alpha' q')-\omega(\alpha'' q''))+ \\ & (1+n^0_{\alpha' q'}+n^0_{\alpha'' q''})\delta(\omega(\alpha q)-\omega(\alpha' q')-\omega(\alpha'' q''))]. \end{aligned} \tag{2.80}$$

The terms $\delta(\omega(\alpha q)+\omega(\alpha' q')-\omega(\alpha'' q''))$ and $\delta(\omega(\alpha q)-\omega(\alpha' q')-\omega(\alpha'' q''))$ in Eqn.2.80 represent the phonon coalescence and decay processes, and the three-phonon scattering processes are calculated from the anharmonic force constants. In RTA, both the normal and Umklapp processes are completely resistive because G vector restricts the phonons within the first Brillouin zone while calculating transitions rates to get Eqn.2.80. Therefore, lattice thermal conductivity is underestimated in the RTA method as compared to an iterative solution of BTE. The difference between the RTA and iterative solutions are very small for the materials in which the Umklapp phonon scattering is dominated i-e κ_l materials.

Phonon-isotope scattering

All atoms of each atomic species have the same mass in the ideal crystal, but they are not the same in the real crystal because stable isotopes (mass-disorder) exist. The existence of the isotopes vanishes the translational symmetry of the crystal which induces phonon scattering. The effect of isotopes is minimal, and isotope can be considered as a perturbation in which the real crystal is replaced with an ordered virtual crystal[60, 64, 70, 76, 77]. This method is known as virtual crystal approximation (VCA), and the Hamiltonian for the virtual crystal can be written as:

$$\begin{aligned} H =& \frac{1}{2}\sum_{lbx} m(lb)\dot{u}_x^2(lb) + \hat{V}_2 \\ =& H_0 + H_{iso}, \end{aligned} \tag{2.81}$$

where H_0 represents the Hamiltonian for the virtual crystal or unperturbed Hamiltonian, and H_{iso} denotes the perturbation due to the isotopes in the crystal. The unperturbed Hamiltonian is given as:

$$H_0 = \frac{1}{2}\sum_{lbx} \bar{m}(b)\dot{u}_x^2(lb) + \hat{V}_2, \tag{2.82}$$

where $\bar{m}(b)$ is the average mass of atom b. The $\bar{m}(b)$ is defined as:

$$\bar{m}(b) = \sum_i f_i(b) m_i(b), \tag{2.83}$$

where f_i denotes the concentration of species i. The perturbation term H_{iso} is defined as:

$$\begin{aligned} H_{iso} =& \frac{1}{2}\sum_{lbx} (m(lb) - \bar{m}(b))\dot{u}_x^2(lb) \\ =& \frac{1}{2}\sum_{lbx} \Delta m(lb)\dot{u}_x^2(lb), \end{aligned} \tag{2.84}$$

where $\Delta m(lb) = m(lb) - \bar{m}(b)$ represents the difference between real crystal mass and virtual crystal mass. The first derivative of the displacement $\dot{u}_x(lb)$ is calculated using the Eqn.2.19 for the atomic displacements. The Eqn.2.84 can be written as:

$$\begin{aligned} H_{iso} = -\frac{\hbar}{4} \sum_{b\alpha\alpha'} \sum_{qq'} \sum_{l} \sqrt{\omega(\alpha q)\omega(\alpha' q')} \frac{\Delta m(lb)}{N_0 \bar{m}(b)} \\ \times e(b|\alpha q) e(b|\alpha' q') [a_{-\alpha q} a^{\dagger}_{\alpha' q'} + a^{\dagger}_{\alpha q} a_{\alpha' q'}] e^{i(ql + q'l)}. \end{aligned} \tag{2.85}$$

The Fourier transform of the $\Delta M = \Delta m(lb)/\bar{m}(b)$ is introduced as:

$$\Delta \tilde{M}_b(Q) = \frac{1}{N_0} \sum_l \Delta M(lb) e^{-iQl}. \tag{2.86}$$

Using the above transformation, we can write ΔM as:

$$\Delta M = \frac{\Delta m(lb)}{\bar{m}(b)} = N_0 \sum_{Q} \Delta\tilde{M}_b(Q) e^{iQl} \tag{2.87}$$

We have replaced $\Delta m(lb)/\bar{m}(b)$ with the Eqn.2.87 in Eqn.2.85 to write H_{iso} as:

$$\begin{aligned} H_{iso} = &\sum_{b\alpha\alpha'} \sum_{qq'Q} \sum_{l} \sqrt{\omega(\alpha q)\omega(\alpha' q')} \Delta\tilde{M}_b(Q) \\ &\times e(b|\alpha q) e(b|\alpha' q') [a_{-\alpha q} a^{\dagger}_{\alpha' q'} + a^{\dagger}_{\alpha q} a_{\alpha' q'}] e^{i(q+q'+Q)l}. \end{aligned} \tag{2.88}$$

We have applied summation over l and get:

$$\begin{aligned} H_{iso} = &\sum_{b\alpha\alpha'} \sum_{qq'Q} \sqrt{\omega(\alpha q)\omega(\alpha' q')} \Delta\tilde{M}_b(Q) \delta(q+q'+Q) \\ &\times e(b|\alpha q) e(b|\alpha' q') [a_{-\alpha q} a^{\dagger}_{\alpha' q'} + a^{\dagger}_{\alpha q} a_{\alpha' q'}]. \end{aligned} \tag{2.89}$$

The perturbed Hamiltonian in Eqn.2.89 is substituted into the Fermi's golden rule as given in Eqn.2.55 and carrying out the algebra (as we did in three-phonon scattering case in Sec.2.1.4), the phonon-isotope scattering can be obtained as:

$$\frac{1}{\tau_{iso}} = \frac{\pi}{2} \omega^2(\alpha q) \sum_{\alpha' q'} \left| \sum_{bQ} \Delta\tilde{M}_b(Q) e(b|\alpha q) e*(b|\alpha' q') \delta(q-q'+Q) \right|^2 \delta(\omega - \omega(\alpha' q')). \tag{2.90}$$

The mass variance parameter $m_i^{(2)}(b)$ can be defined as:

$$m_i^{(2)}(b) = \sum_i f_i(b) \left(\frac{\bar{m}(b) - m(b)}{\bar{m}(b)} \right)^2 . \tag{2.91}$$

The mass variance parameter is obtained from the ensemble average of the random distribution of masses as:

$$\begin{aligned} \left\langle \Delta M(lb) \Delta M(l'b') \right\rangle_{avg} &= \left\langle (\Delta M(lb))^2 \right\rangle_{avg} \delta_{ll'} \delta_{bb'} \\ &= m_i^{(2)}(b) \delta_{ll'} \delta_{bb'}. \end{aligned} \tag{2.92}$$

We use the above equation to obtained $\left|\Delta\tilde{M}_b(Q)\right|^2$ in term of $m_i^{(2)}(b)$ as:

$$\begin{aligned}\left|\Delta\tilde{M}_b(Q)\right|^2 =& \Delta\tilde{M}_b(Q)\Delta\tilde{M}_{b'}(Q') \\ =& \frac{1}{N_0}\sum_{ll'}\Delta M(lb)\Delta M(l'b')e^{-i(Ql-Q'l')} \\ =& \frac{1}{N_0}\sum_{ll'} m_i^{(2)}(b)\delta_{bb'}e^{-i(Ql-Q'l')}\delta_{ll'} \\ =& \frac{1}{N_0}m_i^{(2)}\delta_{bb'}\Delta(Q-Q'). \end{aligned} \tag{2.93}$$

We have substituted Eqn.2.93 in Eqn.2.90 and obtained as:

$$\frac{1}{\tau_{iso}} = \frac{\pi}{2N_0}\omega^2(\alpha q)\sum_{\alpha' q'}\delta(\omega-\omega(\alpha' q'))\sum_b m_i^{(2)}(b)\left|e(b|\alpha q)e*(b|\alpha' q')\right|^2. \tag{2.94}$$

The Eqn.2.94 represents the phonon-isotope scattering rate and it can be obtained for the crystal structure where mass disorder exists due to the different isotopes.

Phonon-boundary scattering

In the polycrystalline material, the phonon means free path (MFP) exceeds the grain size at the low temperature. At the low-temperature range, the phonons are scattered at the grain boundaries various times before they are scattered with another phonons or isotopes. Therefore, phonon-boundary scattering is very prominent at the low temperature. The expression for the phonon-boundary scattering is derived as[60, 62, 78]:

$$\frac{1}{\tau_b} = \frac{v_{\alpha q}}{L}, \tag{2.95}$$

where $v_{\alpha q}$ is the phonon group velocity, and L is the average grain size. This equation considers completely diffusive nature of the scattering, i.e. all incoming phonons are absorbed and re-emitted at the grain boundaries. This model gives a good approximation for the materials where phonon-boundary scattering occurs uniformly all over the volume. This condition can be fulfilled in the polycrystalline materials with a small acoustic mismatch between the grains. For the more accurate calculation of the κ_l, the surface roughness must be considered in the phonon-boundary scattering. The phonon-boundary scattering can be estimated as:

$$\frac{1}{\tau_b} = \frac{1-p}{1+p}\frac{v_{\alpha q}}{L},$$

where p denotes the specularity parameter which describes the effect of surface roughness on the phonon-boundary scattering. It is zero for the completely rough surface and one for the perfectly smooth surface.

2.2 Density functional theory

The Schrödinger equation was formulated in the 1920's which opens the ways to investigate the electrical, magnetic, mechanical and optical properties of the materials without knowledge of the experimental and empirical data and it is dependent on the sole information of the constituent atoms[79]. However, it is challenging to solve exactly for the systems including two or more interacting particles. Several numerical methods, like the variational method, the perturbation theory, the Quantum Monte Carlo method and semi-classical expansion, have been developed to approximate the solution of the many-body Schödinger equation. Among these approaches, density functional theory (DFT) is broadly used because of its high accuracy and required low computational power. The main aim of DFT is to decrease the complication of the many-body problem by using the electron density as a primary variable to describe the many-body effects in a single particle formalism. DFT is comprehensively studied in many of excellent books[80–83] and review articles[84–87].

2.2.1 The many-body Schrödinger equation

To understand the material properties from the quantum mechanical approaches is based on solving the many-body nonrelativistic time-independent Schrödinger equation and it can be written as:

$$\hat{H}\Psi = E\Psi, \tag{2.96}$$

where $\hat{H}$, Ψ, and E are the many-body Hamiltonian, many-body wavefunction and ground state energy of the system, respectively. The many-body wavefunction relies on the all electrons and nuclei coordinates, and it can be expressed for N electrons and M nuclei as:

$$\Psi = \Psi(r_1, r_2, ..., r_N; R_1, R_2, ..., R_M). \tag{2.97}$$

The many-body Hamiltonian can be written as:

$$\begin{aligned}\hat{H} = &-\sum_i \frac{\hbar^2}{2m_e}\nabla_i^2 - \sum_I \frac{\hbar^2}{2M_I}\nabla_I^2 + \frac{1}{2}\sum_{i\neq j}\frac{e^2}{4\pi\varepsilon_0}\frac{1}{|r_i - r_j|} \\ &+ \frac{1}{2}\sum_{I\neq J}\frac{e^2}{4\pi\varepsilon_0}\frac{Z_I Z_J}{|R_I - R_J|} - \sum_{i,I}\frac{e^2}{4\pi\varepsilon_0}\frac{Z_I}{|r_i - R_J|},\end{aligned} \tag{2.98}$$

where i and j are the indexes for the valence electrons, I and J are the indexes for the ions, m_e and r_i are masses and positions of the electrons, M_I and R_I are masses and positions of the ion, and Z_I and Z_J are the atomic (charge) number of the nucleus I and J, respectively. The first two terms represent the kinetic energy (K.E) of the electrons and ions respectively. Third and fourth terms are the electron-electron Coulomb interaction and ion-ion Coulomb interaction, respectively. The final term is the Coulomb interaction between the electron and the ion. To simplify the many-body Hamiltonian given in Eq.2.98, Hartree atomic units ($\hbar = m_e = e = \frac{1}{4\pi\varepsilon_0} = 1$) are introduced. The Eq.2.98 can be written as:

$$\begin{aligned}\hat{H} = &-\sum_i \frac{\nabla_i^2}{2} - \sum_I \frac{\nabla_I^2}{2M_I} + \frac{1}{2}\sum_{i\neq j}\frac{1}{|r_i - r_j|} \\ &+ \frac{1}{2}\sum_{I\neq J}\frac{Z_I Z_J}{|R_I - R_J|} - \sum_{i,I}\frac{Z_I}{|r_i - R_J|}.\end{aligned} \tag{2.99}$$

The solution of the Eq.2.99 is only possible for a minimal system because of the electron-electron Coulomb interaction. The complication of the solution to Eq.2.99 rises exponentially with the size of a system, and therefore, appropriate approximations are required[85].

2.2.2 Born-Oppenheimer approximation

The Born-Oppenheimer or the adiabatic approximation is established on the fact that the ions are more massive than the electrons, so the electrons are responded faster than the ions. This approximation decreases the complication of the Schrödinger equation by decoupling the movement of electrons and nuclei[88]. In this approximation, the nuclei have fixed positions with an infinite effective mass. It makes dramatic changes in the Hamiltonian as the K.E of the ion can be ignored, and the ion-ion Coulomb interaction becomes a constant. By considering the nuclear coordinates as extrinsic parameters and the wavefunction as relying only on electronic positions. The electronic Schrödinger equation without ionic coordinates can be expressed as:

$$\left[-\sum_i \frac{\nabla_i^2}{2} + \sum_i V_n(r_i) + \frac{1}{2}\sum_{i\neq j} \frac{1}{|r_i - r_j|}\right]\Psi_e = E_e\Psi_e, \tag{2.100}$$

where Ψ_e is the electronic wavefunction and E_e and $V_n(r)$ are defined as:

$$E_e = E - \frac{1}{2}\sum_{I\neq J} \frac{Z_I Z_J}{|R_I - R_J|},$$

and

$$V_n(r) = -\sum_I \frac{Z_I}{|r - R_I|}.$$

2.2.3 Independent electron approximation

In this approximation, electron-electron Coulomb interaction is ignored, the many-body Schrödinger equation can be reformulated as a set of single electron Schrödinger equations:

$$\hat{H}_0\phi_i(r_i) = \varepsilon_i\phi_i(r_i), \tag{2.101}$$

where $\hat{H}_0$ and ϕ_i are the single electron Hamiltonian and wavefunction. The single electron Hamiltonian can be written as:

$$\hat{H}_0 = -\frac{\nabla_i^2}{2} + V_n(r), \tag{2.102}$$

and many electrons wavefunctions can be decoupled into single electron wavefunctions as:

$$\Psi_e(r_1, r_2, ..., r_N) = \phi_1(r_1)\phi_2(r_2)...\phi_N(r_N). \tag{2.103}$$

These non-interacting single electron Schrödinger equations are very simpler to solve compared to Eq.2.100. The sum of the electron finding probabilities in each state is the electronic charge density in this approximation and it can be written as:

$$n(r) = \sum_i |\phi_i(r)|^2. \tag{2.104}$$

However, the approximation does not justified because electron-electron is missing which should not be ignored in any meaningful calculation.

2.2.4 Hartree and Hartree-Fock approximation

Hartree introduced an improved version of the independent electron approximation in 1928. He added new potential energy term called Hartree potential (V_H) to the single electron Hamiltonian[89]. The Hartree potential satisfies Poisson's equation

$$\nabla^2 V_H(r) = -4\pi n(r), \tag{2.105}$$

with the Hartree potential solution

$$V_H(r) = \int dr' \frac{n(r')}{|r-r'|}. \tag{2.106}$$

Now, the single electron Schrödinger equation can be written as:

$$\left[-\frac{\nabla^2}{2} + V_n(r) + V_H(r)\right] \phi_i(r) = \varepsilon_i \phi_i(r). \tag{2.107}$$

The total electron wavefunction (Ψ_H) in Hartree approximation is similar to Eq.2.103 and it can be written as:

$$\Psi_e^H(r_i) = \phi_1(r_1)\phi_2(r_2)...\phi_N(r_N). \tag{2.108}$$

However, the Hartree approximation didn't consider the anti-symmetric nature of the wavefunction. In the Hartree-Fock approximation, the anti-symmetric nature of the wavefunction is taken into account and the many-body wavefunction can be expressed as a Slater determinant:

$$\Psi_e^{HF}(r_i) = \frac{1}{N!} det\{\phi_1(r_1)\phi_2(r_2)...\phi_N(r_N)\}. \tag{2.109}$$

The Hartree-Fock approximation contains exchange effects but ignores the correlation effects.

2.2.5 Hohenberg-Kohn theorems

The DFT is based on the two theorems given by Hohenberg and Kohn in 1964[90]. These theorems are stated that:

Theorem I: The external potential ($V_{ext}(r)$) for any interacting fermions system is uniquely determined (up to a constant) from its ground state particle density ($n_0(r)$).

Theorem II: The ground state energy can be determined variationally, the particle density $n(r)$ that minimizes the universal energy functional $E[n(r)]$, is the exact ground state density

$n_0(r)$.

According to the first theorem, many-body Hamiltonian and wavefunctions for all states can be determined from the ground state density. So the ground state density is required to obtain all the properties of the system. The second theorem explains that the universal energy functional is needed to calculate the exact ground state density and energy. However, the universal functional is not known. Therefore, the Kohn-Sham equations are required to calculate the universal energy functional.

2.2.6 The Kohn-Sham equations

The success of DFT depends on the approach suggested by Kohn and Sham in 1965. In this approach, the many-body system, where the particles interact with each other, is replaced by an auxiliary system (particles do not interact but moving through a potential called Kohn-Sham potential (V_{KS})) and it is supposed that the ground state density is the identical for both systems[91]. The ground state total energy of the many-electron system can be expressed as a functional of the electron density:

$$E[n] = F[n] = \int drn(r)V_n(r) + T_s[n(r)] + \left\langle \Psi_e[n] \left| \hat{T} + \hat{W} \right| \Psi_e[n] \right\rangle, \tag{2.110}$$

where $\hat{T}$ is the kinetic energy, and it can be written as:

$$\hat{T} = -\sum_i \frac{\nabla_i^2}{2}, \tag{2.111}$$

and the Coloumb energy, $\hat{W}$, can be expressed as:

$$\hat{W} = \frac{1}{2}\sum_{i \neq j} \frac{1}{\left|r_i - r_j\right|}. \tag{2.112}$$

The potential experienced by the electrons due the nuclei is dependent on the particle density but the other terms in energy functional only implicitly rely on the particle density. Kohn and Sham divide these terms into Coloumb energy and kinetic energy of separate electrons and add an extra term which takes into account for any difference called exchange and correlation energy (E_{xc}). The energy functional can be written as:

$$F[n] = \int drn(r)V_n(r) + \hat{T}[n(r)] + E_H[n(r)] + E_{xc}[n(r)]. \tag{2.113}$$

The exchange and correlation term includes all contributions, which are not enclosed by the independent electron approximation, to the energy functional. Kohn and Sham minimized the universal energy functional with respect particle density ($\frac{\delta F[n]}{\delta n} = 0$) under the condition that one-particle wavefunctions are orthogonal to each other, ie. $\langle \phi_i | \phi_j \rangle = \delta_{ij}$. The N one particle equations can be derived as:

$$\hat{H}_{KS}\phi_i(r) = \varepsilon_i \phi_i(r), \tag{2.114}$$

where the Hamiltonian $\hat{H}_{KS}$ is defined as:

$$\hat{H}_{KS} = -\frac{1}{2}\nabla^2 + V_{KS}(r), \tag{2.115}$$

where V_{KS} represents the Kohn-Sham potential and it can be expressed as:

$$\begin{aligned} V_{KS}(r) =& V_n(r) + \frac{\delta E_H}{\delta n(r)} + \frac{\delta E_{xc}}{\delta n(r)} \\ =& V_n(r) + V_H(r) + V_{xc}(r). \end{aligned} \tag{2.116}$$

These equations 2.114, 2.115, and 2.116 are called Kohn-Sham equations. The Kohn-Sham equations reduce the effort of solving a complicated many-body system to independent-electron system existing in an effective potential.

2.2.7 Exchange-correlation approximations

The exact exchange-correlation functional is not known, and so proper approximations are needed. The local density approximation and the generalized gradient approximation are commonly used as an exchange-correlation functional[84, 92–94].

Local density approximation

The local density approximation (LDA) was the first effort to compute the exchange-correlation energy, and it is strongly interrelated to the homogeneous electron gas (HEG) model presented by Fermi and Thomas in 1920s. In this method, the exchange and correlation energy can be calculated by considering local electronic density only. It can be written as:

$$E_{xc}^{LDA}[n(r)] = \int drn(r)\varepsilon_{xc}[n(r)], \tag{2.117}$$

where ε_{xc} is the exchange-correlation energy per electron of a the HEG of density $n(r)$. The term ε_{xc} can be divided into the exchange and correlation parts, $\varepsilon_{xc} = \varepsilon_x + \varepsilon_c$. The exchange energy per electron in HEG model is provided by a simple analytic form:

$$\varepsilon_x = -\frac{3}{4}\left(\frac{3}{\pi}\right)^{\frac{1}{3}} n^{\frac{1}{3}}. \tag{2.118}$$

The exchange energy for LDA is given as:

$$E_x^{LDA}[n(r)] = -\frac{3}{4}\left(\frac{3}{\pi}\right)^{\frac{1}{3}} \int drn(r)^{\frac{4}{3}}. \tag{2.119}$$

The correlation energy for LDA has been computed to very high precision by Ceperley and Alder[84]. Later, It has been calculated by various groups, and the correlation energy generated by Perdew and Zunger[92] are the most famous and commonly used in the DFT calculations. The LDA is more suitable for the systems where the density changes slowly.

Generalized gradient approximation

The LDA is more suitable for the systems where the density changes slowly. In systems where the electron density is inhomogeneous, efforts have been made to improve the LDA called as generalized gradient approximation (GGA). The inhomogeneities of the electron density can be accurately explained by including density gradient corrections ($\nabla n(r)$) and higher derivative of the density. The GGA exchange and correlation energy can be written as:

$$E_{xc}^{GGA}[n(r)] = \int \varepsilon_{xc}^{GGA}[n(r), |\nabla n(r)|]n(r)dr. \tag{2.120}$$

The GGA predicts better binding energies and bond lengths compared to the LDA for the systems where charge density changes rapidly. Perdew and Wang first proposed it in 1991 known as PW91[94]. Later, Perdew, Burke and Ernzerhof[95] known as PBE generated this functional using different parameterization and the physics and chemistry community commonly use it.

2.2.8 Pseudopotentials

The wavefunction of the deep core electrons (closed shell electrons) are tightly bonded to the nuclei in the solid-state systems, and their distribution remains unaffected by changing the chemical environment. However, the electrons in the valence shell are highly energetic and strongly affected by the neighboring atoms. Therefore, the valence electrons are determined most of the interesting physical properties of solids rather than the closed shell electrons. At the same time, the core electrons description require a considerable amount of basis functions which consume enough computation time. To overcome this problem, the pseudopotential approximation changes the strong Coloumb potential with a weaker pseudopotential.

In general, pseudopotential formalism should satisfy the two conditions. The first condition is the use of a much weaker pseudopotential to replace core electrons and the second condition is to remove the papid oscillations of the valence electrons wavefunctions in the core region. Furthermore, it is also required within the pseudopotential scheme that the pseudo wavefunction and pseudopotential follow the all-electron behavior beyond the core region with the same eigenvalues of the many-body Schrödinger equation as shown in Fig.2.2. Many different approaches are used to generate the pseudopotential from first-principles, such as ultrasoft pseudopotentials (USPPs)[96, 97], norm conservating pseudopotentials (NCPPs)[98, 99] and projector augmented wave (PAW) potentials. We have used the PAW method in this work[100, 101].

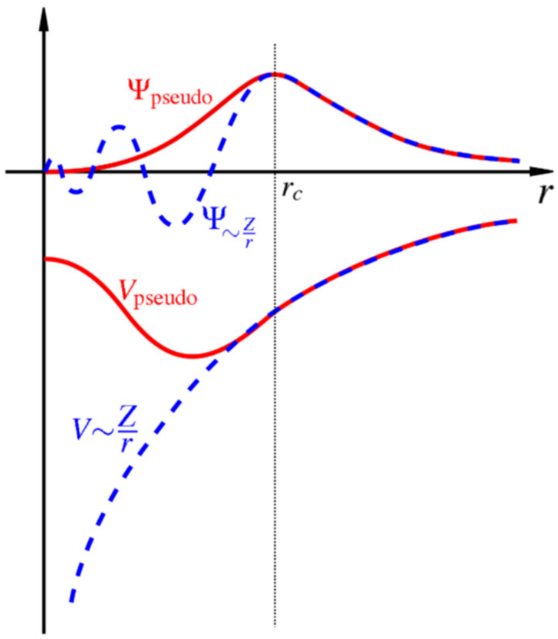
Ψ_{pseudo}
$\Psi_{\sim\frac{Z}{r}}$
r_c
r
V_{pseudo}
$V \sim \frac{Z}{r}$

Figure 2.2: Comparison of a wavefunction within the strong Coloum potential of the nucleus (blue dotted lines) to the one within pseudopotential (solid red lines). The real and pseudopotential meet beyond the cutoff radius r_c. This figure is adapted from ref. [102]

Chapter 3

Thermoelectric and phonon transport properties of two–dimensional IV–VI compounds

3.1 Introduction

Renewable energy is a very important field due to the insufficiency of natural energy source and global warming[103]. One of the best renewable energy sources is waste heat, which can be converted into electricity via the Seebeck effect[104, 105]. The performance of thermoelectric materials is measured by a dimensionless quantity ZT called the figure of merit[106, 107]:

$$ZT = \frac{\sigma S^2}{\kappa} T \tag{3.1}$$

where σ, S, κ, and T are electrical conductivity, Seebeck coefficient, thermal conductivity, and temperature, respectively. The lattice thermal conductivity κ_l and the electronic thermal conductivity κ_e are included in the thermal conductivity κ in eq. 3.1. A large Seebeck coefficient, large electrical conductivity, and low thermal conductivity are needed for high thermoelectric performance, but a low amount of charge carrier is required to improve the Seebeck coefficient, which reduces the electrical conductivity[108].

Improving ZT has been a big challenge, and different approaches have been used. Semiconductors composed of heavy elements such as Zn_4Sb_3 , PbTe and BiSb have been used to reduce the thermal conductivity[44, 45, 109]. Point defects (R_{1-y} $Fe_{4-x}Co_xSb_{12}$ and $Ce_yFe_xCo_{4-x}Sb_{12}$) have been produced to decrease the lattice thermal conductivity and the optimized electrical conductivity[46, 110]. Some bulk complex materials also show very good thermoelectric performance such as filled skutterudites ($La_{0.9}Fe_3CoSb_{12}$), half-Heusler alloys ($ZrCoSn_xSb_{1-x}$), and clathrates ($Sr_8Ga_{16}Ge_{30}$) because of their low thermal conductivity and high periodicity in the crystal structure[47, 111–114]. Zhao *et al*. recently reported that bulk SnSe is a very good thermoelectric material with a ZT of 2.6 at 973 K[115]. It was theoretically predicted that bulk SnS, GeSe, and GeS would also show very good thermoelectric performance[116].

One of the efficient methods to increase ZT is reducing the dimensionality of the material, which increases the Seebeck coefficient due to the increased density of states near the Fermi level[48, 117, 118]. It is reported that the reduction in dimensionality enhances the energy storage and conversion[119], the ZT of bulk Bi_2Te_3 is improved 13 times by converting into the quantum well. Fei *et al*. and Cheng *et al*. reported that a bismuth monolayer and phosphorene showed very promising thermoelectric properties[120, 121].

We studied two-dimensional SnSe, SnS, GeSe, and GeS materials for thermoelectric applications. Monolayers of these materials have already been experimentally synthesized, and they have band gaps less than 2 eV[122–125]. They have been recently reported to have low lattice thermal conductivity as well[126], which is a requirement for efficient thermoelectric materials. Group IV–VI compounds in bulk form have very good thermoelectric efficiency and a simple orthorhombic SnSe crystal was reported to have outstanding thermoelectricity[115, 116, 127]. It was recently discovered that even a monolayer of SnSe shows optimal thermoelectric properties[128], which motivateed us to study the thermoelectric properties of monolayer IV–VI compounds SnSe, SnS, GeSe, and GeS.

3.2 Methodology

Our calculations are based on density functional theory combined with Boltzmann transport theory and were performed using the Vienna Ab initio Simulation Package (VASP) and the Boltztrap code[101, 129, 130]. The generalized gradient approximation proposed by Perdew-Burke-Ernzerhof was chosen as an electronic exchange correlation functional[131]. The vdW-DF scheme is used to include the van der Waals interaction[132]. A Monkhorst mesh of $10\times10\times1$ k-points is used for lattice optimization and 450 eV is used as a plane wave cutoff energy. Structures are optimized until the Hellmann–Feynman force on each atom is less than 0.001 eV/Å. A vacuum region of 15 Å in the z-direction is produced to avoid the interaction between periodic images.

Thermoelectric properties were computed by solving the Boltzmann transport equation under a constant relaxation time (τ) and a rigid band approximation performed in the Boltztrap code[130]. We used a very dense k-point mesh of $60\times60\times1$ to obtain convergent density of states. The Seebeck coefficient $S(T,n)$, electrical (σ/τ) and electronic thermal (κ_e/τ) conductivities devided by the relaxation time were calculated. Boltztrap code used Wiedemann-Franz

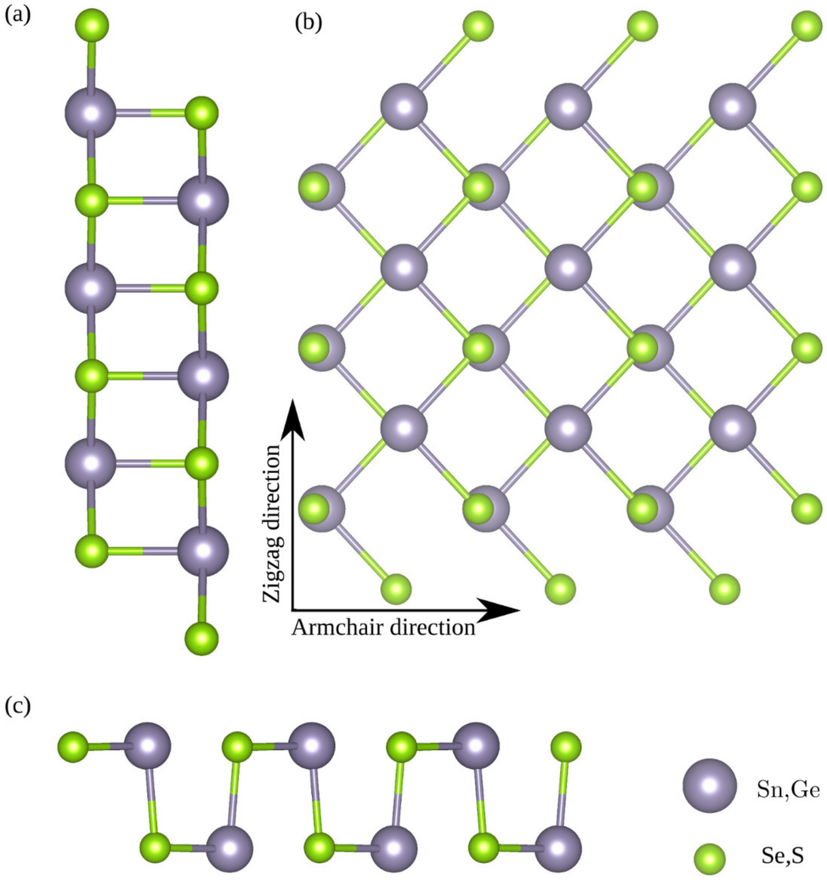
(a)
(b)
Zigzag direction
Armchair direction
(c)
Sn,Ge
Se,S

Figure 3.1: Crystal structure of two-dimensional monochalcogenides SnSe, SnS, GeSe, and GeS. (a) Side view perpendicular to the zigzag direction, (b) top view, (c) side view perpendicular to the armchair direction.

Composition	Lattice parameter (Å)		Band gap (eV)	
	Monolayer		Monolayer	Bulk
	a	*b*	GGA	GGA
SnSe	4.36 (4.41)	4.29 (4.17)	0.99 (1.00)	0.65 (0.69)
SnS	4.31 (4.26)	4.07 (4.06)	1.42 (1.52)	0.86 (0.91)
GeSe	4.41 (4.38)	3.99 (3.95)	1.16 (1.22)	0.83 (0.87)
GeS	4.48 (4.43)	3.70 (3.67)	1.71 (1.70)	1.18 (1.25)

Table 3.1: Calculated lattice parmeters and band gaps of SnSe, SnS, GeSe, and GeS. The values in the parentheses are from the Refs. [116, 138].

law to calculate electronic thermal conductivty from electrical conductivity.

To calculate the lattice thermal conductivity (κ_l), we used the ShengBTE code[133]. The second-order (harmonic) and the third-order (anharmonic) interatomic force constants (IFCs) are required to calculate lattice thermal conductivity. In order to calculate the second-order IFCs, we used the Phonopy code with a supercell of 5 × 5 × 1 and a *k*-mesh of 10 × 10 × 1. For the third-order IFCs, a supercell of 4 × 4 × 1 was used with the of interactions up to the 15^{th} nearest neighbors[134–136].

3.3 Results and discussions

3.3.1 Structure optimization and electronic structure

Bulk SnSe, SnS, GeSe, and GeS have an orthorhombic crystal structure with the space group *Pnma*(62), while their monolayer analogs have the space group $Pmn2_1$(31) (See Fig. 3.1). The structures are optimized with a large vacuum space of 15 Å in the z-direction until the forces on each atom become zero. The optimized lattice parameters are given in Table 3.1, and they are in good agreement with previous reports[137, 138].

Electronic structures are very important for understanding the thermoelectric behavior of materials. The band gaps of SnSe, SnS, GeSe, and GeS are calculated using the exchange-correlation functional within a generalized gradient approximation (GGA), as shown in Table 3.1. The GGA functional calculations show indirect band gaps for SnSe, SnS, and GeS and a direct band gap for GeSe, as shown in Fig. 3.2. Density of states (DOS) of the SnS and GeS monolayers has sharp peaks near conduction band minima and valence band maxima as shown in Fig. 3.2(b,d), which may enhance the Seebeck coefficient. All these monolayers have band gaps less than 2 eV, which suggests that they can be used as thermoelectric materials. It is very difficult to get the optimal value of the *ZT* for wide band gap materials because heavy doping is required.

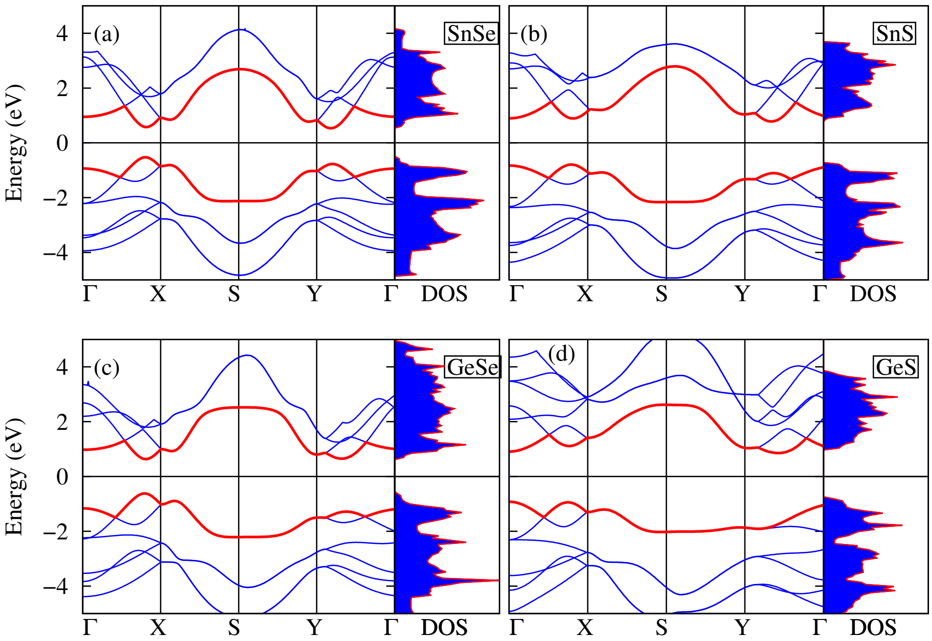

Figure 3.2: Band structures along the high-symmetry k-points Γ, X, S, and Y and density of states of (a) SnSe, (b) SnS, (c) GeSe, and (d) GeS

3.3.2 Carrier mobility and relaxation time

The carrier mobility (μ) of the group IV–VI monolayers is calculated in order to get relaxation time (τ). Our method to calculate the mobility is based on deformation potential theory used extensively to calculate carrier mobility andrelaxation time of two-dimensional materials[139–142], the expression to calculate the mobility is given by[139, 143]:

$$\mu = \frac{e\hbar^3 C^{2D}}{k_B T m^* m_d E_1^2} \tag{3.2}$$

where C_{2D} is the two-dimensional elastic constant determined by fitting the energy-strain curve to quadratic polynomial (see Fig. 3.3), our calculated values for C_{2D} are consistent with previous reported values[144]. T represents the temperature, m^* is the effective mass in the transport direction, and m_d is calculated as $m_d = \sqrt{m_x m_y}$. Here m_x and m_y are the effective masses along armchair and zigzag directions. E_1 is the deformation potential constant defined as: $E_1 = \frac{\partial E_{edge}}{\partial \delta}$, where E_{edge} is the conduction band minima (CBM) and δ is uniaxial strain. The shift in CBM by applying uniaxial strain is shown in Fig. 3.4. The relaxation time is evaluated from mobility using the following relation:

$$\tau = \frac{m^* \mu}{e} \tag{3.3}$$

The calculated E_1, C_{2d}, m^* and temperature-dependent μ and τ are tabulated in Table 3.2. We found an anisotropic behaviour in mobility and relaxation time for these monolayer. The carrier mobility of SnSe is in a good agreement with ref. [140]. The GeS has the highest carrier mobility and relaxation time along the armchair direction among these four monolayer due to the low deformation constant and the low effective mass.

3.3.3 Thermoelectric properties

Electrical and electronic thermal conductivities

The thermoelectric properties of SnSe, SnS, GeSe, and GeS are calculated using the Boltzmann transport equation for electrons under a constant scattering time. Boltztrap code calculates relaxation-time dependent electrical conductivity (σ/τ) and electronic thermal conductivity (κ_e/τ). Since there is no experimental data available for the electrical conductivity to calculate the exact value of the relaxation time of these monolayers, deformation potential theory is used to predict the temperature-dependent relaxation time for each material as compiled in Table 3.2. The electrical (σ) and electronic thermal (κ_e) conductivities are plotted as a function of carrier concentration (n) in Fig. 3.5(a–d) and (e–g) respectively, at 300 K, 500 K, and 700 K along armchair and zigzag directions. The carrier concentration shows the doping (positive values for *p*-type doping and negative values for *n*-type doping). The electrical and thermal conductivities increase by increasing carrier concentration. When the Fermi level occurs in the middle band gap region, the conductivities are increased slowly with respect to the carrier concentration and when it moves down into the valence band (for *p*-type) or moves up into conduction band (for *n*-type), the conductivities are increased quickly. GeSe has the highest electrical conductivity of 69.85×10^6 S/m at $n = -8.9\times10^{14}$ /cm 2 in the *n*-type doping among these compounds. The band gap is higher for the monolayer than bulk (see Table 3.1). The monolayers have lower electrical conductivity than the bulk due to the increase in the band gaps.

Seebeck coefficient

The Seebeck coefficients are calculated as a function of carrier concentration at different temperatures along the armchair and zigzag direction, as shown in Fig. 3.6. As the temperature decreases, the Seebeck coefficient also increases because of bipolar conduction[145]. The Seebeck coefficients of the two-dimensional monochalcogenides are two times greater than those of the bulk material as shown in the Table 3.3. This results from, the increase in the band gaps and the density of states near the Fermi level. The GeS has the largest Seebeck

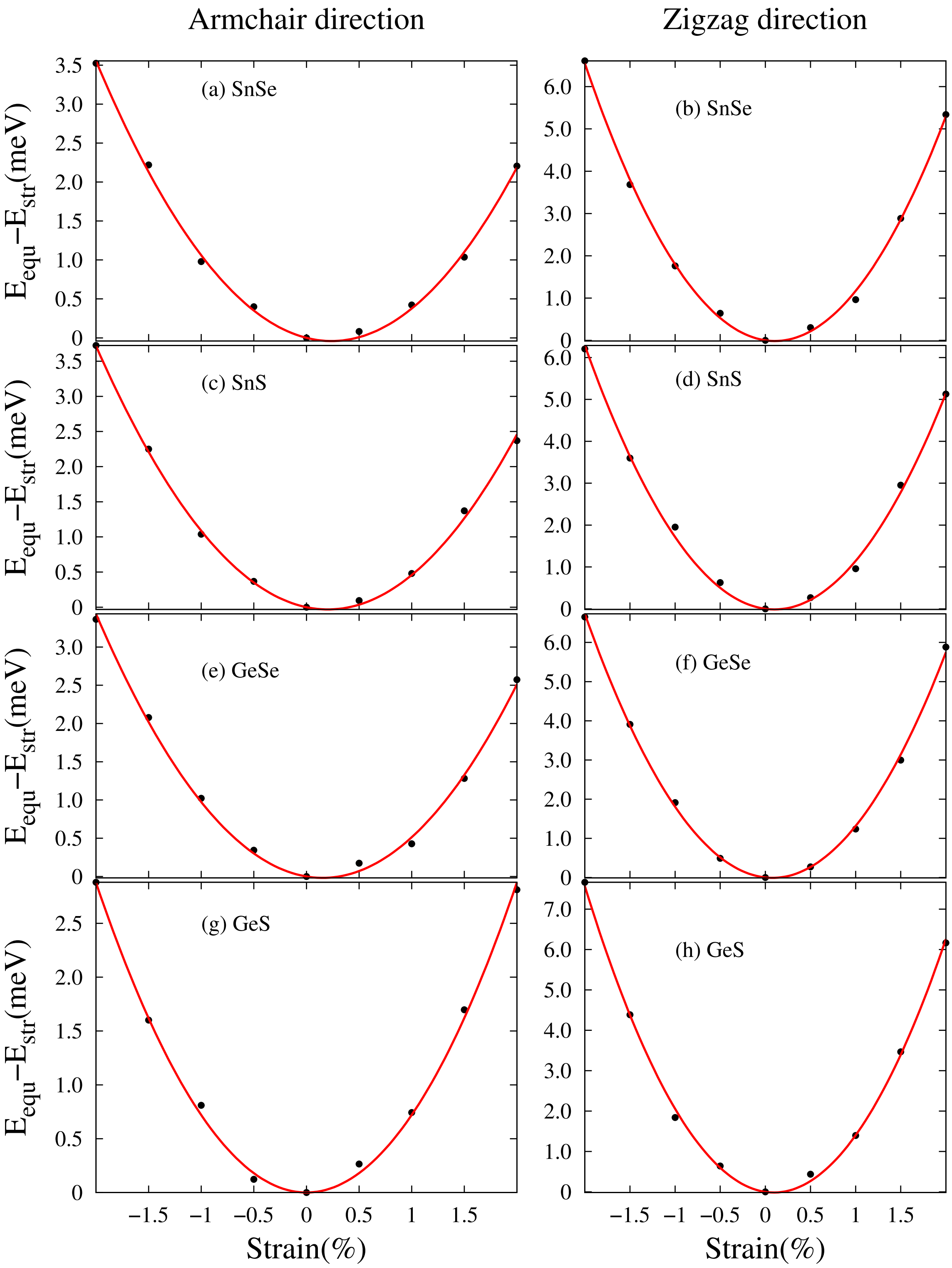

Figure 3.3: Elastic constants are calculated by fitting the energy difference ($E_{equ}-E_{str}$), where E_{equ} is the total energy in the equilibrium state and E_{str} is the total energy in the strained state, to quadratic polynomial functions for (a, b) SnSe, (c, d) SnS, (e, f) GeSe, and (g, h) GeS monolayers along armchair and zigzag directions.

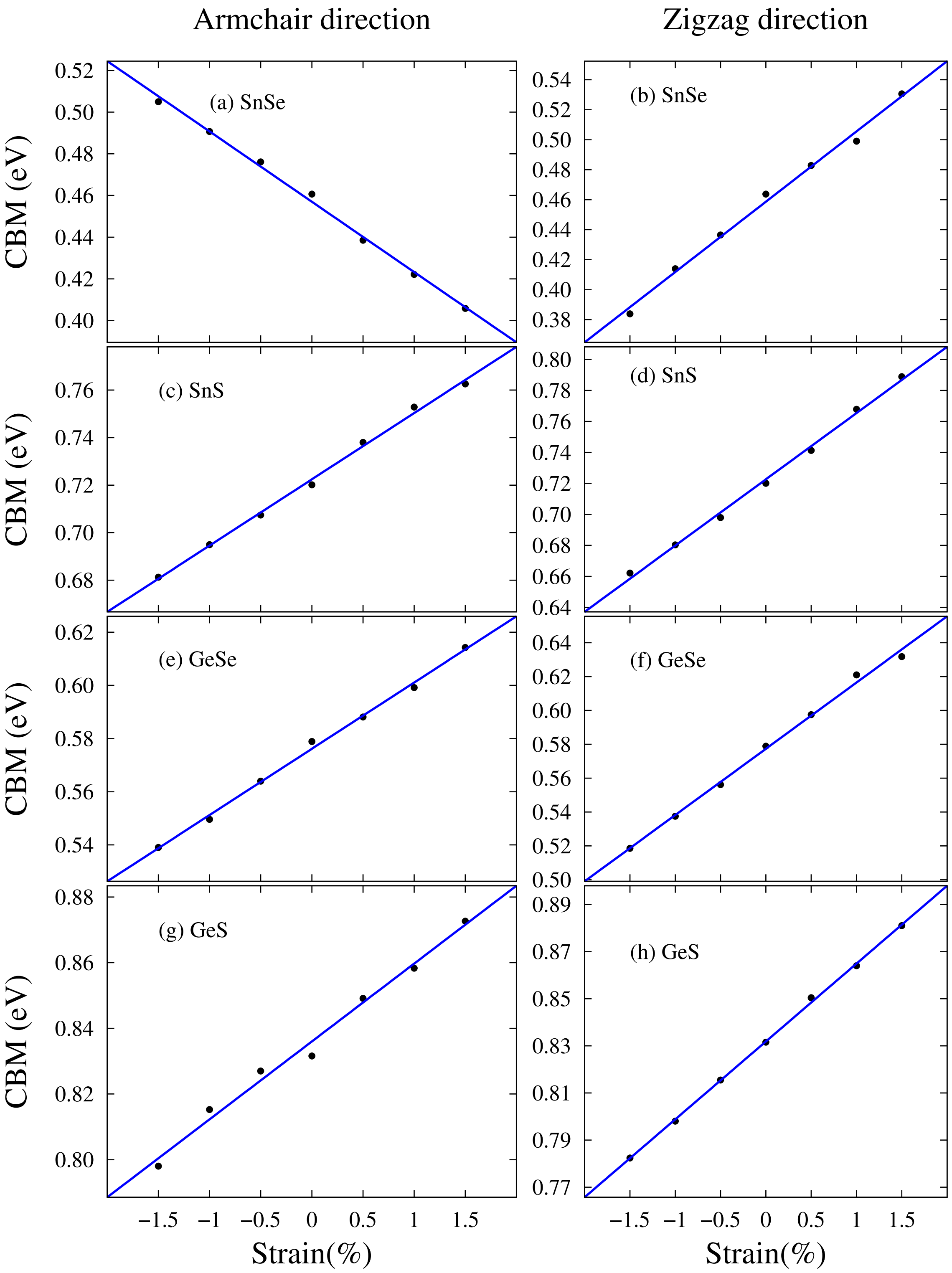

Figure 3.4: Calculated deformation constants for group IV–VI compounds: (a, b) SnSe, (c, d) SnS, (e, f) GeSe, and (g, h) GeS monolayers. The conduction band minima (CBM) at uniaxial strains are fitted to straight lines.

Composition		SnSe		SnS		GeSe		GeS	
Direction		Armchair	Zigzag	Armchair	Zigzag	Armchair	Zigzag	Armchair	Zigzag
	E_1(eV)	3.32	4.70	2.78	4.27	2.49	3.91	2.37	3.70
	C_{2D}(N/m)	12.46	24.82	14.08	26.05	12.11	28.35	13.89	33.40
	m^*(m_e)	0.15	0.16	0.24	0.28	0.27	0.30	0.19	0.37
T=300 K	μ ($\mathrm{cm}^2\mathrm{V}^{-1}\mathrm{s}^{-1}$)	1035.84	965.23	623.54	419.10	541.24	465.01	1045.40	529.57
	τ (fs)	88.35	87.82	85.10	66.73	83.10	79.33	112.95	111.43
T=500 K	μ ($\mathrm{cm}^2\mathrm{V}^{-1}\mathrm{s}^{-1}$)	621.50	579.13	374.13	251.48	324.74	279.01	627.24	317.73
	τ (fs)	53.01	52.69	51.06	40.04	49.86	47.59	67.77	66.86
T=700 K	μ ($\mathrm{cm}^2\mathrm{V}^{-1}\mathrm{s}^{-1}$)	443.93	413.60	267.23	179.63	231.96	199.29	448.03	226.95
	τ (fs)	37.86	37.63	36.47	28.60	35.61	33.99	48.40	47.75

Table 3.2: Deformation potential constant (E_1), two dimensional elastic constant (C_{2D}), effective mass (m^*), carrier mobility (μ) and relaxation time (τ) at 300 K, 500 K, and 700 K, in the armchair and zigzag directions of the group IV–VI compounds.

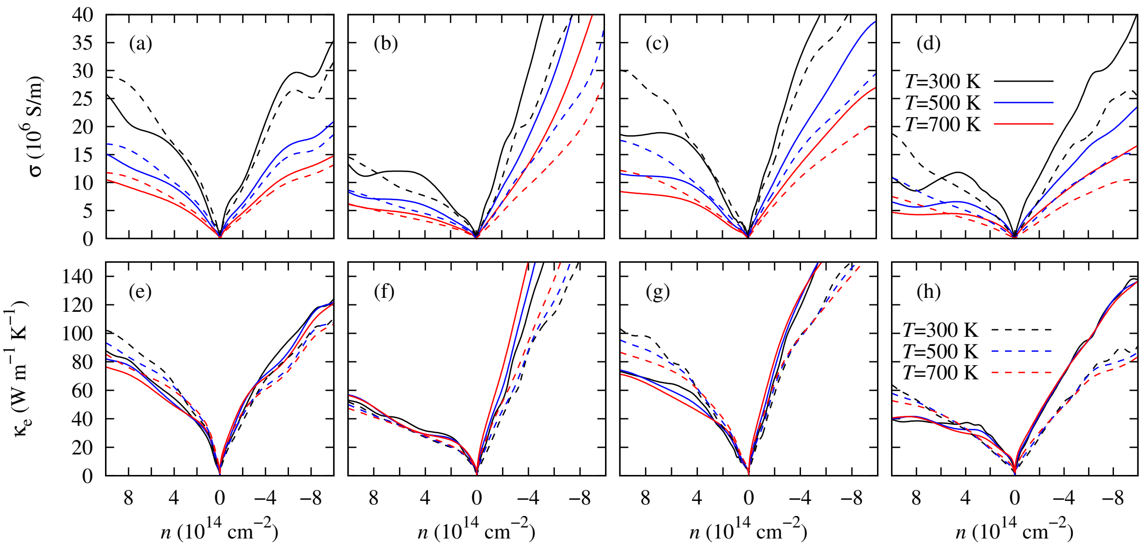

Figure 3.5: Electrical (σ) and electronic thermal (κ_e) conductivities for the (a,e) SnSe, (b,f) SnS, (c,g) GeSe, and (d,h) GeS along the armchair (solid lines) and zigzag (dashed lines) directions at 300 K, 500 K, and 700 K.

coefficient of 2810 μVK^{-1} at 300 K because of the large band gap and the flatness in the band structure. The Seebeck coefficient (S) is calculated with the expression,

$$S = \frac{\int_{-\infty}^{\infty} dE\, g(E)\,(E-\mu)\left(-\frac{\partial f(E,\mu,T)}{\partial E}\right)}{T\int_{-\infty}^{\infty} dE\, g(E)\left(\frac{\partial f(E,\mu,T)}{\partial E}\right)} \tag{3.4}$$

where E, $g(E)$, $f(E,\mu,T)$, μ, and T are the energy, the transport function, the Fermi function, the chemical potential, and temperature, respectively[146]. The transport funtion is

$$g(E) = N(E)v^2(E)\tau(E) \tag{3.5}$$

where $N(E)$ is the density of states, $v(E)$ is Fermi velocity and $\tau(E)$ is scattering time[146]. The Seebeck coefficient changes dramatically near the Fermi level because of the term $\frac{\partial f}{\partial E}$ in Eq. 3.4 which behaves like a Dirac delta function.

Composition	SnSe	SnS	GeSe	GeS
Bulk[116]	990	1260	1240	2000
Monolayer	1750	2380	1960	2810

Table 3.3: The largest values of Seebeck coefficients (S) of bulk and monolayer SnSe, SnS, GeSe and GeSe at 300 K (unit: μVK^{-1})

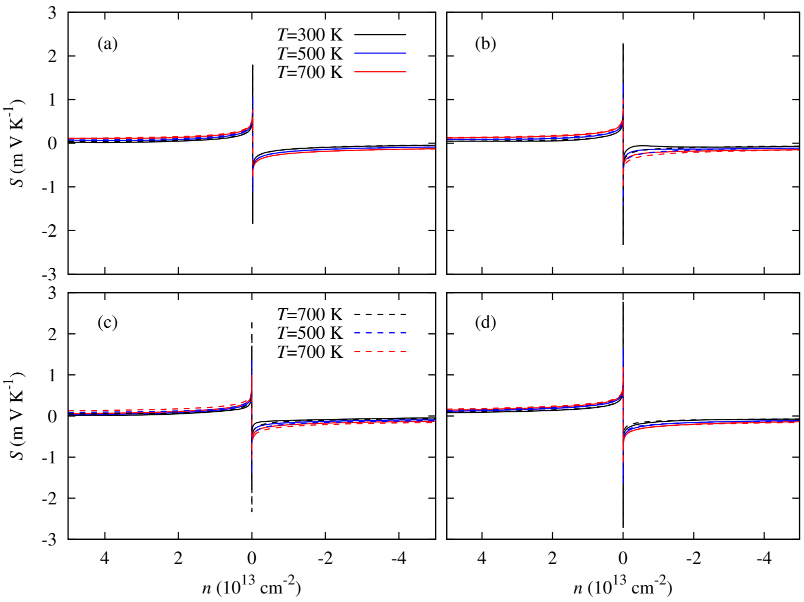

Figure 3.6: Calculated Seebeck coefficients (S) as a function of the carrier concentration (n) along the armchair (solid lines) and zigzag (dashed lines) directions at 300 K, 500 K, and 700 K for the group IV–VI monolayers (a) SnSe, (b) SnS, (c) GeSe, and (d) GeS.

Phonon dispersion and lattice thermal conductivity

Phonon dispersions of SnSe, GeSe, SnS, and GeS were computed to examine the thermal stability using density functional perturbation theory[147], as shown in Fig. 3.7. There is no imaginary line in the dispersion curves, which means that these materials are vibrationally stable. There are twelve modes of vibrations: three lower modes that are acoustic (a transverse acoustic mode, a longitudinal acoustic mode, and a flexural acoustic mode), and the others are optical modes. The flexural acoustic mode is an out-of-plane transverse acoustic mode similar to other two-dimensional materials like graphene, phosphorene, and stanene, quadratic near Γ point[148–150]. The flexural mode vibrational direction is exactly perpendicular to the plane. It is an important mode in order to understand thermal and mechanical properties of two-dimensional materials.

The lattice conductivities are calculated by solving the Boltzmann transport equation for phonons (BTEP) using the iterative method and the relaxation time approximation (RTA). The iterative method exactly solves the BTEP, while RTA is a good approximation for low conductivity compounds. The results in Fig. 3.8 show good agreement with recently reported results[126]. All four of the materials have very low lattice thermal conductivity compared to other two-dimensional materials like graphene, phosphorene, and monolayer of $MoSe_2$, and

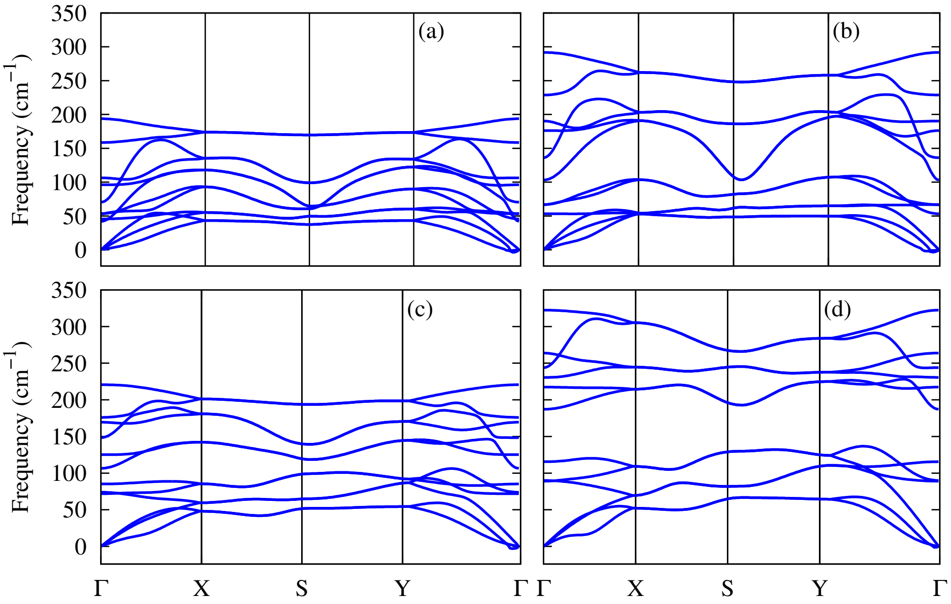

Figure 3.7: Phonon dispersions along high symmetry *k*-points for (a) SnSe, (b) SnS, (c) GeSe, and GeS

WSe$_2$, and are comparable to the monolayer bismuth as shown in Table.3.4[121, 148, 149, 151]. We also found the different lattice thermal conductivity along the armchair and zigzag directions. Because of the heavy masses of Sn and Se, SnSe has the lowest lattice conductivity of 2.44 Wm^{-1}K^{-1} and 2.63 Wm^{-1}K^{-1} at room temperature along the armchair and zigzag directions, respectively.

According to glass dynamical theory, the lattice thermal conductivity is calculated as$\kappa_l = 1/3C_v l v_s$, where C_v is the heat capacity, l is the mean free path, and v_s is the sound velocity. As the temperature increases, the lattice softens and the stiffness decreases, which reduces the sound velocity and hence the lattice thermal conductivity[152]. This trend is shown in Fig. 3.8.

Figure of merit (*ZT*)

Finally, using the Seebeck coefficient and the electrical and thermal conductivities, we calculated *ZT* as a function of the carrier concentration along the armchair and zigzag directions at 300 K, 500 K, and 700 K, as shown in Fig. 3.9. These monolayers had very high *ZT*. SnSe had the highest *ZT* of 2.63 along the armchair direction at 700 K because of the high electrical conductivity and Seebeck coefficient and the low lattice thermal conductivity. In the case SnS, a high *ZT* of 1.88 is predicted along the zigzag direction.

Compound	κ_l (Wm^{-1}K^{-1})		
	Monolayer		Bulk
	zigzag	armchair	
Graphene	2200[148]	2200[148]	2000[153]
Phoshorene	30.1[149]	13.6[149]	-
Bi monolayer	3.8[121]	3.8[121]	-
MoSe2	70[151]	70[151]	40[151]
WSe2	42[151]	42[151]	35[151]
SnSe	2.6	2.4	0.32[116]
SnS	4.7	4.4	0.45[116]
GeSe	6.7	5.2	0.39[116]
GeS	10.5	7.8	0.52[116]

Table 3.4: Comparison of lattice thermal conductivities κ_l of group IV-VI monolayers with other two-dimensional materials at room temperature

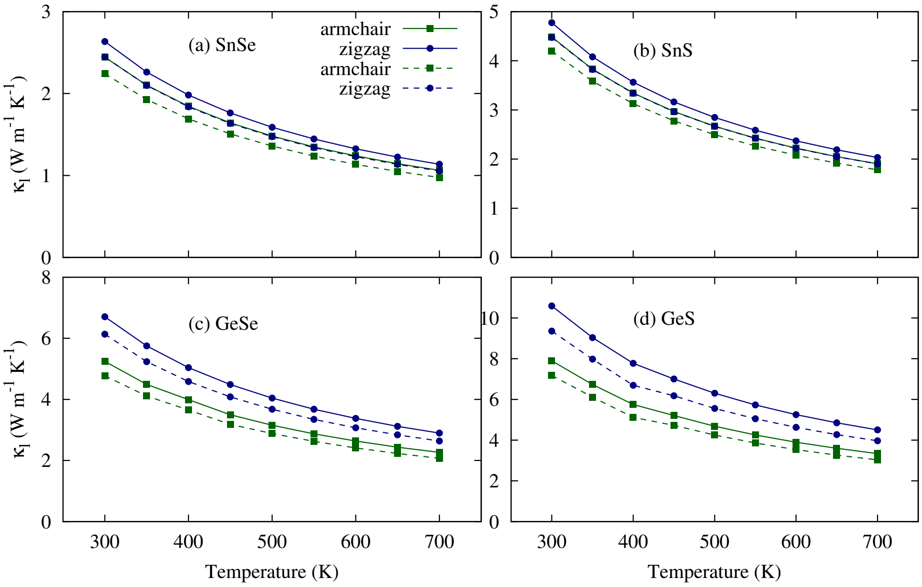

Figure 3.8: Lattice thermal conductivity (κ_l) for the group IV–VI monolayers are calculated as a function of the temperature using iterative (solid lines) and SMRTA (dashed lines) method.

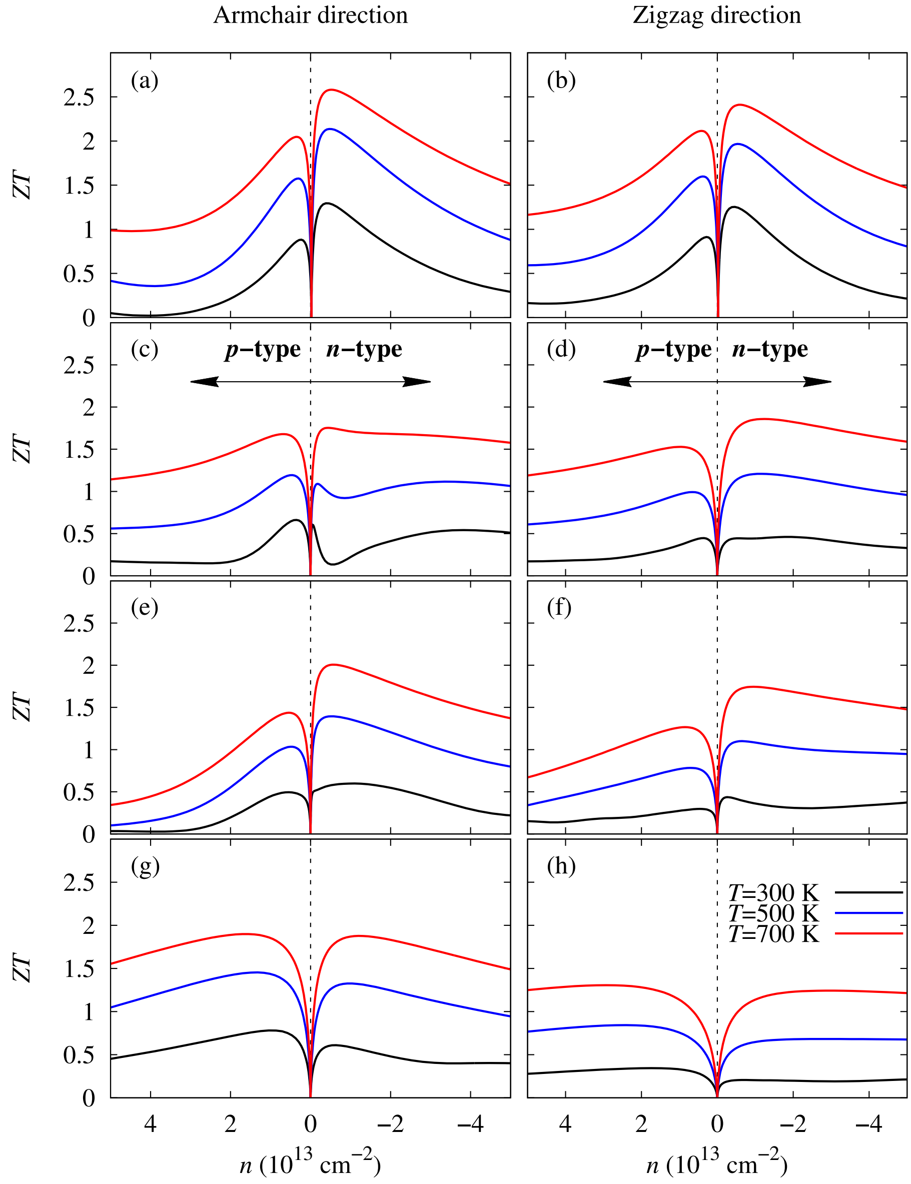

Figure 3.9: Calculated Figures of merit (ZT) as a function of the carrier concentration (n) for the monolayer of (a,b) SnSe, (c,d) SnS, (e,f) GeSe, and (g,h) GeS along armchair and zigzag directions at temperature 300 K, 500 K, and 700 K.

3.4 Summary

We analyzed the structural, electronic, thermoelectric, and phonon-transport properties of the two-dimensional monochalcogenide compounds SnSe, SnS, GeSe, and GeS using density functional theory combined with Boltzmann transport theory for electrons and phonons. These compounds are energetically and vibrationally stable, and SnSe, SnS, and GeS have indirect band gaps while GeSe has a direct band gap. The Seebeck coefficients of these two-dimensional materials are two times larger than those of their bulk structures, and two-dimensional GeS has the largest Seebeck coefficient of 2810 μVK^{-1} at room temperature. These monolayer materials have very low lattice thermal conductivities in comparison to other two-dimensional materials. *ZT* of SnSe, GeSe and GeS along the armchair direction was 2.63, 1.99, and 1.85, respectively, while that of *ZT* of SnS along the zigzag direction was 1.88. These *ZT* values are higher than those of their bulk analogs. Hence, the materials are very promising for thermoelectric applications.

Chapter 4

Ultra low lattice thermal conductivity and high carrier mobility of monolayer SnX_2

4.1 Introduction

After the exploration of graphene, the search of new two-dimensional materials started both for fundamental research and device applications in the field of optoelectronics and energy conversion and storage [147, 154–156]. Monolayer MoS_2-like transition metal dichalcogenides have gained a tremendous interest due to their variety in band gaps, mechanical and chemical properties, and applications in thin film solar cells, metal ion batteries, and thermoelectric devices[35, 157–161]. Thermoelectric materials convert the waste heat energy directly into the useful electrical energy.

One of the crucial problems in the thermoelectric materials is the high lattice thermal conductivity which decreases the ZT. Materials having low lattice thermal conductivity are more significant in thermoelectrics. Since the electronic thermal conductivity has a direct dependence on the electrical conductivity, reducing the electronic thermal conductivity by reducing the electrical conductivity is not an effective way. According to Slack's theory of nonmetallic crystals, the requirements for low lattice thermal conductivity are strong anharmonicity (large Grüneisen parameters), weak interatomic bonding interactions, structural complexity, and materials containing heavy elements[29]. For example, because of the high lattice thermal conductivity (2200 W/mK) of graphene, its use in thermoelectric devices is not attractive[148]. On the other hand, several two-dimensional materials like stanene, silicene, phosphorene, MoS_2, $MoSe_2$, WSe_2, SnSe, and Bi have been reported for low lattice thermal conductivities at room temperature[21, 36, 126, 149, 150, 162–164].

In semiconductor devices, the carrier mobility by holes and electrons plays an important role. The lattice thermal conductivity can be reduced by producing vacancies or doping heavy elements, but they decrease the carrier mobility as well. However, high carrier mobility coupled with low lattice thermal conductivity is required for efficient thermoelectric materials. Graphene, phosphorene, silicene, and monolayer MoS_2, TiS_3, SnSe, GeS, PbS, and PbSe have been reported to have high carrier mobility[139, 140, 165–167]. Monolayer SnX_2 (X = S, Se) have been recently synthesized and their structural parameters and electronic band structures are well studied[168]. Several recent reports show that the bulk SnX_2 has very low lattice thermal conductivity[169, 170], but the lack of researches about the lattice thermal conductivity and carrier mobility for their monolayer phases motivates us to study them. Since these monolayers contain heavy elements such as Sn and Se with weak interatomic bondings, it is expected of these materials to have low lattice thermal conductivity.

This paper explores the phonon transport properties such as phonon dispersion, phonon group velocities, Grüneisen parameters, lattice thermal conductivities, and phonon-limited carrier mobilities of the monolayer SnX_2, using the PBTE and deformation potential theory. It is found that the lattice thermal conductivity of monolayer $SnSe_2$ at room temperature is as low as 3.82 W/mK, which is attributed to the heavy atomic masses of Sn and Se and its strong phonon anharmonicity. The calculated lattice thermal conductivities are lower than in-plane lattice thermal conductivity of their bulk phases unlike MoS_2 and $MoSe_2$[151, 171]. The carrier mobility of the monolayer SnS_2 at room temperature is as high as 756.60 $cm^2V^{-1}s^{-1}$ for electrons and 187.44 $cm^2V^{-1}s^{-1}$ for holes. Contribution of each mode in lattice thermal conductivity is evaluated; longitudinal acoustic (LA) mode is found as the main contributor in the monolayer SnS_2 while transverse acoustic (TA) mode in the monolayer $SnSe_2$. The size effects on lattice thermal conductivity are also discussed. Owing to their ultra low lattice thermal conductivity and high carrier mobility, monolayer SnS_2 and $SnSe_2$ are promising for thermoelectric applications.

4.2 Computational method

All density functional theory calculations are performed by adopting VASP[129] with the projector augmented wave method[101]. The generalized gradient approximation in the form of Perdew-Burke-Ernzerhof[93] is used as an exchange correlation functional. The kinetic energy cutoff is set to 500 eV. The Monkhorst-Pack k-mesh of $15\times15\times1$ is used and the structure is optimized until the largest Hellmann-Feynman force component on each atom is less than 0.001 eV/Å. The Heyd–Scuseria–Ernzerhof hybrid functional is used to calculate the band structure and carrier mobility. Phonopy code is used to calculate the phonon spectra, phonon group velocities, Grüneisen parameters, and harmonic force constants with a supercell

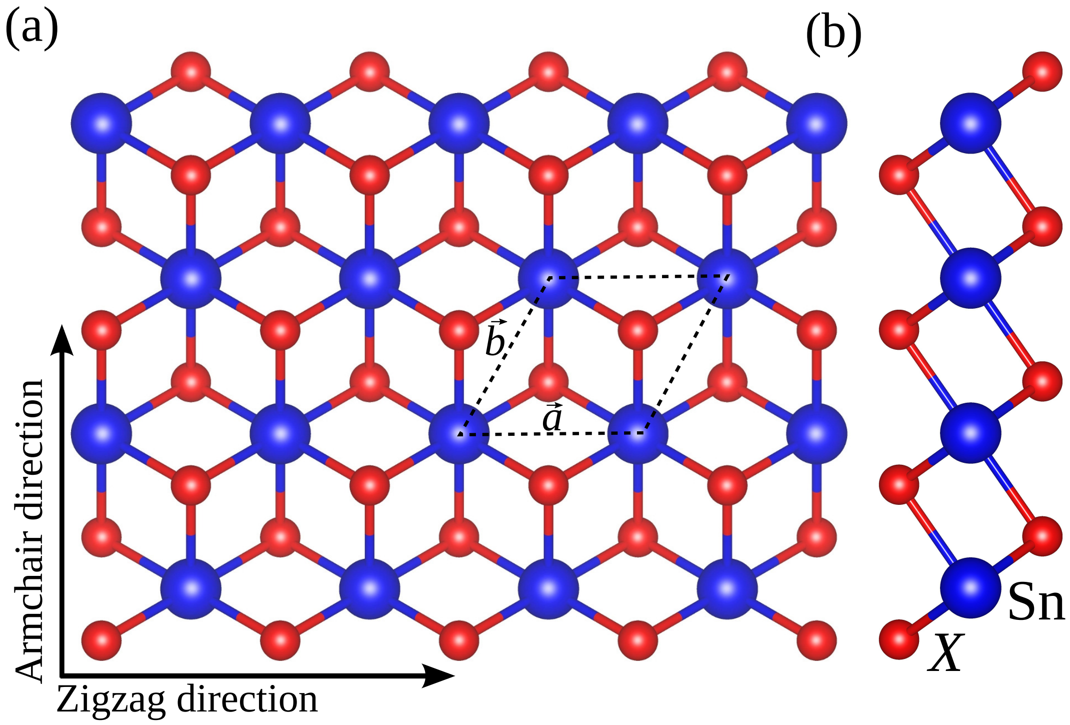

Figure 4.1: (a) Top and (b) side views of the monolayer SnX_2 (X = S, Se). The dashed lines show the primitive unit cell (with lattice vectors $\vec{a}$ and $\vec{b}$).

of 6×6×1 using the finite displacement method[134, 147]. Lattice thermal conductivity is calculated by solving the Boltzmann transport equation for phonons as implemented in the ShengBTE code[133, 135]. The anharmonic force constants are obtained using a supercell of 5×5×1 including five nearest neighbors.

4.3 Results and discussions

4.3.1 Structure optimization and phonon spectra

The energetically and dynamically stable 1T phase of monolayer tin dichalcogenides (SnX_2) lies in the $P\bar{3}m1$ space group (No. 164) as shown in Fig. 4.1. The optimized lattice parameters of a hexagonal primitive unit cell are a=b=3.69 Å for monolayer SnS_2 and a=b=3.86 Å for monolayer $SnSe_2$. The lattice parameters are in good agreement with the previously reported values[172, 173]. Monolayer SnX can be derived from the distorted tetrahedra of Sn(II) atoms with a lone pair. In this monolayer three Sn–X bonds form with two different bond lengths. However, monolayer SnX_2 is derived from the octahe- dral coordination of Sn(IV) to form a hexagonal structure.

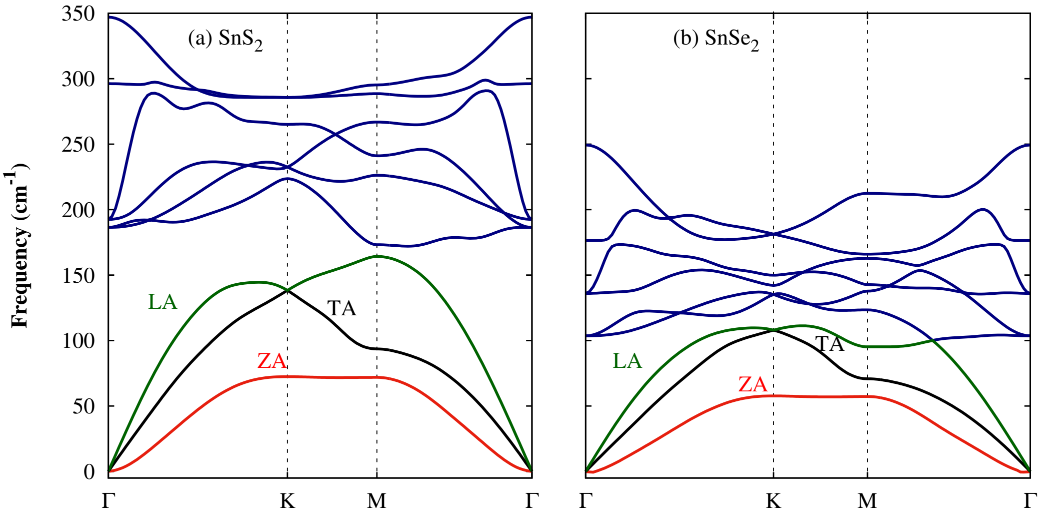

Figure 4.2: Phonon band structure of (a) monolayer SnS$_2$ and (b) monolayer SnSe$_2$. The red, black, green, and blue lines represent the ZA , TA, LA, and the optical modes, respectively.

The phonon spectra of the monolayers SnX_2 are shown in Fig. 4.2. The absence of imaginary frequencies in the phonon band structure for monolayer SnX_2 guarantees its dynamical stability. Among the total nine vibrational modes for the three atoms in a primitive unit cell, the lowest three modes are acoustic (LA, TA, and ZA (flexural acoustic mode)) modes and the other six modes with relatively high frequencies are optical ones. The maximum frequency of vibration is 347.85 cm^{-1} for monolayer SnS$_2$ and 249.36 cm^{-1} for monolayer SnSe$_2$. The phonon band gap between acoustic and optical modes for monolayer SnS$_2$ is larger than that for monolayer SnSe$_2$ because of the higher mass ratio of Sn to S than Sn to Se. The LA and TA modes are linear and the ZA mode is nearly quadratic at the gamma point. The phonon spectra of these monolayers are very similar, but the frequencies of monolayer SnSe$_2$ are slightly shifted downward compared to that of monolayer SnS$_2$ because of its larger reduced mass. Monolayer SnX_2 has higher phonon frequencies than monolayer SnX due to the difference in the oxidation state of Sn in both these cases, as reported in ref. [126]. The optical bands in phonon dispersion of the monolayer SnX are dispersive, which significantly increases the contribution of these branches to the lattice thermal conductivity (see Table 4.1).

4.3.2 Phonon group velocities, Grüneisen parameters, and Debye temperatures

In order to understand the lattice thermal conductivity of the monolayer SnX_2, we explore the phonon related properties such as phonon spectra, phonon group velocity, Grüneisen pa-

System	ZA (%)	TA (%)	LA (%)	Optical (%)	κ_l(Wm^{-1}K^{-1})	Θ_D (K)
SnS_2	36.26	25.56	33.89	4.29	6.41	136.9
$SnSe_2$	29.85	32.32	29.53	8.30	3.82	107.8
SnS	27.07[126]	19.79[126]	25.97[126]	27.17[126]	3.21[126]	——
SnSe	31.39[126]	25.16[126]	14.90[126]	28.55[126]	2.95[126]	——
MoS_2	29.1[160]	30.4[160]	39.1[160]	1.4[160]	101[160]	262.3[35]
Graphene	76[16]	15[16]	8[16]	1[16]	3288[16]	2300[174]
Stanene	13.5[150]	26.9[150]	57.5[150]	2.1[150]	11.6[150]	72.5[150]
Silicene	38.98[21]	21.63[21]	20.97[21]	18.42[21]	27.72[21]	798.1[21]

Table 4.1: The percentage contribution of acoustic modes (ZA, TA, LA) and optical modes toward the lattice thermal conductivity at room temperature, and the Debye temperature

rameter and the Debye temperature. Phonon group velocities are computed from the phonon spectra along the Γ-M and Γ-K directions, as shown in Fig. 4.3. The phonon group velocity of each mode is given by: $v_k = \frac{\partial \omega_k(\mathbf{q})}{\partial \mathbf{q}}$, where ω, k and, q represent the vibrational frequency, the vibrational mode index, and the wave vector respectively. The phonon group velocities of monolayer SnS_2 at low frequency limit are 1948 m/s in the ZA mode, 3222 m/s in the TA mode, and 5160 m/s in the LA mode. For monolayer $SnSe_2$ the group velocities are 1604 m/s in the ZA mode, 2514 m/s in the TA mode, and 4044 m/s in the LA mode. The phonon group velocity of monolayer SnX_2 in the LA mode is smaller than those of graphene[175] (22000 m/s), phosphorene[176] (8640 m/s), and silicene[21] (9520 m/s), and larger than stanene[150] (3600 m/s) and monolayer MoS_2[163] (1108 m/s).

The Grüneisen parameter γ is calculated for each phonon mode in order to quantify the anharmonicity of monolayer SnX_2 as plotted in Fig. 4.4. The Grüneisen parameters are evaluated using the definition[177]:

$$\gamma_k(q) = -\frac{a_0}{\omega_k(q)} \frac{\partial \omega_k(q)}{\partial a}$$

where a_0 is the equilibrium lattice constant. Very large absolute values of the Grüneisen parameter are found at long wavelength limit, which shows large phonon anharmonicity of monolayer SnX_2. The Slack's equation for lattice thermal conductivity[29] is:

$$\kappa_l = \frac{A\bar{M}\Theta_{\mathrm{D}}\delta^{\frac{1}{3}}N^{\frac{1}{3}}}{\gamma^2 T}$$

where A is a constant and $\bar{M}$, Θ_{D}, δ, N, γ, and T are average atomic mass, Debye temperature, volume per atom, number of atoms per unit cell, Grüneisen parameter, and temperature, respectively. Therefore, strong anharmonicity (or large Grüneisen parameter) is required for low

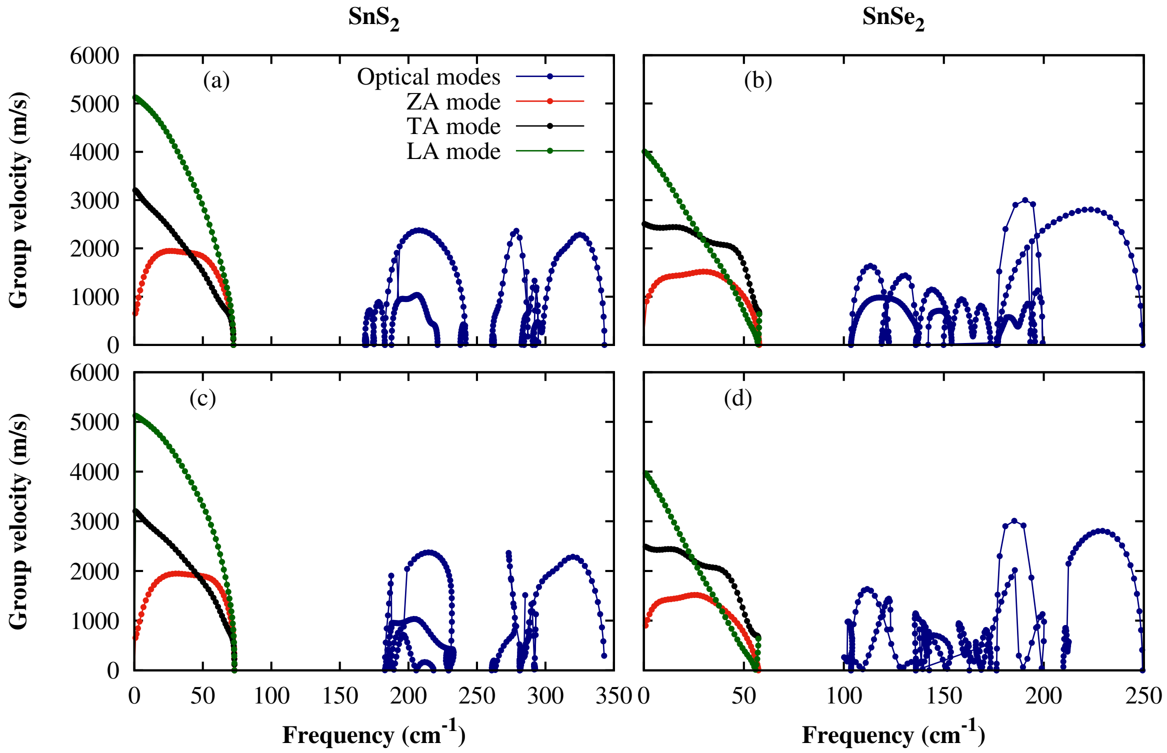

Figure 4.3: Phonon group velocities along (a) Γ-K, (c) Γ-M directions for monolayer SnS_2 and along (b) Γ-K, (d) Γ-M directions for monolayer $SnSe_2$

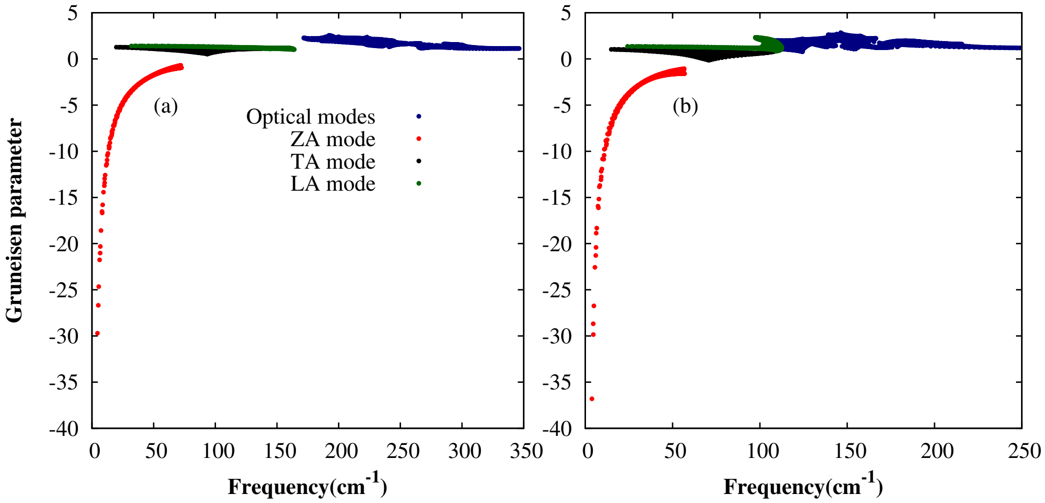

Figure 4.4: Mode-dependent Grüneisen parameters of (a) monolayer SnS_2 and (b) monolayer $SnSe_2$

lattice thermal conductivity. Low Grüneisen parameter is reported for germanene, stanene, and silicene, and high for monolayer WS_2, MoS_2, and $MoSe_2$[35, 175].

Finally we calculate the Debye temperature (Θ_D) that is defined as[178]:

$$\frac{1}{\Theta_\mathrm{D}^3} = \frac{1}{3}\left(\frac{1}{\Theta_\mathrm{ZA}^3} + \frac{1}{\Theta_\mathrm{TA}^3} + \frac{1}{\Theta_\mathrm{LA}^3}\right)$$

where $\Theta_i = \hbar\omega_i^\mathrm{max}/k_B$ is the Debye temperature for each mode (i = ZA, TA, LA) and ω_i^max is the maximum frequency of the ith mode. The Debye temperatures for $\mathrm{Sn}X_2$ are listed in Table 4.1, which are smaller than those of graphene, silicene, monolayer MoS_2 and larger than that of stanene[150, 160, 175]. Small Debye temperatures for SnS_2 and $SnSe_2$ mean that many phonon modes are activated at room temperature, which leads to increasing phonon population and phonon scattering rate[179] to reduce the lattice thermal conductivity.

4.3.3 Lattice thermal conductivity

Lattice thermal conductivity is calculated using both the iterative and single mode relaxation time approximation (SMRTA) methods, as shown in Fig. 4.5. We find very low lattice thermal conductivity for monolayer SnS_2 (6.41 W/mK for the iterative method and 5.44 W/mK for the SMRTA method) and $SnSe_2$ (3.82 W/mK for the iterative method and 3.23 W/mK for the SMRTA method) at room temperature. The difference in the lattice thermal conductivity between the two methods for SnS_2 is larger than $SnSe_2$ because the SMRTA method is usually a good approximation for low thermal conducting materials. In the SMTRA method, the

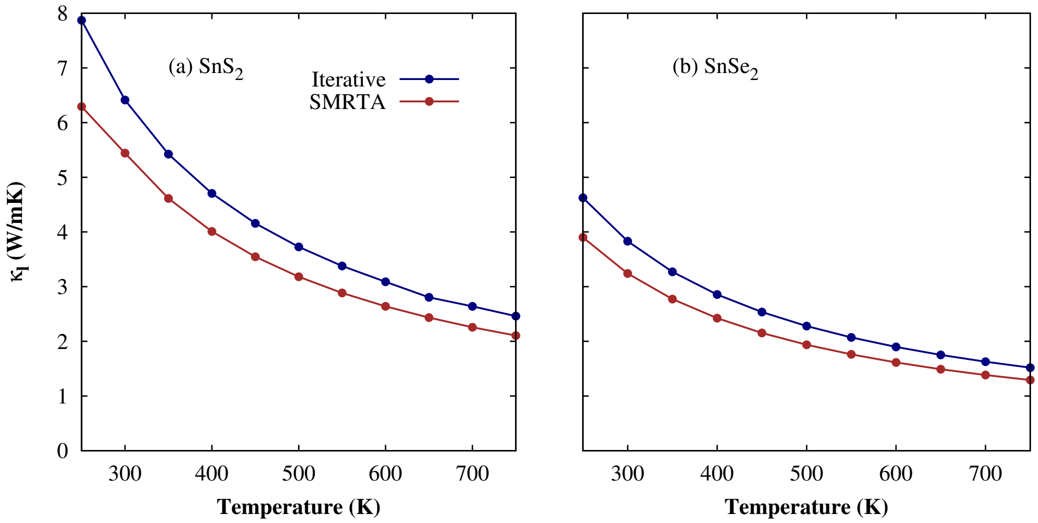

Figure 4.5: Lattice thermal conductivities as a function of temperature for the monolayer (a) SnS_2 and (b) $SnSe_2$

individual phonon mode is excited and has no memory of the initial phonon distribution. This approach only works when normal processes are dominated over the Umklapp processes. It is not a good approximation for high thermal conducting materials such as graphene or GaN. The iterative method solves the Boltzmann transport equation exactly and gives a fully converged value of the lattice thermal conductivity. It is equally applicable for high and low lattice thermal conducting materials[180]. Low lattice thermal conductivities of the monolayer SnX_2 are due to their low phonon velocities, strong anharmonicity, and low Debye temperatures as compared to other two-dimensional materials.

Contributions of acoustic and optical modes to the lattice thermal conductivity are tabulated in the Table 4.1. The contributions from the ZA mode of SnX_2 are smaller than that of graphene, because graphene has the reflection symmetry which does not allow the ZA-mode anharmonic phonons to scatter. Approximately 60% contribution to the lattice thermal conductivity of monolayer SnX_2 comes from the TA and LA modes (unlike graphene) because of the strong anharmonic interactions. The contribution of SnX_2 is compared with well-known two-dimensional materials in Table 4.1.

The cumulative lattice thermal conductivity as a function of phonon mean free path (MFP, Λ) is plotted in Fig. 4.6. The cumulative lattice thermal conductivity shows the dependence of lattice thermal conductivity on the size of the sample and the lattice thermal conductivity reaches its saturation value when the size of the sample is equal to or larger than the for maximal phonon MFPs (Λ_{max}). It also gives information regarding which phonon (long MFP or short MFP) contributes more to the lattice thermal conductivity. It is a very useful prop-

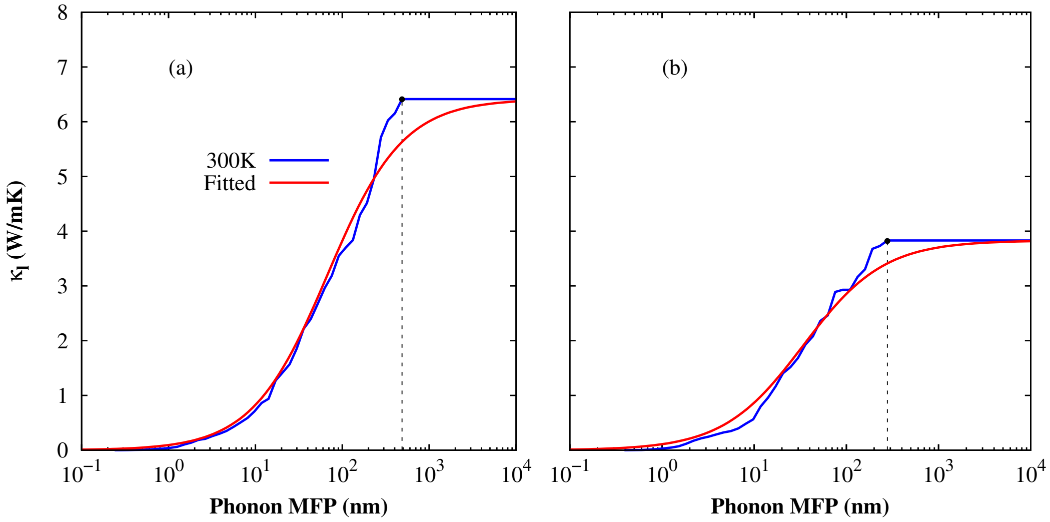

Figure 4.6: The cumulative lattice thermal conductivity as a function of phonon MFP for (a) monolayer SnS_2 and (b) monolayer $SnSe_2$ at room temperature

erty in order to get information about how nanostructuring can decrease the lattice thermal conductivity[15, 181, 182]. Λ for monolayer SnS_2 is 486.2 nm and 278 nm for monolayer $SnSe_2$. The values of $\Lambda_{\max}$ of SnS_2 and $SnSe_2$ are very large, which means that nanostructuring can be effectively modulated by the lattice thermal conductivity. In order to find an important parameter for designing nanostructuring, called the representative phonon MFP (Λ_0), the data is fitted to a single parametric function[133, 149]:

$$\kappa_l(\Lambda \leq \Lambda_{\max}) = \frac{\kappa_{\max}}{1+\Lambda_0/\Lambda},$$

where $\kappa_{\max}$ is the maximal lattice thermal conductivity. The values of Λ_0 for monolayers SnS_2 and $SnSe_2$ are 67.7 nm and 34.1 nm, respectively.

4.3.4 Carrier mobility

Since Bardeen and Shockley proposed deformation potential theory to evaluate the carriers mobility[143], deformation potential theory has been extensively used to calculate the mobility of two-dimensional materials[183–186]. In this theory, the mobility of single layer material $\mu_{2\mathrm{D}}$ is defined as

$$\mu_{2D} = \frac{e\hbar^3 C^{2\mathrm{D}}}{k_B T m^* m_d E_1^2}$$

where T is temperature, $m^* = \hbar^2(\frac{d^2E}{dk^2})$ is the effective mass obtained from the curvature of the band at the band edge whereas curvature $(\frac{d^2E}{dk^2})$ is calculated by least squares fit to a quadratic function,, and $m_d = \sqrt{m^*_{\Gamma-\mathrm{M}} m^*_{\mathrm{M-K}}}$ is the average effective mass. C^{2D} is the elastic constant defined by $C^{\mathrm{2D}} = [\partial^2 E/\partial\delta^2]/A_0$, where E is the total energy after applying uniaxial strain $(\delta = \Delta l/l_0)$ and A_0 is the area at equilibrium. The deformation potential constant E_1 is defined as: $E_1 = \Delta V/\delta$, where ΔV represents the shift in band edge (conduction band minima or valence band maxima) by applying uniaxial strain δ.

The calculated electronic band structures for the monolayer SnS_2 and $SnSe_2$ are shown in Figs. 4.7(a and b) with indirect band gaps of 2.38 and 1.39 eV, respectively. Band structure and carrier mobility calculations are based on the HSE06 method, a more accurate but computationally more expensive method. In both the monolayers, the conduction band maxima (CBM) are located at the M point and the valence band minima (VBM) are located between the Γ and M points. The VBM and CBM positions with respect to uniaxial strain are plotted in Figs. 4.7(c and d). The deformation potential constants are obtained by linear fitting of the CBM (for electrons) or VBM (for holes) *versus* the strain curve as listed in Table 4.2. The effective masses of an electron and a hole listed in Table 4.2 are calculated by fitting the bands near CBM and VBM to quadratic functions. Our effective mass values are consistent with previously reported ones[187]. The effective masses of the holes in the monolayer SnX_2 are heavier than those of electron due to the flatness of valence band. The small effective masses of electron indicate that the electron mobility would be high. The elastic constants (C^{2D}) are calculated directly from the strain–stress relationship and the calculated values of C^{2D} for monolayer SnS_2 and $SnSe_2$ are 66.86 N/m and 56.32 N/m, respectively, and they are consistent with previous studies[159, 188]. The monolayer SnS_2 has higher elastic constants compared to monolayer $SnSe_2$ due to the stronger Sn-S bond than Sn-Se.

The electronic properties of the monolayer SnX_2 are driven by carrier mobilities and strongly held by their effective masses. The carrier mobilities are determined by applying standard two-dimensional model, the so-called acoustic phonon-limited mobility model in which acoustic phonon scattering is the fundamental process[139, 140, 185]. The carrier mobility and relaxation time ($\tau = \mu m^*/e$) for the electrons and holes of monolayer SnX_2 are computed on the basis of the calculated effective mass, elastic constant, and deformation potential constant as listed in Table 4.2. Predicted carrier mobilities of electron and hole are highly asymmetric: a high mobility of 756.60 $\mathrm{cm^2V^{-1}s^{-1}}$ for electrons and 187.44 $\mathrm{cm^2V^{-1}s^{-1}}$ for holes in monolayer SnS_2. The electron carrier mobilities of SnX_2 are higher than those of monolayers MoS_2 (60.32 $\mathrm{cm^2V^{-1}s^{-1}}$) and Ti_2CO_2 (611 $\mathrm{cm^2V^{-1}s^{-1}}$) because of the lower effective mass and lower deformation potential constant of monolayer SnX_2 [139, 189]. It is lower than that for monolayer SnSe (1200 $\mathrm{cm^2V^{-1}s^{-1}}$) and phosphorene (1100 $\mathrm{cm^2V^{-1}s^{-1}}$)[140, 185].

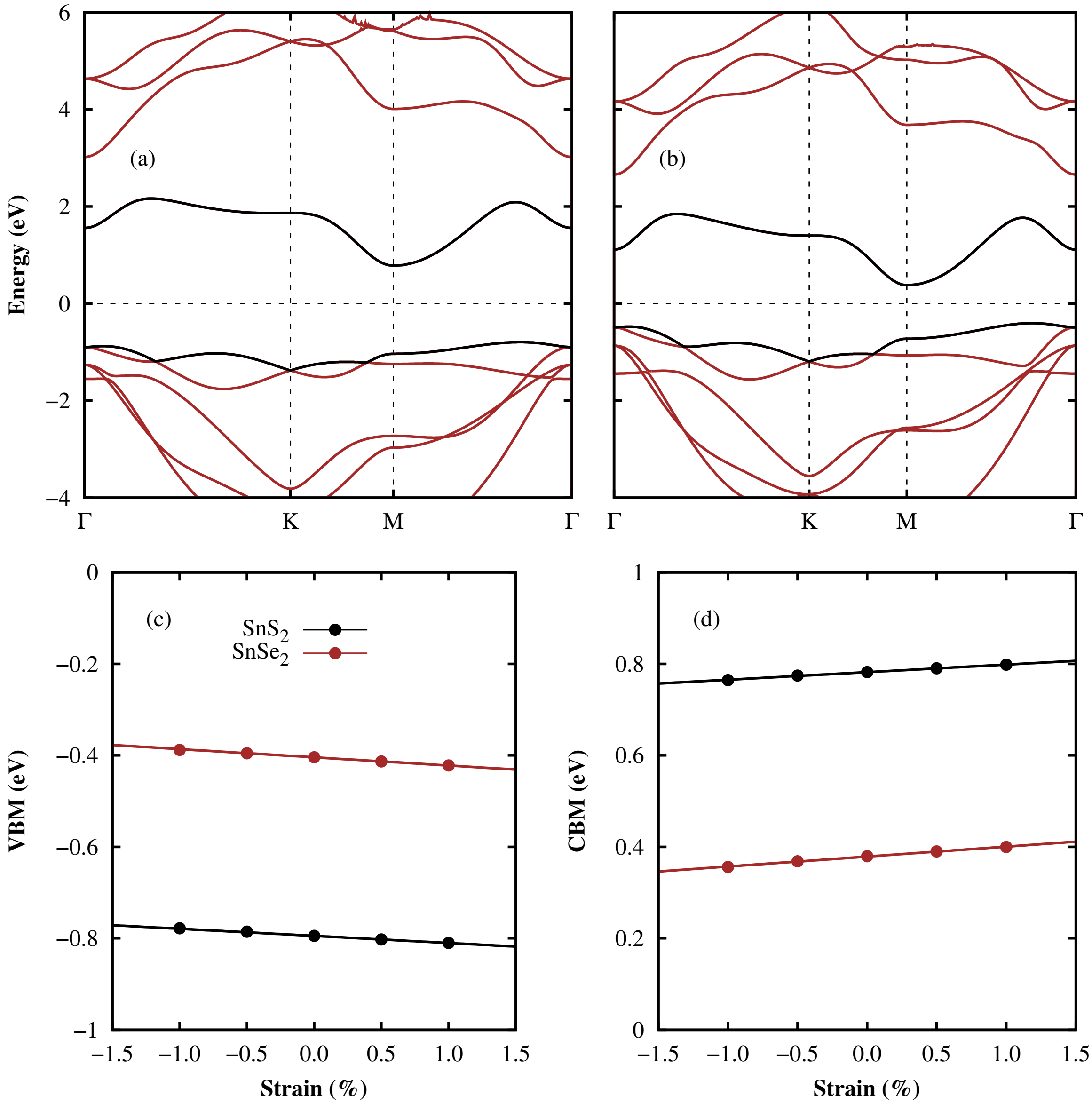

Figure 4.7: Electronic band structure of monolayer (a) SnS_2 and (b) $SnSe_2$ along high symmetry points Γ, K, and M. (c) Shift in the valence band maxima under uniaxial strain and (d) shift in the conduction band minima under uniaxial strain.

Composition	carrier	$m^*_{\Gamma-\mathrm{M}}$	$m^*_{\mathrm{K-M}}$	m_d	E_1 (eV)	μ (cm^{2}V^{-1}s^{-1})	τ (fs)
SnS_2	electron	0.73	0.30	0.46	-2.34	756.60	314.03
	hole	-2.12	-0.40	0.92	-1.97	186.44	225.93
$SnSe_2$	electron	0.71	0.31	0.47	-2.79	462.61	186.74
	hole	-2.06	-0.39	0.89	-2.37	115.65	135.46

Table 4.2: Effective mass ($m^*_{\Gamma-\mathrm{M}}$, $m^*_{\mathrm{K-M}}$), average effective mass (m_d), in-plane stiffness (C^{2D}), deformation constant (E_1), and mobility (μ) for hole and electron in single layer SnX_2at 300 K. The unit of effective masses is m_e.

Such large electron carrier mobilities grant *n*-type electronic properties to monolayer SnX_2 materials.

4.4 Summary

In conclusion, we have explored ultralow lattice thermal conductivity and high carrier mobility in monolayer SnS_2 and $SnSe_2$ using first principles calculations. In order to explain the ultralow lattice thermal conductivities, we have calculated the phonon spectra, phonon group velocities, Grüñeisen parameters, and Debye temperatures. Monolayer $SnSe_2$ has lower lattice thermal conductivity than SnS_2 due to its low phonon group velocity, heavy mass of Se, strong anharmonicity, and low Debye temperature. The contribution of each vibrational mode to the lattice thermal conductivity is calculated and the size dependence of the lattice thermal conductivity is also discussed. The phonon MFPs for these materials are so large that phonon transport properties can be changed more efficiently by nanostructuring. The electron and hole mobility of monolayer $SnSe_2$ is higher than that of monolayer SnS_2 because of the low effective masses. The ultralow lattice thermal conductivity and high carrier mobility of monolayer SnS_2 and $SnSe_2$ suggest that they are good candidates for thermoelectric applications.

Chapter 5

Phononic thermal transport in two-dimensional indium chalcogenide compounds (InX, X=S, Se, Te)

5.1 Introduction

Thermal transport is a critical and key parameter in the optoelectronic, modern electronics, heat dissipation, and thermoelectric devices. In semiconductors and insulators, thermal transport derives from the atomic vibrations called phonons[13, 62, 190]. Thermoelectric materials, which convert the waste heat into useful electrical energy, are very promising to solve the energy and environmental crisis[103, 191]. The performance of thermoelectric devices measures by a dimensionless figure of merit (ZT), $ZT = \sigma S^2 T/(\kappa_e + \kappa_l)$, where σ, S, κ_e, κ_l, and T are the electrical conductivity, Seebeck coefficient, electronic thermal conductivity, lattice thermal conductivity, and temperature. The electronic transport properties σ, S, and κ_e are very difficult to optimize because they are interrelated to each other. Thus, minimizing the lattice thermal conductivity or search materials with low littice thermal conductivity is a suitable option to improve the ZT. Slack *et al*. reported that low bonding interaction, high anharmonicity, high average atomic mass, low Debye temperature, and complex structure required for the low lattice thermal conductivity[29]. High anharmonicity and low Debye temperature increase the phonon scattering rates which lower the lattice thermal conductivity. High average atomic mass reduces the phonon vibration frequency, phonon group velocities and hence lattice thermal conductivity.

Many studies have been done based on first principles and classical molecular dynamics in search of the ideal two-dimensional thermoelectric material with a low lattice thermal conductivity[126, 149, 192]. Two-dimensional semiconductors such as silicene[22], borophene[193], stanene[150], arsenene[194], phosphorene[149], and monolayers SnSe[126, 162], MoS_2[40], WSe_2[164] extensively studied and explored low lattice thermal conductivity, but still, efforts are needed to find materials, which show good electronic transport properties as well as low lattice thermal conductivity. We cannot use graphene for thermoelectric applications because of the high lattice thermal conductivity[16].

Two-dimensional indium chalcogenide compounds are polar materials due to the considerable charge transfer between indium and chalcogen atoms which causes to the creation of dipoles. A long-range electric field generates by the relative motion of these dipoles, which produces interaction between the dipoles. This dipole-dipole interaction strongly affects the frequencies of the optical branches and causes to splitting between the longitudinal optical (LO) and transverse optical (TO) branches near the Γ-point. It has been shown both theoretically and experimentally that the long-range dipole-dipole interactions lead to LO-TO splitting near the Γ-point in bulk InSe. We expect stronger dipole-dipole interaction in monolayer InX compared to their bulk counterpart because of their smaller dielectric permittivity. Thus, the effect of dipole-dipole interaction on the phonon spectra and lattice thermal conductivity would be meaningful to investigate. Secondly, it reported that monolayers InX have low elastic moduli in comparison to other two-dimensional materials[195] and contains heavy elements such as In, Te, and Se, and we expect low lattice conductivity. Wickramaratne *et al.* have predicted excellent electronic thermoelectric properties for these monolayers[196] , but there is a lack of study about phononic thermal transport properties which motivates us to study.

Here, we present a comprehensive investigation of the phonon transport properties and intrinsic lattice thermal conductivities of the monolayers InX by solving the PBTE based on first-principles calculations. The long-wavelength dispersion of longitudinal optical branch and lattice thermal of these monolayers are strongly affected by the non-analytical correction to the dynamical matrix, and it is found that the lattice thermal conductivity of monolayer InS is increased 23.17%. Lattice thermal conductivity trend ($\kappa_{\mathrm{InS}}>\kappa_{\mathrm{InSe}}>\kappa_{\mathrm{InTe}}$) is explained with the help of the phonon spectra and its anharmonicities. . The predicted lattice thermal conductivity value of the monolayer InTe is lower than silicene, phosphorene, monolayers MoS_2 and $MoSe_2$. Furthermore, the contribution of each mode toward total lattice thermal conductivity is extracted and we also discuss the dependence of the lattice thermal conductivity on temperature and size.

5.2 Methodology

The optimized lattice parameters and interatomic force constants (IFCs) are obtained by using plane augmented wave method[101] based on density functional theory calculations with VASP[129]. We use generalized gradient approximation parameterized by the Perdew–Burke–Ernzerhof (PBE)[93] as exchange-correlation potential with a plane wave energy cutoff of 500 eV. All atoms in the unit cell are allowed to relax until the maximum force on each atom is smaller than 10^{-4} eV/Å with a k-point mesh of 25×25×1. A vacuum thickness of 25 Å is used in order to avoid interactions between the periodic images.

Harmonic force constants are determined using the finite displacement method as implemented in the Phonopy package[134]. A 6×6×1 supercell is used for the calculations of the phonon spectra, phonon group velocity, and harmonic constants. A 5×5×1 supercell is employed for the anharmonic force constants including the fifth nearest neighbor interaction. ShengBTE code[133] is used to calculate the lattice thermal conductivity with a q-point mesh of 120×120×1.

5.3 Results and Discussions

5.3.1 Structure and phonon dispersion

Bulk indium chalcogenides exist in rhombohedral, tetragonal, cubic, orthorhombic, monoclinic, and hexagonal structures[197–199]. Here, we study only the energetically and dynamically stable hexagonal monolayer of indium chalcogenides with space group $P\bar{6}m2$ (187) with four atoms in the primitive unit cell as shown in Fig. 5.1. The optimized lattice parameters of monolayer InS, InSe, and InTe are a=b=3.919, 4.093, and 4.382 Å, respectively, and they agree well with previous reports[200] (See Table 5.1). The vertical distance between two chalcogen atoms (d_{X-X}) is used as a thickness in the lattice thermal conductivity calculation.

The phonon band structures are shown in Fig. 5.2. Two in-plane acoustic modes (longitudinal acoustic (LA) and transverse acoustic (TA) modes) are linear near at the Γ-point, and one out-of-plane acoustic mode (flexural acoustic (ZA) mode) has a quadratic nature near the Γ-point. The quadratic nature of ZA mode is a common feature of the two-dimensional materials, and it studied very well for graphene[13], hexagonal boron nitride[201], silicene[22], and monolayer MoS_2[202]. The ZA mode is critical in thermal transport because it contributes the major part of the lattice thermal conductivity in graphene[13]. The absence of the imaginary line in phonon band structures confirms the dynamical stability of these monolayers. The phonon dispersions of these monolayers look similar, and the band gap between low-frequency optical

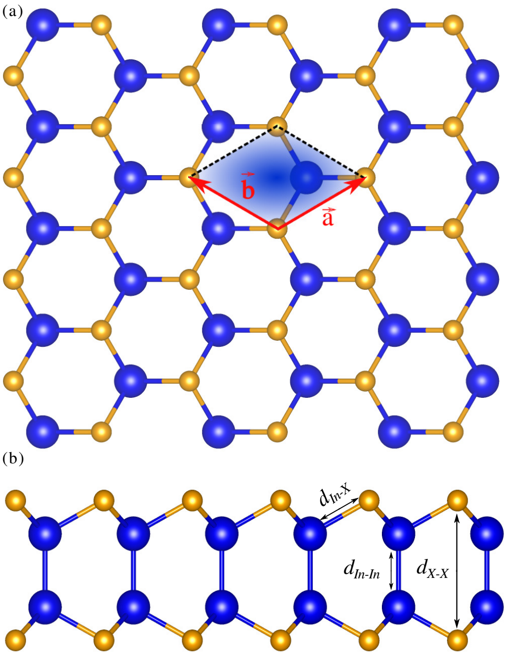

Figure 5.1: Atomic crystal structure of monolayer InX (X=S,Se,Te) from (a) top and (b) side views. The arrows indicate lattice vectors and the dash lines represent a unit cell. Blue and brown spheres, respectively represent the In and X atoms. (c) The representation of optical branches vibration in the long-wavelength limit.

Table 5.1: The calculated lattice constants (a), the distance between Indium atoms (d_{In-In}), the distance between Indium and chalcogen atoms (d_{In-X}), and the vertical distance between chalcogen atoms of the monolayer InX. The values in parentheses are taken from ref.[200] .

Composition	a (Å)	d_{In-In}(Å)	d_{In-X} (Å)	d_{X-X} (Å)
InS	3.919 (3.92)	2.827 (2.83)	2.551	5.182 (5.18)
InSe	4.093 (4.09)	2.816 (2.83)	2.689	5.385 (5.38)
InTe	4.382 (4.38)	2.823 (2.82)	2.884	5.596 (5.60)

Table 5.2: The dielectric constants and Born effective charges of the monolayer InX.

Composition	ε_{xx}=ε_{yy}	ε_{zz}	In $Z^*_{xx} = Z^*_{yy}$(e)	In Z^*_{zz}(e)	X $Z^*_{xx} = Z^*_{yy}$(e)	X Z^*_{zz}(e)
InS	2.912	1.373	2.466	0.293	-2.466	-0.293
InSe	3.305	1.409	2.505	0.250	-2.505	-0.250
InTe	4.024	1.462	2.368	0.200	-2.368	-0.200

modes and high-frequency optical modes is 82.4, 41.3 and 27.8 cm^{-1} for the monolayer InS, InSe, and InTe, respectively.

The non-analytical corrections are applied to the dynamical matrix by calculating the dielectric constants and Born effective charges as summarized in Table 5.2, which split longitudinal optical (LO) and transverse optical (TO) branches at the Γ-point in these monolayers as shown in Fig.5.2. These LO-TO splitting are very strong and they are about ten times larger than monolayer MoS$_2$.The polarization density produced by the atomic displacement (u^a_{LO}) and the associated long-range electric fields are the responsible for the LO-TO splitting. The polarization density (P) Fourier transform can be written as:

$$P(q_p) = \frac{e^2}{V}\sum_a Z_a.u^a_{LO}, \tag{5.1}$$

where e is the electron charge, q_p is the in-plane phonon momentum, and Z_a is the Born effective charges tensor associated with atom a. The polarization charge density ($q_p.P(q_p)$) is zero for the TO branch because the direction of propagation and the polarization is orthogonal to each other and the LO branch produces an electric field. The restoring force on the atoms is increased due to the electric field, and additional energy is required for the displacement of the LO branch with respect to the TO branch. The relationship between the frequency squares of these branches can be expressed as:

$$\omega^2_{LO} = \omega^2_{TO} + W_c(q_p)\frac{e^2|q_p|^2}{V}\left(\sum_a \frac{e_{q_p}.Z_a.e^a_{LO}}{\sqrt{M_a}}\right)^2, \tag{5.2}$$

where $W_c(q_p)$ is the screened Coulomb interaction (which is inversely proportional to the dielectric constant) and $e_{q_p} = q_p/|q_p|$. The LO-TO splitting depends on the screening and the momentum direction (q_p) along the Born effective charges. The large LO-TO splitting in the monolayer InS, compare to monolayer InSe and InTe, is due to the small dielectric constant which increases the screening potential.

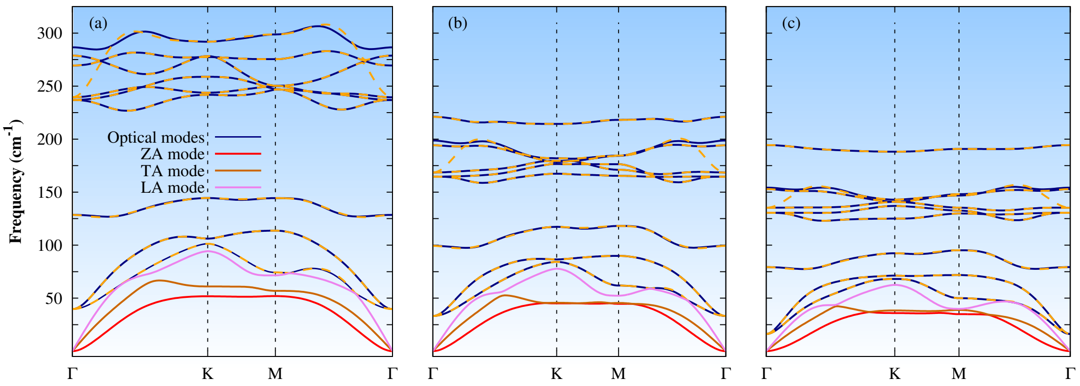

Figure 5.2: Phonon band structures of the monolayer (a) InS, (b) InSe, and (c) InTe along high-symmetry points Γ-K-M-Γ. Solid lines represent the phonon spectra in which non-analytical correction is included, and yellow dash lines represent the optical branches without non-analytical corrections.

5.3.2 Lattice thermal conductivity

The lattice thermal conductivities as a function temperature are plotted for the InS, InSe, and InTe monolayers in Fig. 5.3 (a). The lattice thermal conductivities decrease in the temperature range from 100 K to 750 K, and they are fitted well with the $\kappa_l \sim 1/T$ relationship, which demonstrates that the dominant three-phonon scattering processes in this temperature range are the Umklapp process. The lattice thermal conductivities of the three monolayers are 56.45 W/mK (InS), 44.43 W/mK (InSe), and 33.05 W/mK (InTe) at room temperature. Our calculated value of lattice thermal conductivity for the monolayer InSe agrees well with the recently reported value[203]. They possess low lattice thermal conductivity, especially for monolayer InTe. The lattice thermal conductivity of InTe is lower as compared to a lot of other two-dimensional materials, such as silicene[22], phosphorene[149], hexagonal boron nitride[50], and monolayer MoS_2[40]. The lattice thermal conductivities of the monolayers InX are higher than monolayer SnSe[162], SnS[162], $SnSe_2$[204], SnS_2[204], and stanene[150]. The possible reasons of lower lattice conductivity in monolayer InTe are the small phonon band gap between the optical modes because the small gap causes stronger scattering between the optical modes phonon and heavy mass of In and Te.

We have also computed the lattice thermal conductivities without the non-analytical corrections as shown in Fig. 5.3 (b) to estimate the effect of LO-TO splitting and we found that the lattice thermal conductivities are strongly affected by the dipole-dipole interactions. They are decreased by 23.17%, 21.20%, and 12.62% for monolayer InS, InSe, and InTe, respectively. The non-analytical corrections will shift the optical bands in a neighborhood of Γ-point, thus changing the amount of phase space available for three-phonon scattering. The phase space

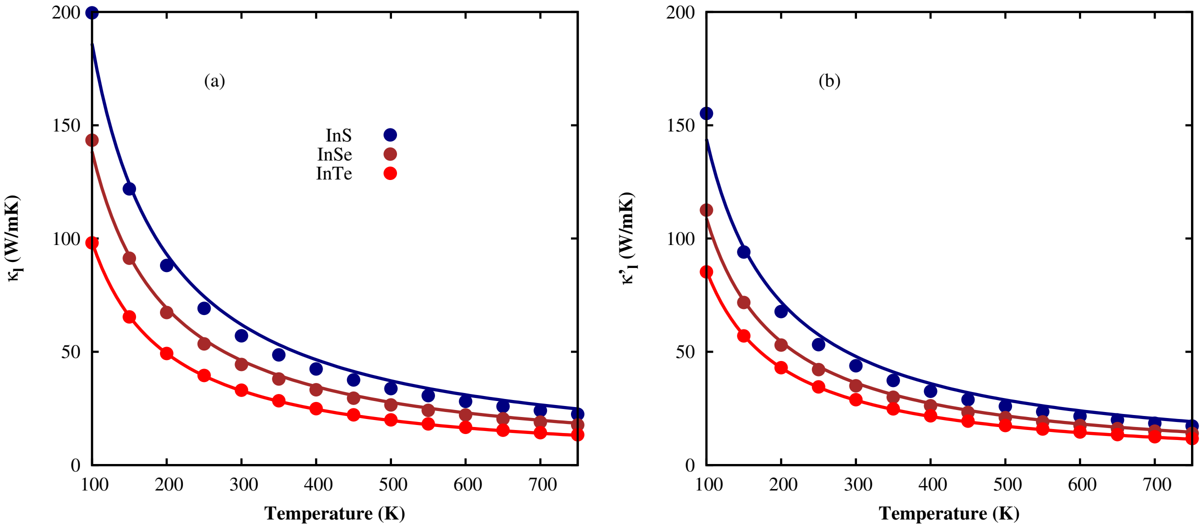

Figure 5.3: Lattice thermal conductivities of the monolayer InS, InSe, and InTe as a function of temperature calculated using iterative solutions of the phonon Boltzmann transport equation, lattice thermal conductivity (κ_l) with non-analytical corrections, and lattice thermal conductivity (κ_l') without non-analytical corrections. Solid lines are from the fitting of lattice thermal conductivities to $1/T$.

for these monolayers increases substantially when we remove the non-analytical corrections, which explains the increase in thermal conductivities.

5.3.3 Debye temperature, phonon group velocity, Grüneisen parameter, and phonon lifetime

The lattice thermal conductivities are changed drastically in the low-temperature range (100 K $\sim$ 300 K), and this change is partially attributed to the low Debye temperature (Θ_D^α) of the acoustic phonon modes as given in Table 5.3. The Debye temperature corresponds to the temperature at which a phonon mode starts to be excited, and it is defined as $\Theta_D^\alpha = \frac{h\omega_m^\alpha}{k_B}$, where α shows ZA, TA, and LA modes, and ω_m^α is the maximum frequency of the corresponding phonon mode. More phonon modes are activated in this temperature range, and the population of phonons is increased. Enhancement in the phonon population leads to an increase in phonon scattering rates and hence, the lattice thermal conductivity is dramatically decreased.

The contribution of the ZA, TA, LA, and optical branches to the lattice thermal conductivity at room temperature is calculated as given in Table 5.4. The main contributor to the lattice thermal conductivity is the LA branch because of the large LA branch phonon group velocity

Table 5.3: Debye temperature (Θ_D^α), representative mean free path (rMFP), specific heat (C_v), lattice thermal conductivity (κ_l) with non-analytical corrections, and lattice thermal conductivity (κ_l') without non-analytical corrections of the monolayer InS, InSe, and InTe.

Composition	Θ_D^{ZA}(K)	Θ_D^{TA}(K)	Θ_D^{LA}(K)	rMFP (nm)	C_v (10^5J/Km^3)	κ_l(W/mK)	κ_l'(W/mK)
InS	74.79	95.57	135.73	535.16	4.64	57.09	43.86
InSe	65.34	75.64	111.96	774.07	4.40	44.43	35.01
InTe	52.89	55.28	90.03	350.75	3.89	33.05	28.88

Table 5.4: Percentage contribution of the ZA, TA, LA, and optical phonon branches to lattice thermal conductivity at room temperature for the monolayer InS, InSe, and InTe.

Composition	ZA (%)	TA (%)	LA (%)	Optical (%)
InS	27.18	19.97	39.35	13.48
InSe	22.66	23.09	43.34	10.91
InTe	17.14	18.35	48.33	16.18

and long phonon lifetime. In the case of graphene, the main contributor is ZA branch where ZA contributes by 76%[16]. In these monolayers, the acoustic branches are granted by approximately 85%, and optical branchs are contributed approximately 15%. Optical branches contribute more significant as compared to graphene, stanene and monolayer MoS_2.

The phonon properties are investigated to understand the underlying phenomena of lower lattice thermal conductivity in these monolayers and the trend of lattice thermal conductivity (InS > InSe > InTe). The solution of the PBTE within single mode relaxation time approximation (SMRTA), the lattice thermal conductivity of a two-dimensional material can be written as $\kappa_l^{xx} = \frac{1}{2}\sum_\alpha C_{v,\alpha} v_x^\alpha.(v_x^\alpha + \Delta_x^\alpha)\tau_\alpha$, where $C_{v,\alpha}$ is the specific heat. The phonon heat capacities for the monolayers InX are calculated using the relation: $C_{v,\alpha} = \frac{k_B}{VN}\sum_\alpha(\frac{\hbar\omega_\alpha}{k_B T})^2 n_\alpha^0(n_\alpha^0+1)$ and the values are given in Table 5.3. The specific heat of the monolayer InTe is lower than those of the monolayers InS and InSe. The lower specific heat of the monolayer InTe is due to low vibrational frequency, and it is partially responsible for lower lattice thermal conductivity of InTe among monolayers InX.

Phonon group velocity is an important factor that affects the lattice thermal conductivity. Phonon group velocities of monolayer InX are calculated along the Γ-M, and Γ-K directions as shown in Fig. 5.4 and they are determined from the slope of the phonon dispersion. Phonon group velocities of the monolayer InTe are found lower as compared to the monolayer InS and InSe and the acoustic phonon group velocities for monolayer InTe at the Γ-point are 1793 m/s and 2747 m/s for TA, and LA branches, respectively. The group velocities of the optical modes are very low as compared to the acoustic branches, and this low group velocities of the

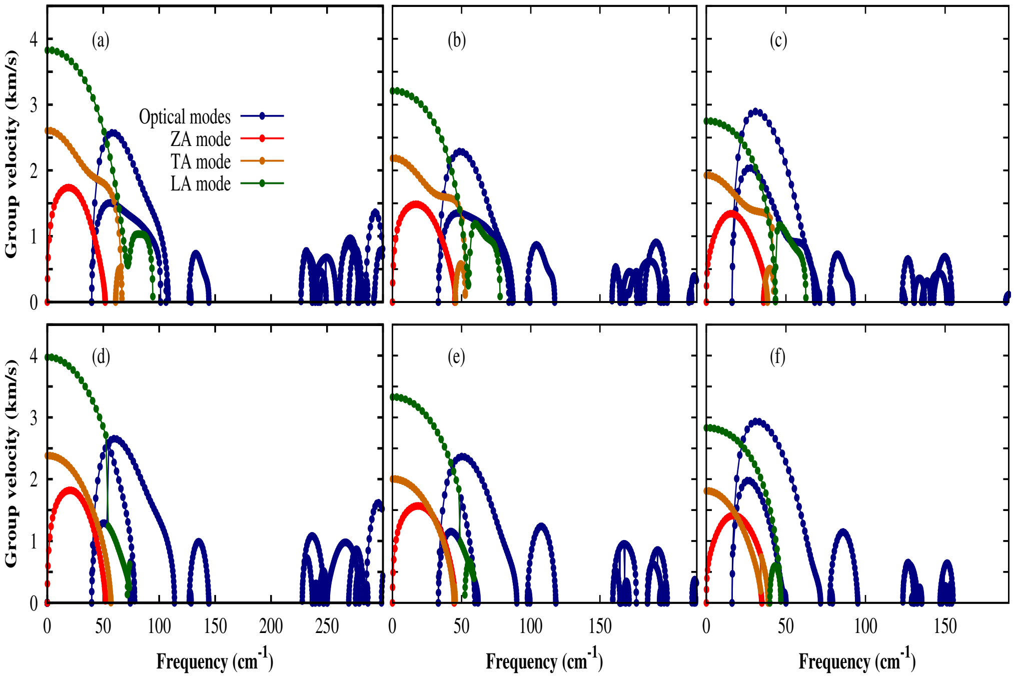

Figure 5.4: Branch-dependent phonon group velocities with non–analytical corrections in monolayer (a,d) InS, (b,e) InSe and (c,f) InTe along the Γ-K and Γ-M directions, respectively.

optical branches cause lower contribution to lattice thermal conductivity.

The phonon lifetimes are extracted for each phonon mode in order to get more physical insight as shown in Fig. 5.5. The phonon-phonon scattering rates are dominated by isotopic and boundary scattering rates in the finite sample. In the monolayer InS, ZA mode is contributed 27.40% to the lattice thermal conductivity (larger than LA, TA and optical modes) because of longer phonon lifetime. However, LA mode is contributed more considerable in the monolayer InSe and InTe due to longer phonon lifetimes and large group velocity. The optical phonon lifetimes are very short that why they contribute very little to the lattice thermal conductivity.

Grüneisen parameter measures the anharmonicity in the chemical bonding, which drives the normal and umklapp phonon-phonon scattering processes. It is calculated from the change in phonon frequency with respect to change in lattice constant, and it can be expressed as:

$$\gamma_\alpha = -\frac{a_0}{\omega_\alpha}\frac{\partial \omega_\alpha}{\partial a}$$

where γ_α is the Grüneisen parameter of the α branch and a_0 is the equilibrium lattice constant. The Grüneisen parameter for each phonon branch is computed as shown in Fig. 5.5 (a-c) to

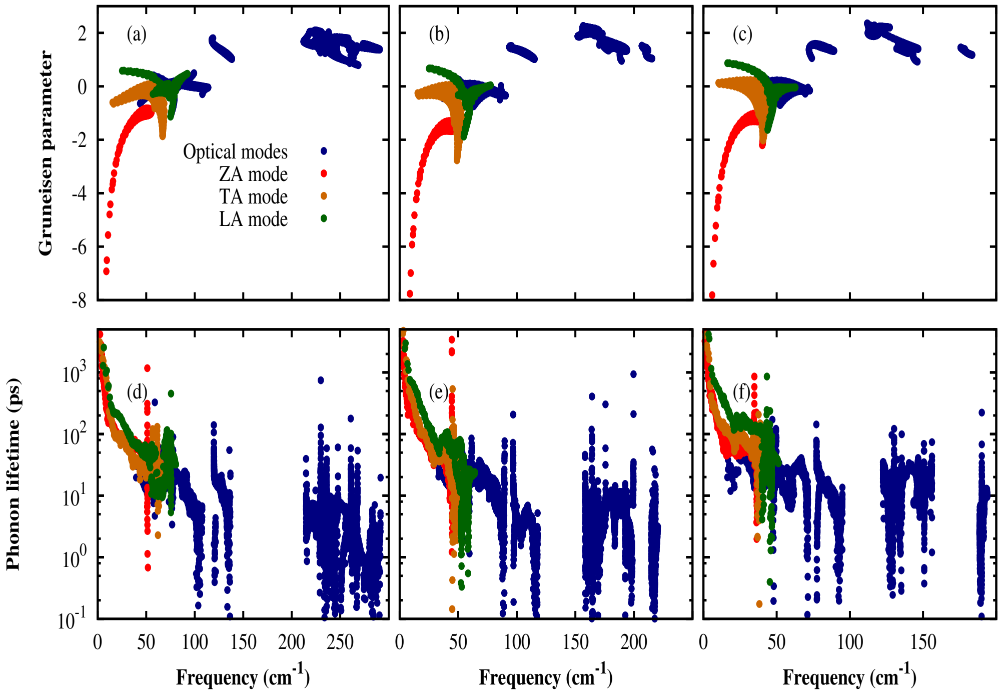

Figure 5.5: Mode dependent Grüneisen parameters and phonon lifetimes at room temperature as a function of frequency for the monolayer InS (a,d), InSe (b,e), and InTe (c,f), respectively.

clarify the origin of low lattice thermal conductivities in these monolayers. The Grüneisen parameters are anomalously large for these monolayer InX, which lead to the low lattice thermal conductivity. Large Grüneisen parameters are the consequence of weak bonding in these monolayers. Strong anharmonicity leads to short phonon lifetime because phonon-phonon scattering rates also depend on anharmonicity of the material.

5.3.4 Size-dependent lattice thermal conductivity

The effect of size on the lattice thermal conductivity is significant in the nanoscale devices because when the sample size decreases from maximal phonon mean free path (MFP), the phonon-boundary scattering is increased and thus lattice thermal conductivity is decreased. To investigate the size-dependence, the cumulative lattice thermal conductivity as a function of phonon MFP is calculated as illustrated in Fig. 5.6 for the monolayer InX . The cumulative lattice thermal conductivity increases as phonon MFP increases and saturates at maximal phonon MFP . The maximal phonon MFP values for the monolayer InS, InSe and InTe, are 61.35 μm, 35.11 μm, and 29.15 μm, respectively. The cumulative lattice thermal conductivity

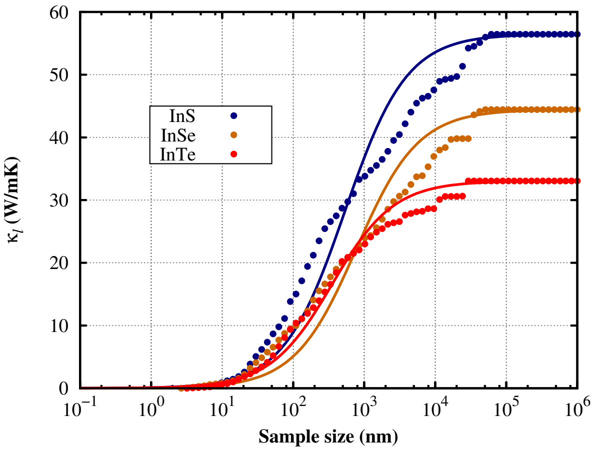

Figure 5.6: Cumulative lattice thermal conductivity with non-analytical corrections as a function of phonon mean free path for monolayer InX at room temperature. The Equ.5.3 fits the curves, and they are plotted with solid lines.

is fitted to a uniparametric function in Eq. 5.3 to evaluate the representative mean free path (rMPF, L_0) and the fitted curves are shown in Fig.5.6. The uniparametric function is given as

$$\kappa_l(L) = \frac{\kappa_l^{max}}{1+\frac{L_0}{L}} \tag{5.3}$$

where κ_l is the cumulative lattice thermal conductivity, and κ_l^{max} is the maximal lattice thermal conductivity. The rMFP values are tabulated in Table 5.3, which are larger than those of phosphorene, monolayer SnS_2 and $SnSe_2$, and smaller than that of stanene[150, 204]. The rMFP is very important in the designing of nanostructure because the phonon-boundary scattering dominates over the three-phonon scattering when the size of the sample below rMFP.

5.4 Summary

In conclusions, phonon thermal transport properties, and temperature- and size-dependent lattice thermal conductivities of the monolayer InX investigated by employing first-principles calculations coupled with an iterative solution of the phonon Boltzmann transport equation The lattice thermal conductivity of these monolayers decreased with increasing temperature and perfectly follows the relation $\kappa_l \sim 1/T$ The predicted values of the lattice thermal conductivity at room temperature are low as compared to lots of other two-dimensional materials. The low lattice thermal conductivities originated from the strong anharmonicity, low phonon group velocity, low Debye temperature, and short phonon lifetimes. The lattice thermal conductivity can be effectively reduced by nanostructuring due to the large phonon MFP. Our work proposes that these materials can be considered for thermoelectric applications.

Chapter 6

Strain engineering of phonon thermal transport properties in monolayer 2H-$MoTe_2$

6.1 Introduction

The evolution of the two-dimensional transition metal dichalcogenides (TMDs) as a new class of materials, offers unique electronic, optical, mechanical, and thermal properties[205, 206]. Two-dimensional TMDs are bringing numerous applications in next-generation energy storage, optoelectronic, nanoelectronic, and thermoelectric devices[159, 161, 206–208]. TMDs have the chemical formula MX_2, where M is a transition metal and X stands for a chalcogen atom[209, 210]. Since bulk TMDs form layered structures and the interlayers are bonded weakly under van der Waals interactions, each layer of TMDs can be easily exfoliated[211, 212]. Most of monolayer TMDs exist in the H phase (trigonally coordinated) or the T phase (octahedrally coordinated) while a very few of them exist in the both H and T phases[206]. Monolayer $MoTe_2$ has gained much attention and been explored due to its unique properties such as the strong binding energy, the direct band gap (1.1 eV), and the strong spin-orbit coupling, and it has been comprehensively studied for valleytronics and exciton and trion effects[213–216].

In semiconductors and insulators, heat is carried by phonons while electrons contribute very little even at low temperature. Therefore, lattice thermal conductivity is commonly used to analyze thermal transport phenomena in materials. Low lattice thermal conductivity is required for the thermoelectric [118, 217] and thermal rectification[218] applications. Many two-dimensional materials such as monolayers of SnSe, SnS, GeSe, GeS, $SnSe_2$, SnS_2, phosphorene, and stanene show very low lattice thermal conductivities[28, 126, 149, 162, 204]. Highly thermal conducting materials are used in the power sources and transistors to dissipate waste heat efficiently[219]. Graphene, hexagonal boron nitride (*h*-BN), and pentagonal monolayers such as penta-Gr, penta-SiC$_2$ and penta-SiN$_2$ are highly thermal conducting materials[28, 50, 52]. Phonon thermal tranport properties of monolayer 2H-MoTe$_2$ are not yet studied and we expect low lattice thermal conductivity due to the heavy atomic masses of Mo and Te.

Strain is a very useful and effective tool to enhance the performance of the semiconducting devices. It can tune electronic, optical, and thermoelectric properties. However, the effect of tensile strain on the phonon thermal transport of two-dimensional materials is unpredictable because the flexural or out-of-plane acoustic (ZA) mode becomes harder and the transverse acoustic (TA) and longitudinal acoustic (LA) modes become softened. The lattice thermal conductivities of graphene[49], *h*-BN[50], silicene[22], antimonene[51], germanene[23], stanene[23], monolayer penta-SiC$_2$[52], and multilayer graphene[53] are increased under tensile strain and the enhancement in the lattice thermal conductivities are attributed to the anomalous behavior of the ZA mode and the increase in lifetime of the ZA mode phonons under tensile strain. While the lattice thermal conductivities for monolayer MoS$_2$[54] and penta-Gr[52] are decreased. We have choosen monolayer MoTe$_2$ (a widely used material in the nanoscale devices) to study the phonon thermal transport properties for two reasons: (1) MoTe$_2$ has a band gap around 1.1 eV and we expect low lattice thermal conductivity to use it for thermoelectric applications. (2) Since nanoscale devices are usually under strain and heat conduction is sensitively affected by strain, it is important to study strain-dependent thermal transport.

In this work, density functional theory (DFT) combined with the Boltzmann transport equation (BTE) is used to calculate the phonon transport properties and lattice thermal conductivities of the unstrained and strained monolayer 2H-MoTe$_2$. By applying the biaxial tensile strain, the LA and TA modes are softened, which decreases phonon group velocity. The phonon lifetime reduces under the tensile strain due to the increase in the phonon-phonon scattering rate. The role of strain on Grüneisen parameter and heat capacity is also discussed. Since the decrease in phonon group velocity and phonon lifetime makes the lattice thermal conductivity decreased significantly, the tensile-strained monolayer 2H-MoTe$_2$ can be a good candidate for thermoelectric applications.

6.2 Methodology

Harmonic (second order) and anharmonic (third order) interatomic force constants are needed for calculating the lattice thermal conductivity and they are computed using the finite displace-

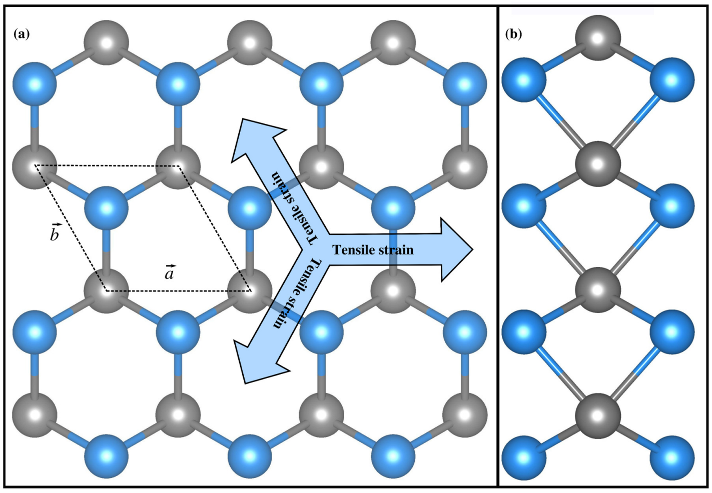

Figure 6.1: (a) Top view and (b) side view of the 2H-MoTe$_2$ monolayer structure, Mo and Te atoms are represented by grey and skyblue spheres, respectively. The arrows indicates stretching of the monolayer.

ment method with the total energy calculations[135, 220]. All the total energy calculations were carried with the density functional theory (DFT) calculations using the VASP[129]. The projector augmented wave method[101] and the generalized gradient approximation within the Perdew-Burke-Ernzerhof [93] exchange correlation functional were used with a plane-wave energy cutoff of 500 eV. For geometry optimization, the electronic stopping criterion was set to 10^{-8} eV with a 25×25×1 k-mesh and all atoms in a unit cell were relaxed until Hellmann-Feynman forces were less than 0.001 eV/Å. A 7×7×1 supercell was used to calculate the harmonic force constants and a 5×5×1 supercell was used to calculate the anharmonic force constants and up to the 10th nearest neighbors were included. The Phonopy code[134] was used to compute harmonic force constants and phonon transport properties and the ShengBTE code[133] was used to compute the lattice thermal conductivities. A q-point grid of 90×90×1 was considered for the lattice thermal conductivity calculations.

6.3 Results and discussions

6.3.1 Role of tensile strain on the lattice thermal conductivity

Fig. 6.1 shows the top and side views of the relaxed monolayer 2H-MoTe$_2$ with a lattice constant of 3.55 Å in $P3m1(156)$ space group and it is well agree with previous reports[221, 222]. Mo is sandwiched between two Te layers to form a trigonal prismatic 2H-MoTe$_2$. The vertical distance between two Te layers and the Mo-Te bond length are 3.61 Å and 2.53 Å,

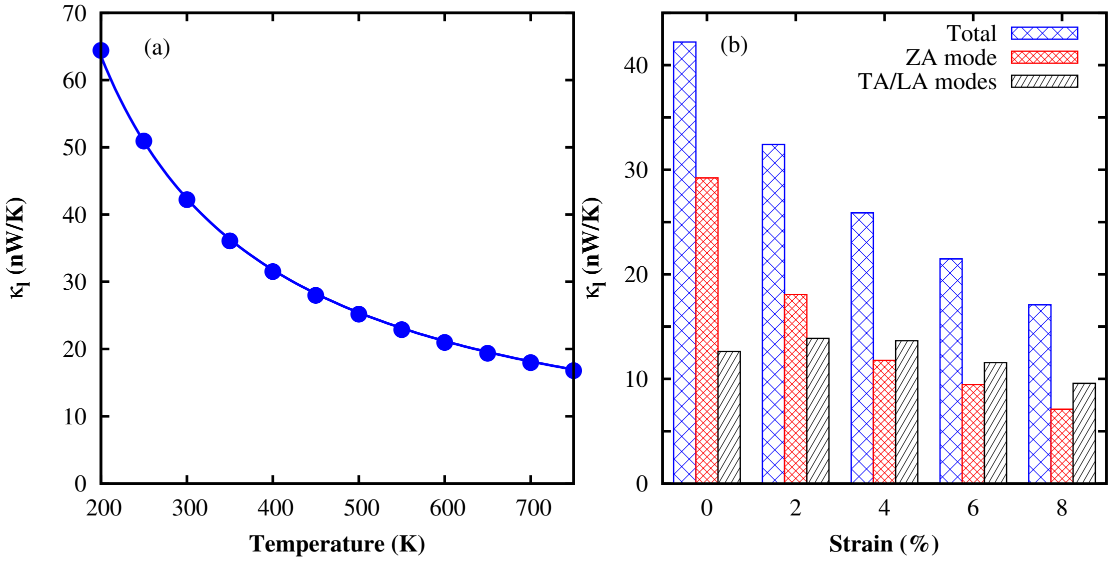

Figure 6.2: (a) Lattice thermal conductivity of monolayer 2H-MoTe$_2$ as a function of temperature, (b) total lattice thermal conductivity, contribution of the ZA and TA/LA modes to the lattice thermal conductivity at 300 K as a function of tensile strain.

respectively.

The temperature- and strain-dependent lattice thermal conductivities for the monolayer 2H-MoTe$_2$ are calculated based on the iterative solution of the phonon Boltzmann transport equation, as shown in Fig. 6.2. The thermal conductivity of the stable monolayer decreases with increasing temperature due to the increase in phonon-phonon scattering rate, as shown in Fig. 6.2(a). The room-temperature (300 K) thermal conductivity is 42.2 nW/K in monolayer 2H-MoTe$_2$, which is lower than graphene[28], monolayer MoS$_2$[34] and larger than monolayer SnSe[162], SnS[162] and stanene[28]. We fit the lattice thermal conductivity to the inverse of the temperature, i. e. $\kappa_l^{xx'} \sim 1/T$. The solid line in Fig. 6.2(a) fits the data and it perfectly coincides with the calculated thermal conductivity.

The lattice thermal conductivities under different biaxial tensile strains are shown in Fig. 6.2(b) at 300 K. The lattice thermal conductivity at the 8% strain is decreased to 17.07 nW/K, and it is almost 2.5 times smaller than that of the unstrained 2H-MoTe$_2$. Similar trend is found in penta-Gr[52] and monolayer MoS$_2$[54]. However, in the case of graphene[49], silicene[22], stanene[23], and germanene[23], the lattice thermal conductivities are increased by increasing tensile strain because the buckled structure of silicene, stanene, and germanene become more planar under tensile strain, which leads to reflectional symmetry, and the scattering of the LA mode phonons and TA mode phonons with ZA mode phonons are reduced which increase the ZA mode phonons lifetime[190]. In the case of monolayer MoTe2, there is no reflection symmetry before and after applying strain. The phonon scattering rates are increased under tensile strain which decreases the lattice thermal conductivity. The reduction in the lattice thermal conductivity is due to the decrease in the phonon group velocity, the phonon heat capacity, and the phonon lifetime and the increase in the Grüneisen parameter as discussed in the following sections.

Next, we analyze the contribution of each mode to the lattice thermal conductivity and how these contributions are changed with tensile strain as presented in Fig. 6.2(b). For the unstrained case, the 69.2% of the contribution to the total lattice thermal conductivity comes from the ZA mode and 29.9% from the TA/LA modes. The contribution from optical modes are negligible because of the low phonon group velocity and the high phonon-phonon scattering rate. As the tensile strain increases, the contribution from the ZA mode decreases because this mode becomes harder under tensile strain, which decreases the phonon group velocity and phonon lifetime. The contribution from the TA/LA modes becomes larger due the softening of these modes. At the 8% strain, the contribution from the ZA mode reduces to 41.6% and the contribution from the LA/TA modes increases to 56.1%.

6.3.2 Phonon dispersion and Raman shift under tensile strain

Phonon dispersion is very important in order to investigate the lattice thermal conductivity. The phonon dispersions are shown in Fig. 6.3 for unstrained monolayer 2H-MoTe$_2$ and for different biaxial tensile strains. There is no imaginary line in phonon dispersion, and it confirms that monolayer MoTe$_2$ is thermally stable. The phonon dispersion curve for the unstrained case is consistent with the previously reported first principles calculations[222]. By increasing the tensile strain to 8%, the out-of-plane acoustic mode, the so-called flexural acoustic (ZA) mode, is stiffened, and the quadratic nature of the ZA mode near the Γ point turns into a straight line as shown Fig. 6.3(f). The quadratic nature of the ZA mode is due to rotational symmetry, and the rotational symmetry is broken and hence quadraticity of the ZA mode disappears when the tensile strain is applied. However, the in-plane acoustic modes (the LA and TA modes) become softened and the frequencies in phonon spectra are shifted downward under tensile strain because atoms are further away and interact less strongly (and the second derivatives of the interaction also become lower). Less stiff bonds lead to lower frequencies. The gap between the acoustic modes and optical modes becomes smaller by increasing the tensile strain due to the red-shift in frequencies of spectra. Since the acoustic modes and the optical modes are coupled with each other at the 8% tensile strain, this coupling may reduce the lattice thermal conductivity due to the increased acoustic-optical phonon scattering.

A theoretical investigation of the phonon dispersion at the $\Gamma-$point is also performed in order to find the position of the peaks in the Raman/infrared spectra. Monolayer 2H-MoTe$_2$

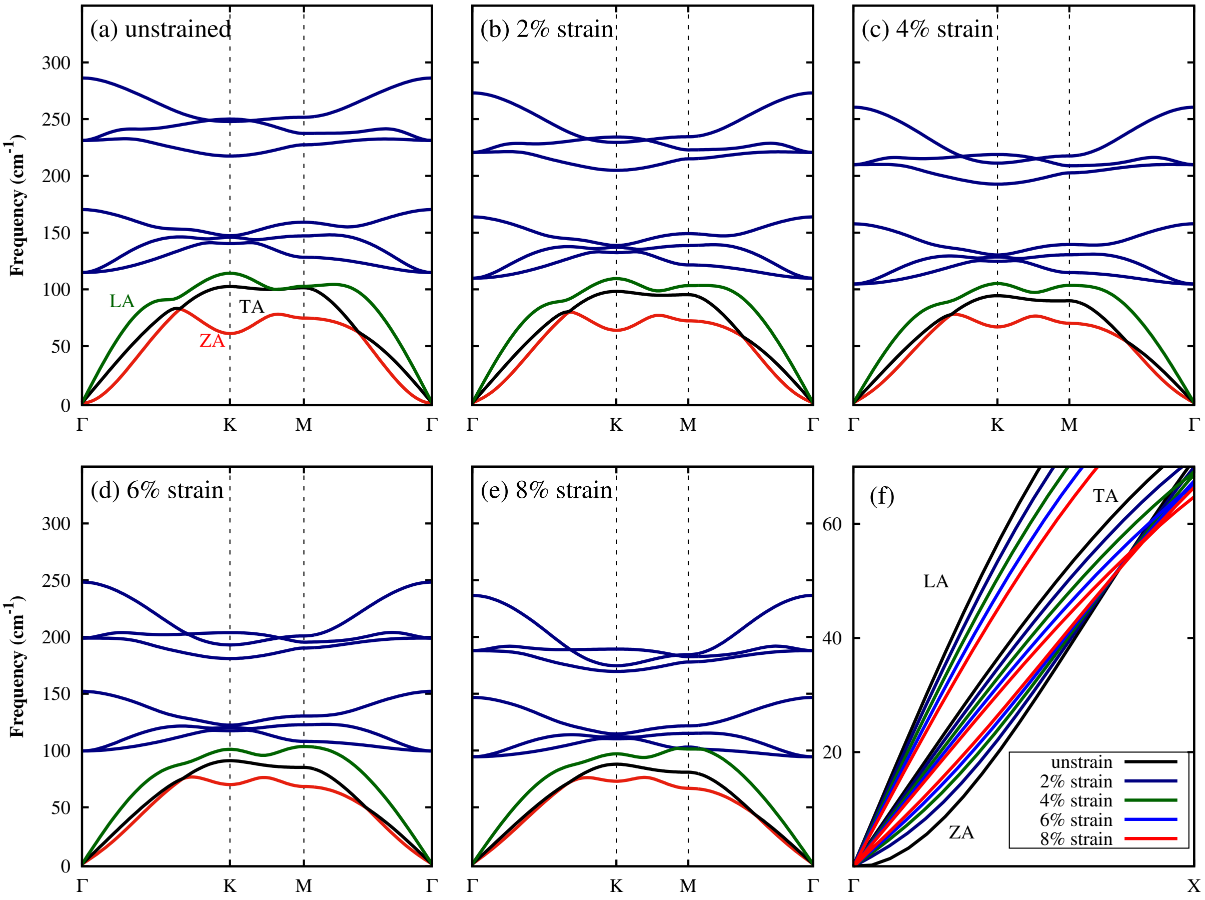

Figure 6.3: The phonon spectra of the monolayer 2H-MoTe$_2$ under different biaxial strains: (a) 0%, (b) 2%, (c) 4%, (d) 6%, and (e) 8% strains, and (f) the acoustic phonon dispersion relation along the Γ-X direction at different tensile strains

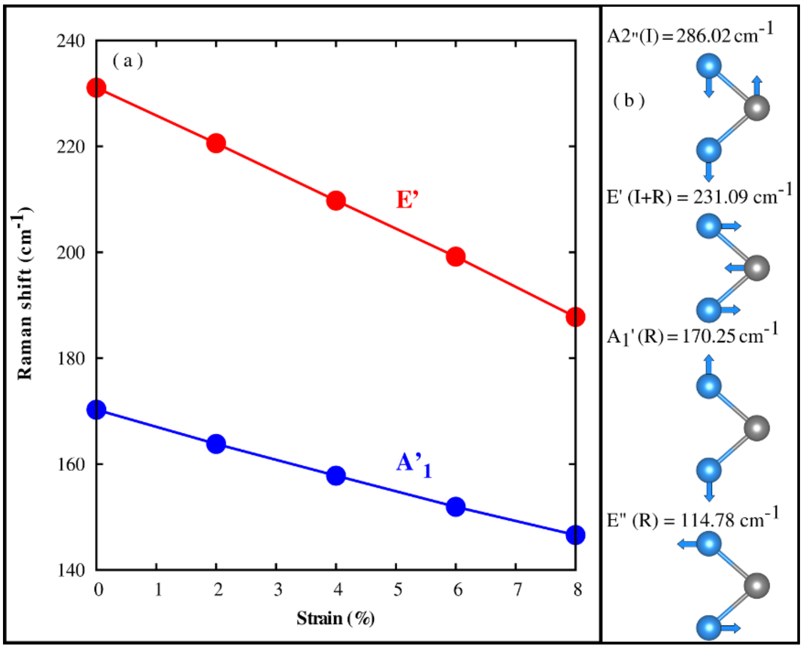

Figure 6.4: (a) Prominent peaks E’ and A$'_1$ in the Raman spectra under biaxial tensile strain and (b) schematic representation of the Raman/Infrared active modes $A''_2(I)$, $E'(I+R)$, $A'_1(R)$, and $E''(R)$ of the monolayer 2H-MoTe$_2$.

has D_{3h} symmetry and their phonons irreducible representation can be defined as[223]:

$$\Gamma \equiv 2A''_2(I) \otimes A'_1(R) \otimes 2E'(I+R) \otimes E''(R)$$

where $A''_2(I)$ is the infrared active mode, $E'(I+R)$ is the both Raman and infrared active modes and $A'_1(R)$ and $E''(R)$ are Raman active modes. The predicted values for the $A''_2(I)$, $E'(I+R)$, $A'_1(R)$ and $E''(R)$ are 286.02 cm^{-1}, 231.09 cm^{-1}, 170.25 cm^{-1} and 114.78 cm^{-1} which well agree with recently reported experimental results[224]. The $E'(I+R)$ and $A'(R)$ are the prominent peaks in the Raman spectra and the these peaks are red-shifted linearly under biaxial tensile strain as shown Fig. 6.4.

6.3.3 Effect of strain on phonon group velocity, phonon heat capacity, and Grüneisen parameter

To understand the underlying mechanism of strain-dependent lattice thermal conductivity we analyzed the the phonon group velocity, the phonon heat capacity, and the Grüneisen parameter. Strain-dependent phonon group velocities are shown in Fig. 6.5: the ZA-mode phonon group velocity at the Γ point is increased from 0.47 km/s to 1.58 km/s by applying tensile

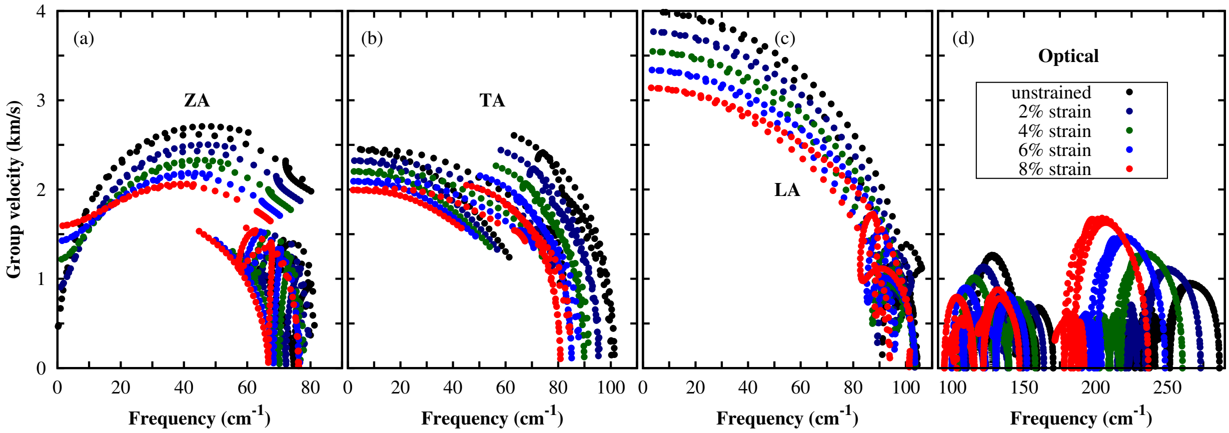

Figure 6.5: (a) Phonon group velocities of the monolayer 2H-MoTe$_2$ (a) ZA mode, (b) TA mode, (c) LA mode, and (d) optical modes under different tensile strains.

strains from 0% to 8% due to linear dispersion at the Γ point and the major part of the ZA-mode phonon group velocities are decreased under tensile strains as shown in Fig. 6.5(a). The phonon group velocities of the in-plane acoustic (LA and TA) modes are reduced with increasing tensile strain. The largest phonon group velocity at the Γ point of the TA/LA modes is decreased from 2.5/4.0 km/s to 1.99/3.12 km/s at the tensile strain of 8% because these modes become softened. One of the possible causes in reduction of the lattice thermal conductivity with tensile strain is the decrease in phonon group velocities of the acoustic modes. The velocities of optical modes are increased with increasing strain but the effect is very small because optical modes contribute very little to the lattice thermal conductivity.

Phonon heat capacity (C_{ph}) is studied under different tensile strains as shown in Fig. 6.6. For the unstrained case, the value of C_{ph} is 4.33×10^5 J/Km^3 and it is reduced to 3.79×10^5 J/Km^3 for the 8% tensile-strained case due to the decrease in the phonon density of states from linearization and stiffening of the ZA mode. It is one of the reasons why the lattice thermal conductivity is reduced under tensile strain.

The Grüneisen parameter measures the anharmonicity of a system presented in Fig. 6.6, and according to Slack's theory, it is inversely related to the lattice thermal conductivity. The Grüneisen parameter is increased from 0.77 to 1.35 at 8% tensile strain. The increase in the Grüneisen parameter reduces the lattice thermal conductivity.

6.3.4 Strain-dependent phonon lifetime

The phonon lifetime as a function of frequency and strain is plotted in Fig. 6.7. The phonon lifetime is larger at the low frequency limit (acoustic modes) due to the low phonon-phonon

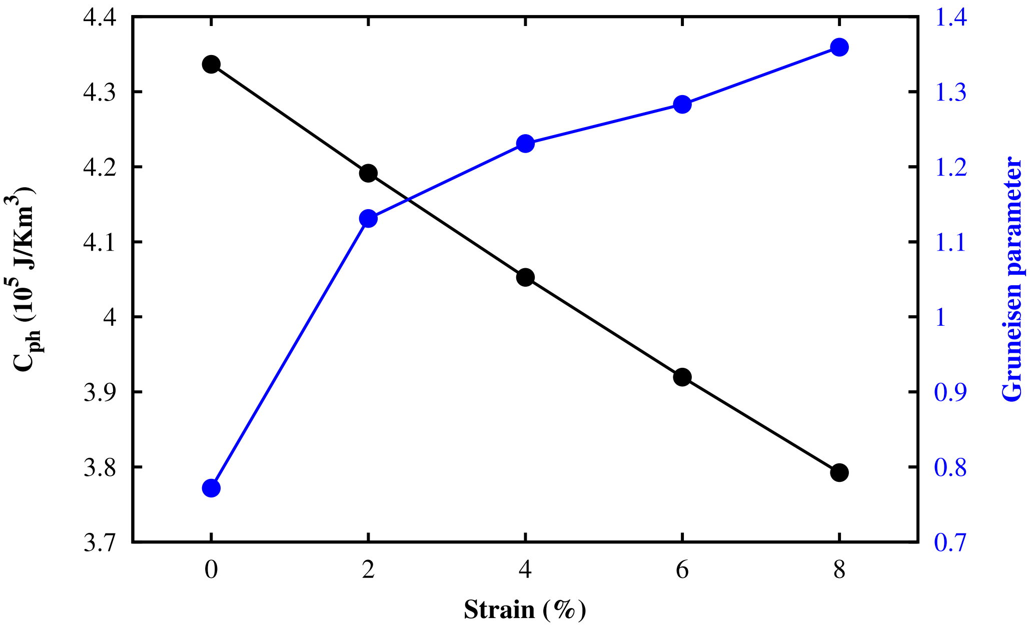

Figure 6.6: Phonon heat capacity (C_{ph}) and Grüneisen parameter as a function of strain at room temperature.

scattering rate. Thus, acoustic modes can transport nearly all heat in monolayer 2H-$MoTe_2$. The phonon lifetime is decreased under tensile strain, specially at low frequency because of the softening of the TA/LA modes, which increases phonon density of states and consequently gives rise to high scattering rate for the TA/LA phonons. Since the main contributors to the lattice thermal conductivity are the TA/LA modes at the 8% strain, the reduction in the phonon lifetime of these modes can be one of the possible causes for the reduction of the lattice thermal conductivity. Similar mechanisms are found in MoS_2[54] and ZrS_2[142] monolayers, where the phonon lifetime is decreased under tensile strain, while it is found that phonon lifetimes are increased under tensile strain in silicene[22], stanene[23], and germanene[23].

6.3.5 Effect of strain on phonon mean free path

The cumulative lattice thermal conductivity is presented in Fig. 6.8 as a function of phonon mean free path (MFP) under different tensile strains at room temperature. It characterizes how phonons with different MFPs are contributed to the total lattice thermal conductivity. Large MFP phonons contribute a significant amount to the cumulative lattice thermal conductivity at zero strain. As the tensile strain increases, the shorter MFP phonons are dominated. Furthermore, we fit our data to a parametric function to find the characteristic phonon MFP, which is

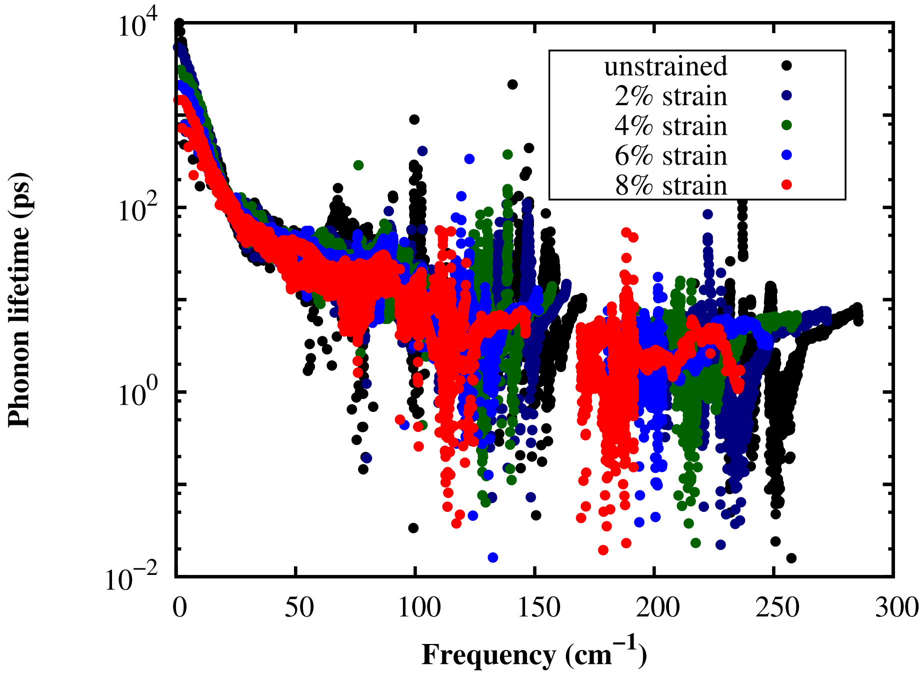

Figure 6.7: Phonon lifetimes as a function of phonon vibrational frequency under different strains at 300 K.

a very important parameter in nanostructuring. The function is given by:

$$\kappa_l(l_{\text{MFP}}) = \frac{\kappa_{\max}}{1 + l_0/l_{\text{MFP}}}$$

where $\kappa_{\max}$, l_0, and l_{MFP} are maximal lattice thermal conductivity, characteristic phonon MFP and phonon MFP, respectively. The calculated values of the l_0 at 0%, 2%, 6%, and 8% strains are 1054.22 nm, 651.36 nm, 296.25 nm, 244.31 nm and 219.39 nm, respectively. Characteristic phonon MFP (l_0) is very important parameter for experimentalist in the designing of the nanoscale devices.

6.4 Summary

In conclusion, strain-dependent thermal transport properties of the monolayer 2H-MoTe$_2$ were comprehensively investigated. We found that the lattice thermal conductivities were reduced approximately three times at the 8% tensile strain for 2H-MoTe$_2$ contrary to graphene, silicene, germanene, and penta-SiC$_2$. The reduction in lattice thermal conductivity under the biaxial tensile strain is due to the reduction in the phonon group velocity, the phonon heat

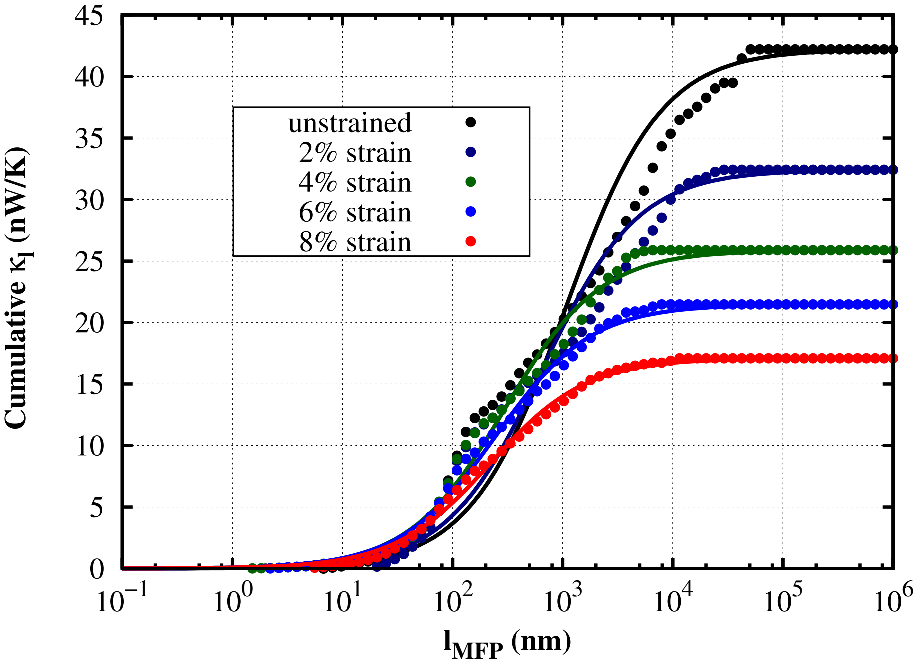

Figure 6.8: Cumulative lattice thermal conductivity with respect to MFP under different tensile strains at 300 K for the monolayer 2H-$MoTe_2$. Solid lines show the fitting curves.

capacity, and the phonon scattering time. The mode-contribution to the thermal conductivity was also evaluated. The ZA mode is the main contributor for the unstrained case, but the TA/LA modes are more significant for the 8% strain case. The lattice thermal conductivity as a function of MFP was analyzed under different tensile strains. Strained monolayer 2H-$MoTe_2$ may be more appropriate for thermoelectric applications due to the lower thermal conductivity. Our findings provide basic understanding of thermal transport in monolayer 2H-$MoTe_2$ for future applications.

Chapter 7

Superior and anisotropic thermal transport in the hybridized monolayer (BC_2N) of boron nitride and graphene

7.1 Introduction

Efficient heat dissipation is highly demanded continuing development in the nanoscale electronic industry, and extensive research is undergone to increased levels of dissipated power[59, 225, 226]. A material with high thermal conductivity has become very important for the design of the next generation nano-electronic devices[225, 226]. The performance and lifetime of large-scale integrated circuits can be increased by enhanced heat dissipation. Thus, high thermal conductivity is a crucial factor in the performance of some electronic devices, especially power electronics[59, 227]. However, low thermal conductivity and high electrical conductivity are needed for the thermoelectric applications[23, 108, 162, 228]. The heat transport in bulk materials is reduced when they are set-up on a nanoscale due to the increased in phonon scattering with boundary. However, theoretical studies showed that anomalously large thermal conductivity is possible in one-dimensional and two-dimensional materials[229, 230].

The thermal interface material (TIM) is the critical part of power generation technologies, photovoltaic solar cell, and electronics used in communications and information processing[231, 232]. TIM is inserted between the heat source and heat sink to fill the space produced by the imperfect surface finish. A solar cell converts 15% absorbed light into electrical energy and 70% into heat. Efficient heat dissipation is required to prevent solar cell from damage and degradation of the performance.

Several theoretical methods are developed to determine the accurate value of the lattice thermal conductivity, such as classical molecular dynamics (MD)[233] and iterative or single mode relaxation time approximation (SMRTA) solution of Boltzmann transport equation based on first principles[133]. Classical MD is an efficient method to determine lattice thermal conductivity but not rigorous due to the improper parameter in interatomic potential. While the first-principles calculation is fascinating due to the parameter-free procedure to predict the thermal conductivity of materials of interest and yields very accurate results in good agreement with experimental observation.

Many efforts have been devoted to searching ideal two-dimensional materials which have a suitable bandgap and high lattice thermal conductivity[28, 78, 201, 234–238]. As for graphene and hexagonal boron nitride (*h*-BN), both materials have some advantages and some deficiencies e. g. graphene has very high carrier mobility, but it is not suitable for many practical applications (such as field effect transistor) due to zero bandgap, and *h*-BN has wide bandgap but low carrier mobility due to the flat band structure at Fermi level. Recently, monolayer BC_2N (the hybrid of graphene and h-BN) has gained considerable attention due to its ideal electronic properties, such as direct bandgap of 1.6 eV and high carrier mobility[239, 240]. Liu et. al. predicted the energetically stable model among several possible models[241], and it is composed of the B-N and C-C zigzag chains as shown in Fig. 7.1. Monolayer BC_2N on the Ir(111) surface is epitaxially grown under very high vacuum[242]. Recently, Lin et al studied thermal transport properties in the monolayer BC_2N using classical MD[243] but due to imprecise results of the classical MD motivate us to study thermal transport in the hybrid monolayer using first-principles calculations, and we expect very high lattice thermal conductivity due to strong C-C bonding and light masses of the boron, carbon, and nitrogen atoms.

In this paper, we systematically investigate the thermal transport properties of the monolayer BC_2N by solving the PBTE iteratively based on first-principles calculations. We find a very high and anisotropic lattice thermal conductivity. The lattice thermal conductivity along the zigzag direction is very high as compared to armchair direction due to the strong C-C bonding along the zigzag direction. To explain ultra-high lattice thermal conductivity of the monolayer BC_2N, we calculate the phonon dispersion, phonon lifetimes and phonon group velocities. We also calculate the electronic thermal transport properties and found a very high value at room temperature. Due to the high thermal conductivity, monolayer BC_2N will be a promising material for thermal management and heat dissipation in the nano-electronic devices.

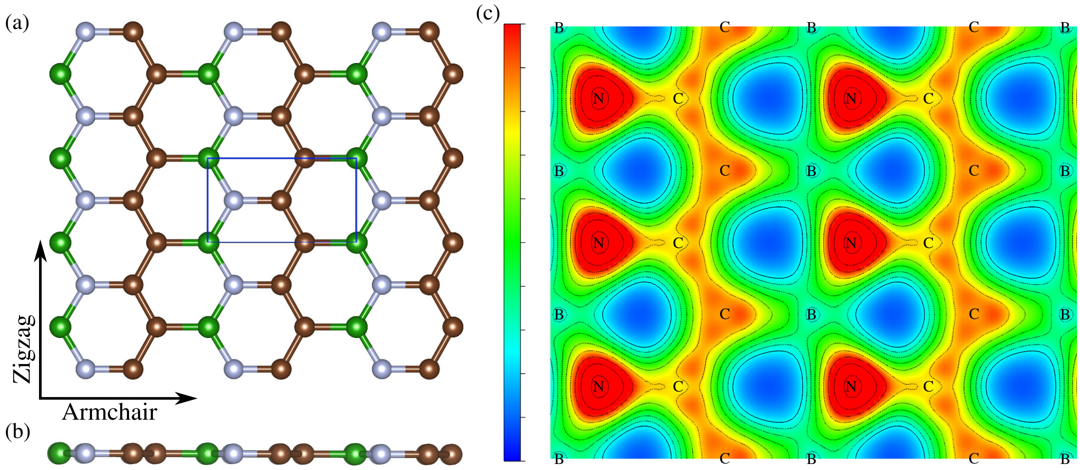

Figure 7.1: Crystal structure of the monolayer BC_2N (a) top view (b) side view. The golden, white and green spheres represent carbon, nitrogen, and boron atoms, respectively, and The arrows indicate armchair and zigzag directions (c) electron localization function of the monolayer BC_2N starts from 0 (blue) to 1 (red).

7.2 Methodology

All first-principles calculations are performed using the projector augmented wave method[101] as implemented in VASP[129] coupled with generalized gradient approximation electron-electron interaction defined as Perdew-Burke-Ernzerhof exchange-correlation functional[95]. The geometry of the system is optimized until Hellmann-Feynman force is converged to 10^{-4} eV/A and energy difference is converged to 10^{-6} eV. Kinetic energy cutoff of 600 eV is used with a $15\times15\times1$ k-points mesh, and a vacuum space of 40 Å along z-direction is taken to avoid interaction with other neighboring layers. Band structure calculation is based on the Heyd-Scuseria-Ernzerhof hybrid functional.

Harmonic and anharmonic interatomic force constants are needed for the calculation of lattice thermal conductivity and they are obtained from the first principles using the phonopy code[134] with supercell size of $6\times6\times1$ and the thirdorder.py script[40] with supercell size of $5\times5\times1$ supercells, respectively.

The electron Boltzmann transport equation is solved under relaxation time approximation (RTA), as implemented in Boltztrap code[130], is used to calculate the electrical conductivity (σ) and Seebeck coefficient (S) and can be expressed as:

$$\frac{\sigma^{\alpha\beta}(T,\mu)}{\tau} = \frac{1}{V}\int e^2 v^{\alpha}(\vec{k}) v^{\beta}(\vec{k})[\frac{\partial f_{\mu}(T,\varepsilon)}{\partial\varepsilon}]d\varepsilon$$

and

$$S^{\alpha\beta}(T,\mu) = \frac{1}{eT}\frac{\int v^{\alpha}(\vec{k})v^{\beta}(\vec{k})(\varepsilon-\mu)[\frac{\partial f_{\mu}(T,\varepsilon)}{\partial\varepsilon}]d\varepsilon}{\int v^{\alpha}(\vec{k})v^{\beta}(\vec{k})[\frac{\partial f_{\mu}(T,\varepsilon)}{\partial\varepsilon}]d\varepsilon}$$

where μ is the chemical potential, $v^{\alpha}(\vec{k}) = \frac{1}{\hbar}\nabla_{\vec{k},\alpha}\varepsilon_{\vec{k}}$ is the electron group velocity, and $f_{\mu}(T,\varepsilon)$ is the Fermi-Dirac distribution function. The electronic thermal conductivity (κ_e) is obtained from the electrical conductivity using the Wiedemann-Franz law. To ensure the accuracy of electronic transport properties, we used a very dense k-mesh of 70×70×1 in the energy calculations.

7.3 Results and Discussions

7.3.1 Geometry optimization, electron charge density, and band structure

Monolayer BC$_2$N possesses Pmm2 symmetry (C_{2v}^{1}, 25) as shown in Fig.7.1(a) and it is a hybrid monolayer of the graphene and *h*-BN. Lattice constants of the orthorhombic unit cell along the armchair and zigzag directions are 4.36Å and 2.48Å, respectively. The unit cell of the monolayer BC$_2$N composed of two carbon (C) atoms, one boron (B) atom and one nitrogen (N) atom and bond lengths of the C-C, C-N, C-B, and B-N are 1.42Å, 1.39Å, and 1.53Å and 1.44Å, respectively, well agreed with previous results[243]. The charge density of the optimized 2x3 unit cell is illustrated in Fig. 7.1 (c) and due to the lone pair of N atom, electron charge density is higher at N site which makes a stronger bond between C and N atoms. We found an anisotropic bonding behavior along zigzag and armchair directions, the bonding along the zigzag direction is stronger than armchair because of the strong covalent bonding (C-C chain). Although, the C-N bonding is stronger but there no chain along the armchair direction. The strong bonding between C and N is verified by higher Young modulus along the zigzag direction (315.62 Nm^{-1}) than armchair direction (304.67 Nm^{-1}). The Young modulus is calculated from the elastic stiffness constants of C_{11} =302.97 Nm^{-1}, C_{22} =312.22 Nm^{-1}, and C_{12}=58.29 Nm^{-1}.

Normal density functional theory calculation is not a good way to obtain the band structure because it underestimates the bandgap as compared to the experimental bandgap value. Band structure is calculated using the HSE06 hybrid functional as shown in Fig. 7.2(a) in which the horizontal dotted line represents the Fermi level. We have found that monolayer BC$_2$N is a semiconductor with a direct bandgap of 2.165 eV at the *S* symmetric point. This value is very close to the experimentally observed bandgap (2.0 eV)[244]. The valence band and the conduction band along the S-Y are very flat, and we expect substantial Seebeck coefficient

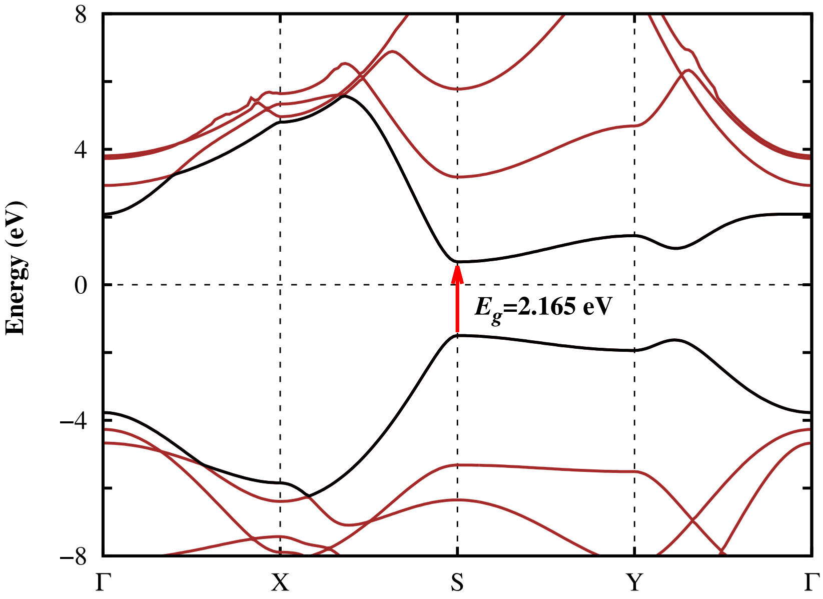

Figure 7.2: Electronic band structure of the monolayer BC_2N calculated using the HSE06 method. The black lines in the band structure represent the valence band and conduction band.

because the effective mass will very large along this direction.

7.3.2 Total and mode-dependent lattice thermal conductivity

The intrinsic lattice thermal conductivity (κ_l) as a function of temperature is calculated for the monolayer BC_2N, as shown in Fig. 3, and it is based on harmonic and anharmonic IFC's obtained from the first principles calculations. The predicted values of the κ_l at room temperature are 893.90 W/mK and 1275.79 W/mK along armchair and zigzag directions, respectively, which is largest among the semiconducting two-dimensional materials such as silicene[21], phosphorene[149], anitmonene, and monolayer $SnSe_2$[204], MoS_2[34], SnSe[126, 162], $MoTe_2$[245]. The superior lattice thermal conductivity is attributed to large phonon group velocity, long phonon lifetime, strong bonding and reflection symmetry in the monolayer BC_2N (similar to graphene)[190]. The κ_l along the armchair and zigzag directions is highly anisotropic and the ratio of $\kappa_l^{armchair}$ to κ_l^{zigzag} is 1.43. The strong anisotropy is associated with anisotropic bonding in BC_2N monolayer because bonding has a direct relation to the κ_l in the Slack's expression and anisotropic phonon dispersion along Γ-X and Γ-Y directions. The κ_l decreases with temperature ascending and perfectly follows the relation $\kappa_l \propto 1/T$. The decrease in the κ_l is originated from the increase in phonon-phonon scattering at high temperature, and it is a common phenomenon in two-dimension crystalline materials except for monolayer GaN and

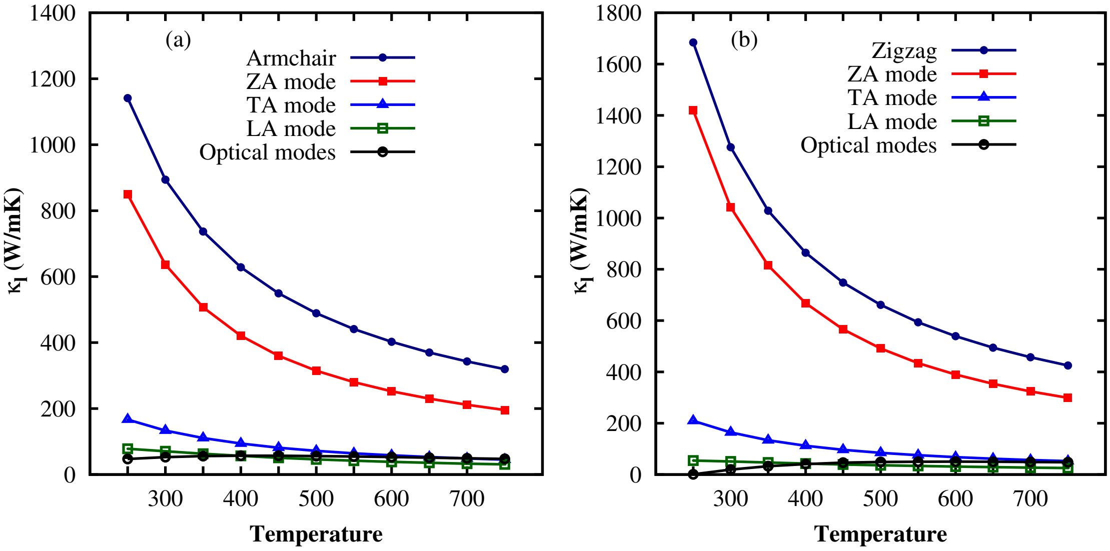

Figure 7.3: (a) Lattice thermal conductivity (κ_l) and contribution of ZA, TA, LA, and optical modes to the lattice thermal along the armchair (a) and zigzag (b) directions as a function of the temperature of the monolayer BC$_2$N.

ZnO[192, 246], in which the κ_l is dependent anomalously on temperature.

The mode-dependent contribution to the total κ_l along the armchair and zigzag directions are shown in Fig. 7.3 for the monolayer BC$_2$N. The acoustic phonon modes are the main contributor to the total κ_l in both directions, and ZA, TA and LA modes are contributed 71.22%, 14.93%, and 7.92% along the armchair direction and 81.63%, 12.86%, and 3.99% along the zigzag direction, respectively. A similar trend is found in graphene and *h*-BN. The large contribution of ZA mode is related to reflection symmetry which prevents scattering ZA mode phonons with other modes phonons. Thus, ZA mode phonons have the long lifetime, which is caused to the high lattice thermal conductivity.

7.3.3 Phonon dispersion and group velocity

Phonon band structure is obtained along the high symmetric path Γ-X-S-Y-Γ, as shown in Fig. 7.4 (a) and there is no imaginary line in the phonon band structure which confirmed the thermodynamic stability of the monolayer BC$_2$N. There are twelve branches in phonon dispersion corresponding to four atoms in the primitive cell. The lowest-three phonon branches at the Γ-point are the acoustic branches labeled in Fig. 7.4 as ZA (out-of-plane flexural acoustic), TA (in-plane transverse acoustic), and LA (in-plane longitudinal acoustic). The TA/LA modes are linear at the Γ-point similar to the bulk case, and the ZA branch has quadratic nature near the Γ-point due to the rotational symmetry, which is similar to the other two-dimensional material

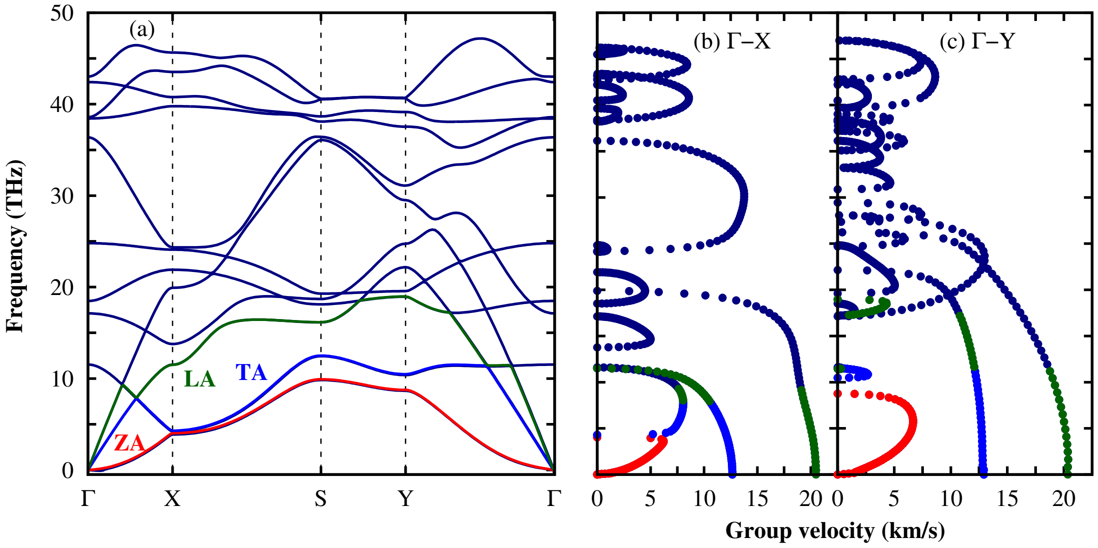

Figure 7.4: (a) Phonon spectrum along the high symmetric path Γ-X-S-Y-Γ in the first Brillouin zone, (b) phonon group velocities along the Γ-X direction, and (c) phonon group velocities along the Γ-Y direction of the monolayer BC_2N. The red, blue, green and navy colors correspond to ZA, TA, LA and optical branches, respectively.

such as graphene, *h*-BN, and silicence. This branch is essential to analyzed lattice thermal conductivity in two-dimensional materials. The gap between ZA branch and TA/LA branches along the Γ -Y direction is larger than gap along the Γ -X direction, which prevents scattering of ZA phonons with TA/LA phonons and enhance the lattice thermal conductivity along that direction. The highest frequency is located along the Γ -Y direction of 47.19 THz, which is slightly lower than graphene.

Phonon group velocities and phonon lifetimes are calculated to understand the reason for the high and anisotropic thermal transport in monolayer BC_2N. Phonon group velocity is obtained from the slope of the phonon dispersion, $v_g = \frac{d\omega(q)}{dq_{ph}}$, as shown in Fig. 7.4 (b,c). It is a very important quantity to understand thermal transport in the material. The phonon group velocity of ZA mode is exactly zero at the Γ -point due to quadratic nature of phonon dispersion and the LA mode has the largest phonon group velocities are 20.47 km/s and 20.35 km/s along the Γ -X and Γ -Y directions at gamma point. The phonon dispersion along the Γ -X and Γ -Y directions are strongly anisotropic, and this anisotropic behavior produces different phonon group velocities in different directions, which may cause anisotropic lattice thermal conductivity. The anisotropic phonon group velocities are due to the anisotropic bond strength because of phonon group velocity is directly proportional to the bond strength[62] ($v_g \sim \sqrt{K/M}$). However, since the ZA mode group velocities are smaller than TA/TA acoustic mode but the ZA mode contributes the major part of the lattice thermal conductivity, the

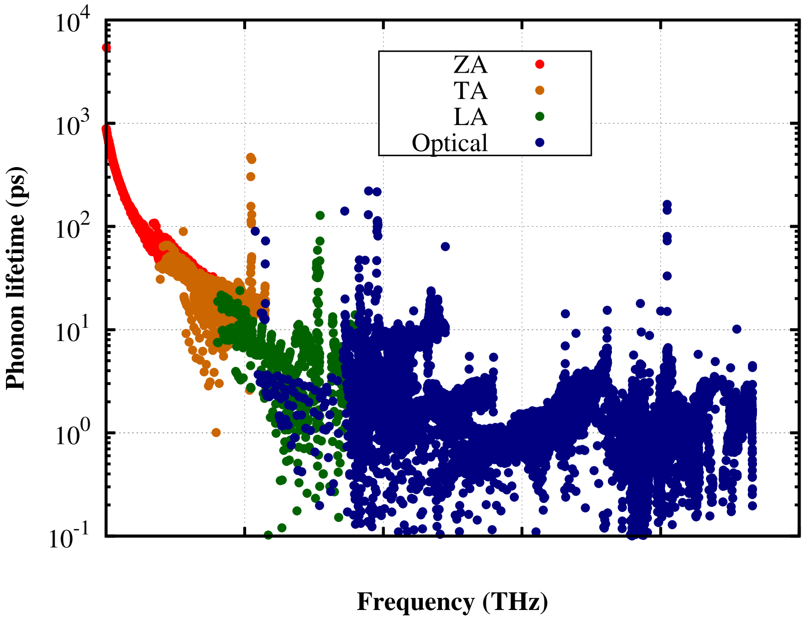

Figure 7.5: Phonon relaxation time (τ) as a function frequency at 300K for the monolayer BC_2N.

phonon group velocity is not only the factor leading to large lattice thermal conductivity.

7.3.4 Phonon lifetime

To understand the significant difference in the contribution of each phonon mode to κ_l, we analyze the phonon lifetimes (τ_λ) of each phonon mode as shown in Fig. 7.5. The phonon lifetimes are calculated using the Matthiessen rule expressed as[62]: $1/\tau_\lambda = 1/\tau_\lambda^{3ph} + 1/\tau_\lambda^{boundary} + 1/\tau_\lambda^{iso}$. The $1/\tau_\lambda$ is the total phonon scattering rate, the $1/\tau_\lambda^{3ph}$ is the three phonons scattering rate, the $1/\tau_\lambda^{boundary}$ is boundary scattering rate, and the $1/\tau_\lambda^{iso}$ is isotopic impurity scattering rate. All scattering processes must satisfy the energy and momentum conservation, $\omega_\lambda \pm \omega_{\lambda'} = \omega_{\lambda''}$ and $q \pm q' = q'' + G$, where G is the reciprocal lattice vector, the G value is zero for Normal processes and exists for the Umklapp processes. Among the phonon lifetime values, the ZA mode phonons have significantly larger lifetimes than other mode phonons. Monolayer BC_2N is one atom thick plane similar to graphene, and the out-of-plane symmetry exists which restricts scattering of the ZA mode phonons with other mode phonons and only allow even number ZA mode phonons scattering-processes (ZA+ZA ↔ LA/TA and ZA + LA/TA ↔ ZA). Therefore, the ZA mode phonons are contributed quite a large contribution to the total κ_l.

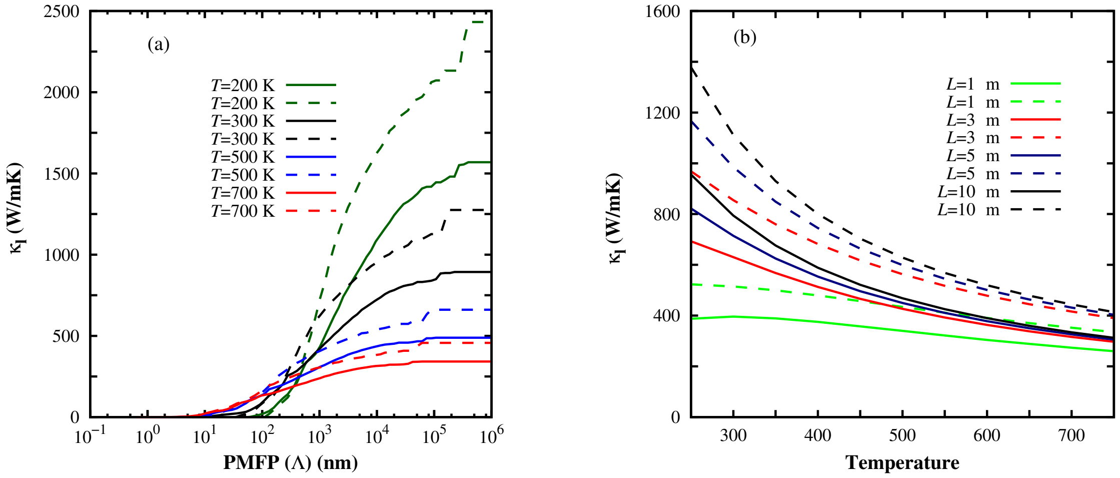

Figure 7.6: (a) Lattice thermal conductivity as a function of phonon mean free path (PMFP)(Λ) at different temperatures, and (b) lattice thermal conductivity as a function of temperature at different sample sizes. Solid lines represent the armchair direction, and dash lines represent the zigzag direction.

7.3.5 Lattice thermal conductivity as a function of the size

Phonon means free paths (PMFPs, Λ) are become shorten when we go from monocrystalline to the polycrystalline material because the phonons are scattered with grain boundary in the polycrystalline material. When the grain size (L_g) is larger than PMFPs ($\Lambda \ll L_g$), the dominant scattering will be phonon-phonon scattering, and phonon transport inside the grain will be diffusive. However, when the grain-size is smaller than PMFPs ($L_g \ll \Lambda$), the dominant scattering will be phonon-boundary scattering, and the phonon transport inside the grain will be ballistic. To check the consistency of our monocrystalline results with experimental polycrystalline results, we must analyze κ_l as a function of PMFPs to get a more extensive picture of phonon thermal transport. The κ_l along zigzag and armchair directions as a function of PMFP at different temperatures is plotted in Fig. 7.6(a). All values of PMFP are greater than 10^5 nm at room temperature and very large compared to other two-dimensional materials except graphene and *h*-BN. The κ_l may reduce in the polycrystalline BC2N sample with grain sizes range from 10^4 nm to 10^5 nm.

The lattice thermal conductivity of monolayer BC_2N with different sample sizes L=1μm, 3μm, 5μm, and 10μm as a function of temperature is shown in Fig. 7.6(b). The κ_l is strongly affected by sample size, the κ_l for the BC_2N sheet with L=1μm along the armchair and zigzag directions are 396.29 W/mK and 514.75 W/mK, respectively. The κ_l along the zigzag direction is more reduced than along armchair direction because long wavelength (ZA mode) phonons, which have the largest relative contribution to κ_l along zigzag than armchair direction, are suppressed. When the sample size decreases, the κ_l is reduced, and temperature-dependence is weakened because the phonon-boundary scattering is dominant from three-phonon scattering.

7.3.6 Electronic thermal transport properties

We now focus our attention on the electronic thermal transport properties of the monolayer BC_2N. We have obtained electronic transport properties using Boltzmann transport theory under constant relaxation time. The precise value of the electronic relaxation time (τ_e) can only be estimated from experiments, but there is no experimental data available for monolayer BC_2N. So, scaled electrical conductivity (σ/τ_e), electronic thermal conductivity (κ_e/τ_e), and Seebeck coefficient as a function of chemical potential (μ) are shown in Fig. 7.7 for the temperature range 300-700 K. The electronic transport properties are dramatical change with mu, which indicates that an optimal carrier concentration is required for the high electronic transport properties. The σ/τ_e and κ_e/τ_e increase with increasing temperature near to the Fermi level (Fermi level is set at 0 eV), they become independent of temperature away from the Fermi level. Similar behavior is observed in graphene. The rigid band approximation is used to check the effect of doping on the electronic transport properties, which is a reasonable approximation for the small doping. The positive and negative chemical potentials (shown in Fig. 7.7) represent the *n*-type and *p*-type dopants, respectively. As the Fermi level move into the conduction band (*n*-type doping) or valence band (*p*-type doping), the σ/τ_e and κ_e/τ_e are increased because number of charge carriers (n) are increased. The Seebeck coefficient along the armchair and zigzag directions are almost the same and isotropic. It decreases with increasing temperature due to the bipolar effect. The Seebeck coefficient has two peaks around Fermi level, and p-type Seebeck coefficient at 300 K is 2644 μVK which is slightly higher than the n-type. When we go away from the Fermi level the charge carriers increase, the Seebeck coefficient values decrease because it is inversely proportional $n^{2/3}$[108].

7.4 Summary

Phononic and electronic transport properties have been investigated using first principle calculations coupled with the Boltzmann transport equation. Monolayer BC2N has very high elastic constants, and it has a reflection symmetry, which prevents the scattering of ZA phonons with other modes phonons. Therefore, we have predicted very large values of lattice thermal conductivity (κ_l) along the armchair and zigzag directions at room-temperature. The κ_l along the armchair and zigzag directions are exhibited anisotropy, and the anisotropy value is 1.43.

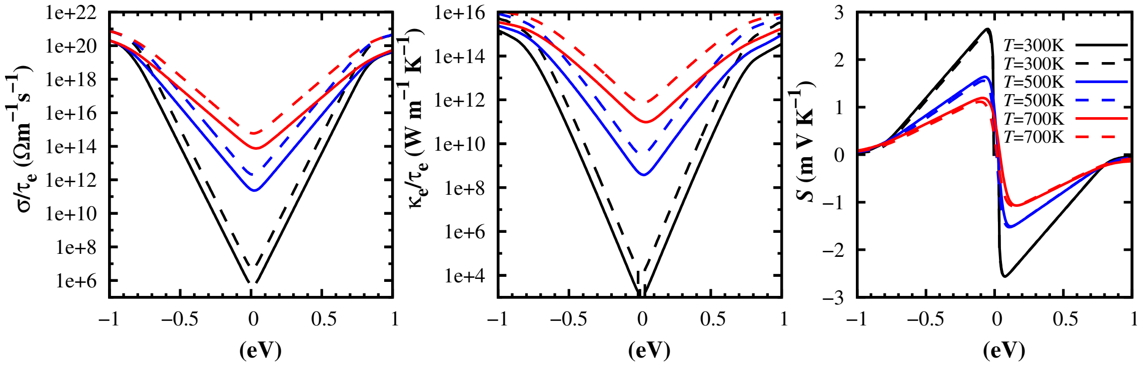

Figure 7.7: Scaled Electrical (σ/τ) and electronic thermal (κ_e/τ) conductivities, and Seebeck coefficients of the monolayer BC_2N as a function of chemical potential along the zigzag (solid line) and armchair directions (dash line) at 300K, 500K, and 700K.

The effect of size on the κ_l is also discussed, and it is found that the κ_l at room-temperature is reduced 2.25 and 2.47 times along armchair and zigzag directions, respectively, when the sample size is taken 1μm. The reduction in κ_l at small sample size is due to the increased in phonon boundary scattering. The electronic transport properties are also studied, and we found very high electronic thermal conductivity and Seebeck coefficient. Monolayer BC2N can be a promising material in thermal management because of the high thermal conductivities.

Chapter 8

Conclusions and future research directions

8.1 Conclusions

The primary objective of this thesis is to predict accurate lattice thermal conductivity of the two-dimensional materials which is important for a broad spectrum of applications, such as high-performance thermoelectric devices, thermal barrier coatings, thermal medical therapies, and thermal management of the nanoelectronics. The performances and the advancements in the nano-devices depend on the thermal transport in their constituent materials. However, the thermal transport in the two-dimensional materials alters drastically as compared to the bulk. Therefore, the fundamental understanding of phonon thermal transport in two-dimensional materials would be useful to tailor their thermal properties, according to the utilization.

In this thesis, phonon thermal transport in two-dimensional was investigated using the density functional theory combined with an iterative solution to the Boltzmann transport equation. The precise understanding of each phonon mode is obtained by calculating the phonon dispersion and phonon scattering rate of each phonon mode separately. Such an understanding is essential in the ability to engineer materials with craved thermal conductivity. The theoretical backgroung to calculate the lattice thermal conductivity is explained in Chapter 2.

In Chapter 3, we explored structural, electronic, thermoelectric, and phonon transport properties of two-dimensional monochalcogenides (SnSe, SnS, GeSe, and GeS) using density functional theory and semiclassical Boltzmann transport theory for electrons and phonons. To check the vibrational stability of these monolayers, we performed phonon dispersions calculations. The Seebeck coefficients of these monolayers become twice as compared to their bulk analogs. Lattice thermal conductivities of these monolayers were very low as compared to other two-dimensional materials. Due to large Seebeck coefficients and low lattice thermal conductivities we propose that these materials are very good thermoelectric materials.

In Chapter 4, we systematically investigated lattice thermal conductivity and carrier mobility of the SnX_2 (X: S, Se). Ultra-Low lattice thermal conductivities were found in SnS_2 (6.41 W/mK) and $SnSe_2$ (3.82 W/mK) at room temperature. We also calculated the phonon related properties like phonon spectra, phonon group velocity, Debye temperature and Grüneisen parameter. Effect of size on the lattice thermal is explored in order to design nano thermoelectric devices. The contribution toward total lattice thermal conductivity of the acoustic and optical mode was calculated. The phonon-limited carrier mobility was evaluated for the monolayer SnX_2 at room temperature and it was found that monolayer SnS_2 and $SnSe_2$ had high electronic mobilities of 756.60 cm^2 V^{-1} s^{-1} and 462.61 cm^2 V^{-1} s^{-1}. Due to ultra-low lattice thermal conductivities coupled with high carrier mobility, these materials can be exploited for thermoelectric applications.

In Chapter 5, we presented a comparative study of lattice thermal conductivity and phonon transport properties of the semiconducting monolayers InX (X=S, Se, Te). The predicted lattice thermal conductivities at room temperature are 56.45 W/mK, 44.43 W/mK and 33.05 W/mK for the monolayer InS, InSe and InTe, respectively. We also investigated the effect of non-analytical corrections on the phonon spectra and lattice thermal conductivity, and found that the longitudinal optical (LO) and transverse optical (TO) branches was split near the Γ-point and lattice thermal conductivities are increased for these monolayers. To understand the lattice thermal conductivity trend among these monolayers, we analyzed the phonon group velocity, phonon-phonon scattering rate, Debye temperature, and phonon anharmonicity. Size-dependent lattice thermal conductivity is also calculated and found a very large representative mean free path is indicating that nanostructuring can effectively reduce the lattice thermal conductivity. The relative contribution of the phonon modes to the lattice thermal conductivity fully quantify by our calculations and predicted that the longitudinal acoustic branch was the main contributor to the lattice thermal conductivity. Due to the low lattice thermal conductivities of these monolayers, they can be useful in the nanoscale thermoelectric devices.

In Chapter 6, we studied the effect of strain on the phonon thermal transport properties of the two-dimensional 2H-$MoTe_2$. The strain is a handy and useful tool to enhance the performance of the semiconducting devices. It can tune electronic, optical, and thermoelectric properties. However, the effect of tensile strain on the phonon thermal transport of two-dimensional materials is unpredictable because the flexural acoustic (ZA) mode becomes harder and transverse acoustic (TA) and longitudinal acoustic (LA) modes become softened. We found that the lattice thermal conductivity was reduced approximately 2.5 times at 8% tensile strain for the two-dimensional 2H-$MoTe_2$ contrary to graphene, germanene, silicene, germanene, and

Penta-SiC_2. The reduction in lattice thermal conductivity attributes to the reduction in the phonon group velocity, the phonon heat capacity, and the phonon scattering time. We also evaluated the contribution of each mode to the lattice thermal conductivity. The ZA mode contribution decreased while the TA/LA modes contributions increased under tensile strain. These results highlighted that tensile strain is a key parameter to tune the lattice thermal conductivity and other phonon thermal transport properties of the two-dimensional 2H-MoTe_2.

In Chapter 7, we predicted an ultra-high and anisotropic lattice thermal conductivity in the monolayer BC_2N. The predicted values of lattice thermal conductivity at room-temperature are 893.90 W/mK and 1275.79 W/mK along armchair and zigzag directions, respectively. These values are probably the highest that have ever been reported for the two-dimensional semiconducting materials, which we attributed to the high vibrational frequencies, large phonon group velocities, long phonon lifetime, low phonon anharmonicity, and strong bonding in monolayer BC_2N. We also calculate the electrical and electronic thermal conductivities, which are also very high. Monolayer BC_2N can be used for thermal management in the nanoelectronic devices because of the ultra-high lattice thermal conductivity.

8.2 Future research directions

The lattice dynamics method has the main advantage of giving the entire phonon properties and relating these directly to the lattice thermal conductivity. The accurate modeling of phonon thermal transport across lateral and vertical heterostructures using lattice dynamic based methods should be the subject of future work. In heterostructure, the properties can be tuned by changing the stacking orientation and interlayer distance, which opens the door to the new possibilities and novel applications. The combination of the semiconducting monolayers can merge the excellent thermoelectric properties with ultra-low lattice thermal conductivity and high electrical conductivity. We expect that lattice thermal conductivity is reduced in the heterostructure because the interface suppress the phonons and we will search type II band structure alignment heterostructure to increase electrical conductivity. I have proposed the following topics to support my prospective research:

1. InX/GaX (X=S,Se, Te) heterobilayer as potential thermoelectric material
2. Thermoelectric properties of the InAs/InSb heterostructure: a first principles study
3. Thermoelectric properties of the HfSe_3/ZrSe_3 heterostructure
4. Phonon and thermoelectric properties of TiS_3/ZrSe_3 heterostructure

References

[1] Keivan Esfarjani, Gang Chen, and Harold T. Stokes. Heat transport in silicon from first-principles calculations. *Phys. Rev. B*, 84(8):085204, 2011.

[2] Eric S. Toberer, Lauryn L. Baranowski, and Chris Dames. Advances in Thermal Conductivity. *Annu. Rev. Mater. Res.*, 42(1):179–209, 2012.

[3] Yangyu Guo and Moran Wang. Heat transport in two-dimensional materials by directly solving the phonon Boltzmann equation under Callaway's dual relaxation model. *Phys. Rev. B*, 96(13):134312, 2017.

[4] Nuo Yang, Xiangfan Xu, Gang Zhang, and Baowen Li. Thermal transport in nanostructures. *AIP Advances*, 2(4):041410, 2012.

[5] William J. Evans, Lin Hu, and Pawel Keblinski. Thermal conductivity of graphene ribbons from equilibrium molecular dynamics: Effect of ribbon width, edge roughness, and hydrogen termination. *Appl. Phys. Lett.*, 96(20):203112, 2010.

[6] Zhixin Guo, Dier Zhang, and Xin-Gao Gong. Thermal conductivity of graphene nanoribbons. *Appl. Phys. Lett.*, 95(16):163103, 2009.

[7] Alexander A. Balandin, Suchismita Ghosh, Wenzhong Bao, Irene Calizo, Desalegne Teweldebrhan, Feng Miao, and Chun Ning Lau. Superior Thermal Conductivity of Single-Layer Graphene. *Nano Lett.*, 8(3):902–907, 2008.

[8] H. K. Liu, Y. Lin, and S. N. Luo. Thermal Conductivity of Graphene in Corbino Membrane Geometry. *J. Phys. Chem. C*, 4:24797–24802, 2014.

[9] Weiwei Cai, Arden L. Moore, Yanwu Zhu, Xuesong Li, Shanshan Chen, Li Shi, and Rodney S. Ruoff. Thermal Transport in Suspended and Supported Monolayer Graphene Grown by Chemical Vapor Deposition. *Nano Lett.*, 10(5):1645–1651, 2010.

[10] Shanshan Chen, Qingzhi Wu, Columbia Mishra, Junyong Kang, Hengji Zhang, Kyeongjae Cho, Weiwei Cai, Alexander A. Balandin, and Rodney S. Ruoff. Thermal conductivity of isotopically modified graphene. *Nat. Mater.*, 11(3):203–207, 2012.

[11] Hongyang Li, Hao Ying, Xiangping Chen, Denis L. Nika, Alexandr I. Cocemasov, Weiwei Cai, Alexander A. Balandin, and Shanshan Chen. Thermal conductivity of twisted bilayer graphene. *Nanoscale*, 6(22):13402–13408, 2014.

[12] D. L. Nika, E. P. Pokatilov, A. S. Askerov, and A. A. Balandin. Phonon thermal conduction in graphene: Role of Umklapp and edge roughness scattering. *Phys. Rev. B*, 79(15):155413, 2009.

[13] L. Lindsay, D. A. Broido, and Natalio Mingo. Flexural phonons and thermal transport in graphene. *Phys. Rev. B*, 82(11):115427, September 2010.

[14] Dhruv Singh, Jayathi Y. Murthy, and Timothy S. Fisher. Mechanism of thermal conductivity reduction in few-layer graphene. *J. Appl. Phys.*, 110(4):044317, 2011.

[15] Giorgia Fugallo, Andrea Cepellotti, Lorenzo Paulatto, Michele Lazzeri, Nicola Marzari, and Francesco Mauri. Thermal Conductivity of Graphene and Graphite: Collective Excitations and Mean Free Paths. *Nano Lett.*, 14(11):6109–6114, November 2014.

[16] L. Lindsay, Wu Li, Jes??s Carrete, Natalio Mingo, D. A. Broido, and T. L. Reinecke. Phonon thermal transport in strained and unstrained graphene from first principles. *Phys. Rev. B*, 89(15):155426, April 2014.

[17] Xiaokun Gu and Ronggui Yang. First-principles prediction of phononic thermal conductivity of silicene: A comparison with graphene. *Journal of Applied Physics*, 117(2):025102, 2015.

[18] Xiaobo Li, Kurt Maute, Martin L. Dunn, and Ronggui Yang. Strain effects on the thermal conductivity of nanostructures. *Phys. Rev. B*, 81(24):245318, 2010.

[19] H. K. Liu, Y. Lin, and S. N. Luo. Grain Boundary Energy and Grain Size Dependences of Thermal Conductivity of Polycrystalline Graphene. *J. Phys. Chem. C*, 118(42):24797–24802, 2014.

[20] Ziqian Wang, Rongguo Xie, Cong Tinh Bui, Dan Liu, Xiaoxi Ni, Baowen Li, and John T. L. Thong. Thermal Transport in Suspended and Supported Few-Layer Graphene. *Nano Lett.*, 11(1):113–118, 2011.

[21] Bo Peng, Hao Zhang, Hezhu Shao, Yuanfeng Xu, Rongjun Zhang, Hongliang Lu, David Wei Zhang, and Heyuan Zhu. First-Principles Prediction of Ultralow Lattice Thermal Conductivity of Dumbbell Silicene: A Comparison with Low-Buckled Silicene. *ACS Appl. Mater. Interfaces*, 8(32):20977–20985, August 2016.

[22] Han Xie, Tao Ouyang, Éric Germaneau, Guangzhao Qin, Ming Hu, and Hua Bao. Large tunability of lattice thermal conductivity of monolayer silicene via mechanical strain. *Phys. Rev. B*, 93(7):075404, February 2016.

[23] Y. D. Kuang, L. Lindsay, S. Q. Shi, and G. P. Zheng. Tensile strains give rise to strong size effects for thermal conductivities of silicene, germanene and stanene. *Nanoscale*, 8(6):3760–3767, February 2016.

[24] Ming Hu, Xiaoliang Zhang, and Dimos Poulikakos. Anomalous thermal response of silicene to uniaxial stretching. *Phys. Rev. B*, 87(19):195417, 2013.

[25] Qing-Xiang Pei, Yong-Wei Zhang, Zhen-Dong Sha, and Vivek B Shenoy. Tuning the thermal conductivity of silicene with tensile strain and isotopic doping: A molecular dynamics study. *J. Appl. Phys.*, 114(3):033526, 2013.

[26] Hai-peng Li and Rui-qin Zhang. Vacancy-defect–induced diminution of thermal conductivity in silicene. *EPL*, 99(3):36001, 2012.

[27] Lin Wang and Huai Sun. Thermal conductivity of silicon and carbon hybrid monolayers: a molecular dynamics study. *J. molec. model.*, 18(11):4811–4818, 2012.

[28] Bo Peng, Hao Zhang, Hezhu Shao, Yuanfeng Xu, Gang Ni, Rongjun Zhang, and Heyuan Zhu. Phonon transport properties of two-dimensional group-IV materials from ab initio calculations. *Phys. Rev. B*, 94(24):245420, December 2016.

[29] G. A. Slack. Nonmetallic crystals with high thermal conductivity. *J. Phys. Chem. Solids*, 34(2):321–335, January 1973.

[30] Satyaprakash Sahoo, Anand P. S. Gaur, Majid Ahmadi, Maxime J.-F. Guinel, and Ram S. Katiyar. Temperature-Dependent Raman Studies and Thermal Conductivity of Few-Layer MoS2. *J. Phys. Chem. C*, 117(17):9042–9047, 2013.

[31] Rusen Yan, Jeffrey R. Simpson, Simone Bertolazzi, Jacopo Brivio, Michael Watson, Xufei Wu, Andras Kis, Tengfei Luo, Angela R. Hight Walker, and Huili Grace Xing. Thermal Conductivity of Monolayer Molybdenum Disulfide Obtained from Temperature-Dependent Raman Spectroscopy. *ACS Nano*, 8(1):986–993, 2014.

[32] Insun Jo, Michael Thompson Pettes, Eric Ou, Wei Wu, and Li Shi. Basal-plane thermal conductivity of few-layer molybdenum disulfide. *Appl. Phys. Lett.*, 104(20):201902, 2014.

[33] Andrzej Taube, Jarosław Judek, Anna Łapińska, and Mariusz Zdrojek. Temperature-Dependent Thermal Properties of Supported MoS2 Monolayers. *ACS Appl. Mater. Interfaces*, 7(9):5061–5065, 2015.

[34] Appala Naidu Gandi and Udo Schwingenschlögl. Thermal conductivity of bulk and monolayer mos2. *EPL*, 113(3):36002, 2016.

[35] Bo Peng, Hao Zhang, Hezhu Shao, Yuchen Xu, Xiangchao Zhang, and Heyuan Zhu. Thermal conductivity of monolayer MoS_2, $MoSe_2$, and WS_2: interplay of mass effect, interatomic bonding and anharmonicity. *RSC Advances*, 6(7):5767–5773, January 2016.

[36] Xiaokun Gu and Ronggui Yang. Phonon transport in single-layer transition metal dichalcogenides: A first-principles study. *Appl. Phys. Lett.*, 105(13):131903, September 2014.

[37] Jin-Wu Jiang, Harold S. Park, and Timon Rabczuk. Molecular dynamics simulations of single-layer molybdenum disulphide (MoS2): Stillinger-Weber parametrization, mechanical properties, and thermal conductivity. *J. Appl. Phys.*, 114(6):064307, 2013.

[38] Xiangjun Liu, Gang Zhang, Qing-Xiang Pei, and Yong-Wei Zhang. Phonon thermal conductivity of monolayer MoS2 sheet and nanoribbons. *Appl. Phys. Lett.*, 103(13):133113, 2013.

[39] Chris Muratore, Vikas Varshney, Jamie J. Gengler, Jianjun Hu, John E. Bultman, Ajit K. Roy, Barry L. Farmer, and Andrey A. Voevodin. Thermal anisotropy in nano-crystalline MoS2 thin films. *Phys. Chem. Chem. Phys.*, 16(3):1008–1014, 2013.

[40] Wu Li, J Carrete, and Natalio Mingo. Thermal conductivity and phonon linewidths of monolayer mos2 from first principles. *Appl. Phys. Lett.*, 103(25):253103, 2013.

[41] Jian He and Terry M. Tritt. Advances in thermoelectric materials research: Looking back and moving forward. *Science*, 357(6358):eaak9997, September 2017.

[42] Saikat Mukhopadhyay, David S. Parker, Brian C. Sales, Alexander A. Puretzky, Michael A. McGuire, and Lucas Lindsay. Two-channel model for ultralow thermal conductivity of crystalline Tl3VSe4. *Science*, 360(6396):1455–1458, 2018.

[43] Terry M. Tritt. Thermoelectrics Run Hot and Cold. *Science*, 272(5266):1276–1277, May 1996.

[44] G. Jeffrey Snyder, Mogens Christensen, Eiji Nishibori, Thierry Caillat, and Bo Brummerstedt Iversen. Disordered zinc in Zn_4Sb_3 with phonon-glass and electron-crystal thermoelectric properties. *Nat. Mater.*, 3:458–463, 2004.

[45] Kengo Kishimoto and Tsuyoshi Koyanagi. Preparation of sintered degenerate n-type PbTe with a small grain size and its thermoelectric properties. *J. Appl. Phys.*, 92:2544, 2002.

[46] Xinfeng Tang, Lidong Chen, Takashi Goto, and Toshio Hirai. Effects of Ce filling fraction and Fe content on the thermoelectric properties of Co-rich $Ce_yFe_xCo_{4-x}Sb_{12}$. *J. Mater. Res.*, 16:837–843, 2001.

[47] G. S. Nolas, M. Kaeser, R. T. Littleton, and T. M. Tritt. High figure of merit in partially filled ytterbium skutterudite materials. *Appl. Phys. Lett.*, 77(12):1855–1857, 2000.

[48] L. D. Hicks and M. S. Dresselhaus. Thermoelectric figure of merit of a one-dimensional conductor. *Phys. Rev. B*, 47:16631–16634, Jun 1993.

[49] Nicola Bonini, Jivtesh Garg, and Nicola Marzari. Acoustic Phonon Lifetimes and Thermal Transport in Free-Standing and Strained Graphene. *Nano Lett.*, 12(6):2673–2678, June 2012.

[50] Shasha Li and Yue Chen. Thermal transport and anharmonic phonons in strained monolayer hexagonal boron nitride. *Sci. Rep.*, 7:43956, March 2017.

[51] Ai-Xia Zhang, Jiang-Tao Liu, San-Dong Guo, and Hui-Chao Li. Strain effects on phonon transport in antimonene investigated using a first-principles study. *Phys. Chem. Chem. Phys.*, 19(22):14520–14526, 2017.

[52] Huake Liu, Guangzhao Qin, Yuan Lin, and Ming Hu. Disparate Strain Dependent Thermal Conductivity of Two-dimensional Penta-Structures. *Nano Lett.*, 16(6):3831–3842, June 2016.

[53] Youdi Kuang, Lucas Lindsay, and Baoling Huang. Unusual Enhancement in Intrinsic Thermal Conductivity of Multilayer Graphene by Tensile Strains. *Nano Lett.*, 15(9):6121–6127, September 2015.

[54] Liyan Zhu, Tingting Zhang, Ziming Sun, Jianhua Li, Guibin Chen, and Shengyuan A. Yang. Thermal conductivity of biaxial-strained MoS 2 : sensitive strain dependence and size-dependent reduction rate. *Nanotechnology*, 26(46):465707, 2015.

[55] Siegfried Bauer. Flexible electronics: Sophisticated skin. *Nat. Mater.*, 12(10):871–872, October 2013.

[56] Houfu Song, Jiaman Liu, Bilu Liu, Junqiao Wu, Hui-Ming Cheng, and Feiyu Kang. Two-Dimensional Materials for Thermal Management Applications. *Joule*, 2(3):442–463, March 2018.

[57] Eric Pop, Vikas Varshney, and Ajit K. Roy. Thermal properties of graphene: Fundamentals and applications. *MRS Bulletin*, 37(12):1273–1281, December 2012.

[58] H. F. Hamann, A. Weger, J. A. Lacey, Z. Hu, P. Bose, E. Cohen, and J. Wakil. Hotspot-Limited Microprocessors: Direct Temperature and Power Distribution Measurements. *IEEE J. Solid-State Circuits*, 42(1):56–65, January 2007.

[59] Alexander A. Balandin. Thermal properties of graphene and nanostructured carbon materials. *Nat. Mater.*, 10(8):569–581, 2011.

[60] Giorgia Fugallo, Michele Lazzeri, Lorenzo Paulatto, and Francesco Mauri. Ab initio variational approach for evaluating lattice thermal conductivity. *Phys. Rev. B*, 88(4):045430, July 2013.

[61] R. Peierls. On the Kinetic Theory of Thermal Conduction in Crystals. In *Selected Scientific Papers of Sir Rudolf Peierls*, volume Volume 19 of *World Scientific Series in 20th Century Physics*, pages 15–48. CO-PUBLISHED BY IMPERIAL COLLEGE PRESS AND WORLD SCIENTIFIC PUBLISHING CO., April 1997.

[62] John M Ziman. *Electrons and phonons: the theory of transport phenomena in solids*. Oxford university press, 1960.

[63] Terry M. Tritt, editor. *Thermal Conductivity: Theory, Properties, and Applications*. Physics of Solids and Liquids. Springer US, 2004.

[64] Gyaneshwar P Srivastava. *The physics of phonons*. CRC press, 1990.

[65] Max Born and Kun Huang. *Dynamical Theory of Crystal Lattices*. Oxford university press, 1998.

[66] Neil W. Ashcroft and N. David Mermin. *Solid State Physics*. Cengage Learning, 2011.

[67] A. A. Maradudin and A. E. Fein. Scattering of Neutrons by an Anharmonic Crystal. *Phys. Rev.*, 128(6):2589–2608, December 1962.

[68] Martin T. Dove and Martin T. Dove. *Introduction to Lattice Dynamics*. Cambridge University Press, October 1993.

[69] Ankita Katre. *Modelling Thermal Transport in Nanostructured Materials*. PhD thesis, February 2016.

[70] L. Lindsay, D. A. Broido, and T. L. Reinecke. Phonon-isotope scattering and thermal conductivity in materials with a large isotope effect: A first-principles study. *Phys. Rev. B*, 88(14):144306, October 2013.

[71] L. Lindsay, D. A. Broido, and T. L. Reinecke. Thermal Conductivity and Large Isotope Effect in GaN from First Principles. *Phys. Rev. Lett.*, 109(9):095901, August 2012.

[72] A. J. H. McGaughey, M. I. Hussein, E. S. Landry, M. Kaviany, and G. M. Hulbert. Phonon band structure and thermal transport correlation in a layered diatomic crystal. *Phys. Rev. B*, 74(10):104304, September 2006.

[73] Lorenzo Paulatto, Francesco Mauri, and Michele Lazzeri. Anharmonic properties from a generalized third-order ab initio approach: Theory and applications to graphite and graphene. *Phys. Rev. B*, 87(21):214303, June 2013.

[74] R. A. Cowley. Anharmonic crystals. *Rep. Prog. Phys.*, 31(1):123, 1968.

[75] Matteo Calandra, Michele Lazzeri, and Francesco Mauri. Anharmonic and non-adiabatic effects in MgB2: Implications for the isotope effect and interpretation of Raman spectra. *Physica C: Superconductivity*, 456(1):38–44, June 2007.

[76] M. Omini and A. Sparavigna. Effect of phonon scattering by isotope impurities on the thermal conductivity of dielectric solids. *Physica B: Condensed Matter*, 233(2):230–240, May 1997.

[77] M. Omini and A. Sparavigna. Heat transport in dielectric solids with diamond structure. *Nuovo Cimento D Serie*, 19:1537, October 1997.

[78] Giorgia Fugallo, Andrea Cepellotti, Lorenzo Paulatto, Michele Lazzeri, Nicola Marzari, and Francesco Mauri. Thermal Conductivity of Graphene and Graphite: Collective Excitations and Mean Free Paths. *Nano Lett.*, 14:6109–6114, November 2014.

[79] Erwin Schrödinger. Quantisierung als eigenwertproblem. *Annalen der physik*, 385(13):437–490, 1926.

[80] Robert G. Parr and Yang Weitao. *Density-Functional Theory of Atoms and Molecules*. Oxford University Press, May 1994.

[81] Reiner M. Dreizler and Eberhard K. U. Gross. *Density Functional Theory: An Approach to the Quantum Many-Body Problem*. Springer-Verlag, Berlin Heidelberg, 1990.

[82] Feliciano Giustino. *Materials Modelling Using Density Functional Theory: Properties and Predictions*. Oxford University Press, Oxford, New York, May 2014.

[83] Richard M. Martin and Richard Milton Martin. *Electronic Structure: Basic Theory and Practical Methods*. Cambridge University Press, April 2004.

[84] D. M. Ceperley and B. J. Alder. Ground State of the Electron Gas by a Stochastic Method. *Phys. Rev. Lett.*, 45(7):566–569, August 1980.

[85] W. Kohn. Nobel Lecture: Electronic structure of matter—wave functions and density functionals. *Rev. Mod. Phys.*, 71(5):1253–1266, October 1999.

[86] R. O. Jones and O. Gunnarsson. The density functional formalism, its applications and prospects. *Rev. Mod. Phys.*, 61(3):689–746, July 1989.

[87] J. Hafner. Atomic-scale computational materials science. *Acta Materialia*, 48(1):71–92, January 2000.

[88] M. Born and R. Oppenheimer. Zur Quantentheorie der Molekeln. 389(20):457–484, January 1927.

[89] D. R. Hartree. The Wave Mechanics of an Atom with a Non-Coulomb Central Field. Part I. Theory and Methods. *Math. Proc. Camb. Philos. Soc.*, 24(1):89–110, January 1928.

[90] P. Hohenberg and W. Kohn. Inhomogeneous Electron Gas. *Phys. Rev.*, 136(3B):B864–B871, November 1964.

[91] W. Kohn and L. J. Sham. Self-Consistent Equations Including Exchange and Correlation Effects. *Phys. Rev.*, 140(4A):A1133–A1138, November 1965.

[92] J. P. Perdew and Alex Zunger. Self-interaction correction to density-functional approximations for many-electron systems. *Phys. Rev. B*, 23(10):5048–5079, May 1981.

[93] John P. Perdew, Kieron Burke, and Matthias Ernzerhof. Generalized Gradient Approximation Made Simple. *Phys. Rev. Lett.*, 77(18):3865–3868, October 1996.

[94] John P. Perdew and Yue Wang. Accurate and simple analytic representation of the electron-gas correlation energy. *Phys. Rev. B*, 45(23):13244–13249, June 1992.

[95] John P. Perdew, Kieron Burke, and Matthias Ernzerhof. Generalized Gradient Approximation Made Simple. *Phys. Rev. Lett.*, 77(18):3865–3868, October 1996.

[96] David Vanderbilt. Soft self-consistent pseudopotentials in a generalized eigenvalue formalism. *Phys. Rev. B*, 41(11):7892–7895, April 1990.

[97] Kari Laasonen, Alfredo Pasquarello, Roberto Car, Changyol Lee, and David Vanderbilt. Car-Parrinello molecular dynamics with Vanderbilt ultrasoft pseudopotentials. *Phys. Rev. B*, 47(16):10142–10153, April 1993.

[98] DR Hamann, M Schlüter, and C Chiang. Norm-conserving pseudopotentials. *Physical Review Letters*, 43(20):1494, 1979.

[99] Warren E. Pickett. Pseudopotential methods in condensed matter applications. *Computer Physics Reports*, 9(3):115–197, April 1989.

[100] P. E. Blöchl. Projector augmented-wave method. *Phys. Rev. B*, 50(24):17953, December 1994.

[101] G. Kresse and D. Joubert. From ultrasoft pseudopotentials to the projector augmented-wave method. *Phys. Rev. B*, 59:1758–1775, Jan 1999.

[102] M. C. Payne, M. P. Teter, D. C. Allan, T. A. Arias, and J. D. Joannopoulos. Iterative minimization techniques for ab initio total-energy calculations: molecular dynamics and conjugate gradients. *Rev. Mod. Phys.*, 64:1045–1097, Oct 1992.

[103] G. Jeffrey Snyder and Eric S. Toberer. Complex thermoelectric materials. *Nat. Mater.*, 7:105–114, 2008.

[104] Bao Zhen Sun, Zuju Ma, Chao He, and Kechen Wu. Anisotropic thermoelectric properties of layered compounds in $\mathrm{Sn}X_2$ (X = S, Se): a promising thermoelectric material. *Phys. Chem. Chem. Phys.*, 17:29844–29853, 2015.

[105] Francis J. DiSalvo. Thermoelectric cooling and power generation. *Sci.*, 285(5428):703–706, 1999.

[106] Guangqian Ding, G Y Gao, and K L Yao. Examining the thermal conductivity of the half-heusler alloy TiNiSn by first-principles calculations. *J. Phys. D: Appl. Phys.*, 48:235302, 06 2015.

[107] Khuong P. Ong, David J. Singh, and Ping Wu. Analysis of the thermoelectric properties of n-type ZnO. *Phys. Rev. B*, 83:115110, Mar 2011.

[108] Hiromichi Ohta, SungWng Kim, Yoriko Mune, Teruyasu Mizoguchi, Takashi Nomura, Shingo Ohta, Takashi Nomura, Yuichi Ikuhara, Masahiro Hirano, Hideo Hosono, and Kunihito Koumoto. Giant thermoelectric Seebeck coefficient of a two-dimensional electron gas in $SrTiO_3$. *Nat. Mater.*, 6:129–134, 2007.

[109] A. M. Ibrahiman and D. A. Thompson. Thermoelectric properties of BiSb alloys. *Mater. Chem. Phys.*, 12:29–36, 1985.

[110] B. C. Sales, D. Mandrus, B. C. Chakoumakos, V. Keppens, and J. R. Thompson. Filled skutterudite antimonides: Electron crystals and phonon glasses. *Phys. Rev. B*, 56:15081–15089, Dec 1997.

[111] G. S. Nolas, J. L. Cohn, G. A. Slack, and S. B. Schujman. Semiconducting Ge clathrates: Promising candidates for thermoelectric applications. *Appl. Phys. Lett.*, 73(2):178–180, 1998.

[112] Takeyuki Sekimoto, Ken Kurosaki, Hiroaki Muta, and Shinsuke Yamanaka. High-Thermoelectric figure of merit realized in p-type half-heusler compounds: $ZrCoSn_xSb_{1-x}$. *Jap. J. Appl. Phys.*, 46:L673–L675, 7 2007.

[113] I. I. Singh, D. J.; Mazin. Calculated thermoelectric properties of La-filled skutterudites. *Phys. Rev. B*, 56:R1650–R1653, 7 1997.

[114] Joseph R. Sootsman, Duck Young Chung, and Mercouri G. Kanatzidis. New and old concepts in thermoelectric materials. *Ang. Chem. Inter. Edit.*, 48:8616–8639, 2009.

[115] Li Dong Zhao, Shih Han Lo, Yongsheng Zhang, Hui Sun, Gangjian Tan, Ctirad Uher, C. Wolverton, Vinayak P. Dravid, and Mercouri G. Kanatzidis. Ultralow thermal conductivity and high thermoelectric figure of merit in SnSe crystals. *Nature*, 508:373–377, 4 2014.

[116] Guangqian Ding, Guoying Gao, and Kailun Yao. High-efficient thermoelectric materials: The case of orthorhombic IV–VI compounds. *Sci. Rep.*, 5:9567, 6 2015.

[117] M. S. Dresselhaus, G. Chen, Ming Y. Tang, Ronggui Yang, Hohyun. Lee, Dehhi. Wang, Zhifeng Ren, J. P. Fleurial, and P. Gogna. New directions for low-dimensional thermoelectric materials. *Adv. Mater.*, 38:1043–1053, 2007.

[118] Jeannine R. Szczech, Jeremy M. Higgins, and Song Jin. Enhancement of the thermoelectric properties in nanoscale and nanostructured materials. *J. Mater. Chem.*, 21:4037, 2011.

[119] L. D. Hicks and M. S. Dresselhaus. Effect of quantum-well structures on the thermoelectric figure of merit. *Phys. Rev. B*, 47:12727–12731, May 1993.

[120] Ruixiang Fei, Alireza Faghaninia, Ryan Soklaski, Jia-An Yan, Cynthia Lo, and Li Yang. Enhanced thermoelectric efficiency via orthogonal electrical and thermal conductances in phosphorene. *Nano Lett.*, 14:6393–6399, 11 2014.

[121] Long Cheng, Huijun Liu, Xiaojian Tan, Jie Zhang, Jie Wei, Hongyan Lv, Jing Shi, and Xinfeng Tang. Thermoelectric properties of a monolayer bismuth. *J. Phys. Chem. C*, 118:904–910, 01 2014.

[122] Lun Li, Zhong Chen, Ying Hu, Xuewen Wang, Ting Zhang, Wei Chen, and Qiangbin Wang. Single-layer single-crystalline snse nanosheets. *J. Am. Chem. Soc.*, 135(4):1213–1216, January 2013.

[123] Jing Xia, Xuan-Ze Li, Xing Huang, Nannan Mao, Dan-Dan Zhu, Lei Wang, Hua Xu, and Xiang-Min Meng. Physical vapor deposition synthesis of two-dimensional orthorhombic SnS flakes with strong angle/temperature-dependent Raman responses. *Nanoscale*, 8(4):2063–2070, January 2016.

[124] Xufan Li, Ming-Wei Lin, Alexander A. Puretzky, Juan C. Idrobo, Cheng Ma, Miaofang Chi, Mina Yoon, Christopher M. Rouleau, Ivan I. Kravchenko, David B. Geohegan, and Kai Xiao. Controlled vapor phase growth of single crystalline, two-dimensional GaSe crystals with high photoresponse. *Sci. Rep.*, 4:5497, June 2014.

[125] Shengli Zhang, Ning Wang, Shangguo Liu, Shiping Huang, Wenhan Zhou, Bo Cai, Meiqiu Xie, Qun Yang, Xianping Chen, and Haibo Zeng. Two-dimensional GeS with tunable electronic properties via external electric field and strain. *Nanotechnology*, 27(27):274001, 2016.

[126] Guangzhao Qin, Zhenzhen Qin, Wu-Zhang Fang, Li-Chuan Zhang, Sheng-Ying Yue, Qing-Bo Yan, Ming Hu, and Gang Su. Diverse anisotropy of phonon transport in two-

dimensional group IV–VI compounds: A comparative study. *Nanoscale*, 8(21):11306–11319, May 2016.

[127] Li-Dong Zhao, Cheng Chang, Gangjian Tan, and Mercouri G. Kanatzidis. SnSe: a remarkable new thermoelectric material. *Energy Environ. Sci.*, 9(10):3044–3060, October 2016.

[128] Fancy Qian Wang, Shunhong Zhang, Jiabing Yu, and Qian Wang. Thermoelectric properties of single-layered SnSe sheet. *Nanoscale*, 7(38):15962–15970, September 2015.

[129] G. Kresse and J. Furthmüller. Efficient iterative schemes for *ab initio* total-energy calculations using a plane-wave basis set. *Phys. Rev. B*, 54:11169–11186, Oct 1996.

[130] Georg K.H. Madsen and David J. Singh. BoltzTraP. A code for calculating band-structure dependent quantities. *Comp. Phys. Commun.*, 175:67–71, 2006.

[131] John P. Perdew, Kieron Burke, and Matthias Ernzerhof. Generalized gradient approximation made simple. *Phys. Rev. Lett.*, 77:3865–3868, Oct 1996.

[132] Ji ří Klimeš, David R. Bowler, and Angelos Michaelides. Van der Waals density functionals applied to solids. *Phys. Rev. B*, 83:195131, May 2011.

[133] Wu Li, Jesus Carrete, Nebil A. Katcho, and Natalio Mingo. ShengBTE: A solver of the Boltzmann transport equation for phonons. *Comp. Phys. Commun.*, 185:1747–1758, 06 2014.

[134] Atsushi Togo, Fumiyasu Oba, and Isao Tanaka. First-principles calculations of the ferroelastic transition between rutile-type and $CaCl_2$-type SiO_2 at high pressures. *Phys. Rev. B*, 78:134106, Oct 2008.

[135] Wu Li, Lucas Lindsay, David A. Broido, Derek A. Stewart, and Natalio Mingo. Thermal conductivity of bulk and nanowire $mg_2si_xsn_{1-x}$ alloys from first principles. *Phys. Rev. B*, 86:174307, 2012.

[136] Wu Li, Natalio Mingo, Lucas Lindsay, David A. Broido, Derek A. Stewart, and Nebil A. Katcho. Thermal conductivity of diamond nanowires from first principles. *Phys. Rev. B*, 85:195436, 2012.

[137] Arunima K. Singh and Richard G. Hennig. Computational prediction of two-dimensional group-IV mono-chalcogenides. *Appl. Phys. Lett.*, 105(4):042103, 2014.

[138] Ruixiang Fei, Wenbin Li, Ju Li, and Li Yang. Giant piezoelectricity of monolayer group IV monochalcogenides: SnSe, SnS, GeSe, and GeS. *Appl. Phys. Lett.*, 107(17):173104, 2015.

[139] Yongqing Cai, Gang Zhang, and Yong-Wei Zhang. Polarity-Reversed Robust Carrier Mobility in Monolayer MoS2 Nanoribbons. *J. Am. Chem. Soc.*, 136(17):6269–6275, April 2014.

[140] Li-Chuan Zhang, Guangzhao Qin, Wu-Zhang Fang, Hui-Juan Cui, Qing-Rong Zheng, Qing-Bo Yan, and Gang Su. Tinselenidene: a Two-dimensional Auxetic Material with Ultralow Lattice Thermal Conductivity and Ultrahigh Hole Mobility. *Sci. Rep.*, 6:19830, February 2016.

[141] Zelin Jin, Quanwen Liao, Haisheng Fang, Zhichun Liu, Wei Liu, Zhidong Ding, Tengfei Luo, and Nuo Yang. A Revisit to High Thermoelectric Performance of Single-layer MoS2. *Scientific Reports*, 5:18342, December 2015.

[142] H. Y. Lv, W. J. Lu, D. F. Shao, H. Y. Lu, and Y. P. Sun. Strain-induced enhancement in the thermoelectric performance of a ZrS 2 monolayer. *Journal of Materials Chemistry C*, 4(20):4538–4545, 2016.

[143] J. Bardeen and W. Shockley. Deformation Potentials and Mobilities in Non-Polar Crystals. *Phys. Rev.*, 80(1):72–80, October 1950.

[144] Le Huang, Fugen Wu, and Jingbo Li. Structural anisotropy results in strain-tunable electronic and optical properties in monolayer GeX and SnX (X = S, Se, Te). *The Journal of Chemical Physics*, 144(11):114708, March 2016.

[145] Je-Hyeong Bahk and Ali Shakouri. Enhancing the thermoelectric figure of merit through the reduction of bipolar thermal conductivity with heterostructure barriers. *Appl. Phys. Lett.*, 105(5):052106, August 2014.

[146] David Parker and David J. Singh. Thermoelectric properties of $AgGaTe_2$ and related chalcopyrite structure materials. *Phys. Rev. B*, 85:125209, Mar 2012.

[147] Stefano Baroni, Stefano de Gironcoli, Andrea Dal Corso, and Paolo Giannozzi. Phonons and related crystal properties from density-functional perturbation theory. *Rev. Mod. Phys.*, 73:515–562, Jul 2001.

[148] B. D. Kong, S. Paul, M. Buongiorno Nardelli, and K. W. Kim. First-principles analysis of lattice thermal conductivity in monolayer and bilayer graphene. *Phys. Rev. B*, 80:033406, Jul 2009.

[149] Guangzhao Qin, Qing Bo Yan, Zhenzhen Qin, Sheng Ying Yue, Ming Hu, and Gang Su. Anisotropic intrinsic lattice thermal conductivity of phosphorene from first principles. *Phys. Chem. Chem.Phys.*, 17:4854–4858, 2015.

[150] Bo Peng, Hao Zhang, Hezhu Shao, Yuchen Xu, Xiangchao Zhang, and Heyuan Zhu. Low lattice thermal conductivity of stanene. *Sci. Rep.*, 6:20225, February 2016.

[151] S. Kumar and U. Schwingenschlogl. Thermoelectric Response of Bulk and Monolayer $MoSe_2$ and WSe_2. *Chem. Mater.*, 27:1278–1284, February 2015.

[152] J. S. Dugdale and D. K. C. MacDonald. Lattice thermal conductivity. *Phys. Rev.*, 98:1751–1752, Jun 1955.

[153] D. L. Nika, S. Ghosh, E. P. Pokatilov, and A. A. Balandin. Lattice thermal conductivity of graphene flakes: Comparison with bulk graphite. *Appl. Phys. Lett.*, 94(20):203103, May 2009.

[154] Guoxiu Wang, Xiaoping Shen, Jane Yao, and Jinsoo Park. Graphene nanosheets for enhanced lithium storage in lithium ion batteries. *Carbon*, 47(8):2049–2053, July 2009.

[155] K. S. Novoselov, V. I. Fal'ko, L. Colombo, P. R. Gellert, M. G. Schwab, and K. Kim. A roadmap for graphene. *Nat. Rev.*, 490(7419):192–200, October 2012.

[156] Yong Xu, Zuanyi Li, and Wenhui Duan. Thermal and Thermoelectric Properties of Graphene. *Small*, 10(11):2182–2199, June 2014.

[157] Andrea Splendiani, Liang Sun, Yuanbo Zhang, Tianshu Li, Jonghwan Kim, Chi-Yung Chim, Giulia Galli, and Feng Wang. Emerging Photoluminescence in Monolayer MoS_2. *Nano Lett.*, 10(4):1271–1275, April 2010.

[158] Lamuel David, Romil Bhandavat, and Gurpreet Singh. MoS_2/Graphene Composite Paper for Sodium-Ion Battery Electrodes. *ACS Nano*, 8(2):1759–1770, February 2014.

[159] Abdus Samad, Mohammad Noor-A-Alam, and Young-Han Shin. First principles study of a SnS_2/graphene heterostructure: a promising anode material for rechargeable Na ion batteries. *J. Mater. Chem. A*, 4(37):14316–14323, September 2016.

[160] Bo Peng, Hao Zhang, Hezhu Shao, Yuanfeng Xu, Xiangchao Zhang, and Heyuan Zhu. Towards intrinsic phonon transport in single-layer MoS_2. *ANNALEN DER PHYSIK*, 528(6):504–511, June 2016.

[161] Abdus Samad, Aamir Shafique, and Young-Han Shin. Adsorption and diffusion of mono, di, and trivalent ions on two-dimensional TiS 2. *Nanotechnology*, 28(17):175401, 2017.

[162] Aamir Shafique and Young-Han Shin. Thermoelectric and phonon transport properties of two-dimensional IVÃ¯Â¿Âœ @ sVI compounds. *Sci. Rep.*, 7(1):506, March 2017.

[163] Yongqing Cai, Jinghua Lan, Gang Zhang, and Yong-Wei Zhang. Lattice vibrational modes and phonon thermal conductivity of monolayer mos_2. *Phys. Rev. B*, 89:035438, Jan 2014.

[164] Wu-Xing Zhou and Ke-Qiu Chen. First-Principles Determination of Ultralow Thermal Conductivity of monolayer WSe_2. *Sci. Rep.*, 5:15070, October 2015.

[165] Xi-Bo Li, Pan Guo, Yan-Ning Zhang, Ru-Fang Peng, Hui Zhang, and Li-Min Liu. High carrier mobility of few-layer PbX (X = S, Se, Te). *J. Mater. Chem. C*, 3(24):6284–6290, June 2015.

[166] Yierpan Aierken, Deniz Cakir, and Francois M. Peeters. Strain enhancement of acoustic phonon limited mobility in monolayer tis_3. *Phys. Chem. Chem. Phys.*, 18:14434–14441, 2016.

[167] Feng Li, Xiuhong Liu, Yu Wang, and Yafei Li. Germanium monosulfide monolayer: a novel two-dimensional semiconductor with a high carrier mobility. *J. Mater. Chem. C*, 4(11):2155–2159, March 2016.

[168] Xing Zhou, Lin Gan, Wenming Tian, Qi Zhang, Shengye Jin, Huiqiao Li, Yoshio Bando, Dmitri Golberg, and Tianyou Zhai. Ultrathin SnSe_2 Flakes Grown by Chemical Vapor Deposition for High-Performance Photodetectors. *Adv. Mater.*, 27(48):8035–8041, December 2015.

[169] Haifeng Wang, Yan Gao, and Gang Liu. Anisotropic phonon transport and lattice thermal conductivities in tin dichalcogenides SnS_2 and SnSe_2. *RSC Advances*, 7:8098–8105, 2017.

[170] Yingchun Ding, Bing Xiao, Gang Tang, and Jiawang Hong. Transport Properties and High Thermopower of SnSe_2: A Full Ab-Initio Investigation. *J. Phys. Chem. C*, 121:225–236, January 2017.

[171] Appala Naidu Gandi and Udo Schwingenschlogl. Thermal conductivity of bulk and monolayer MoS_2. *EPL*, 113(3):36002, 2016.

[172] Houlong L. Zhuang and Richard G. Hennig. Theoretical perspective of photocatalytic properties of single-layer sns_2. *Phys. Rev. B*, 88:115314, Sep 2013.

[173] YuCheng Huang, Danmei Zhou, Xi Chen, Hai Liu, Chan Wang, and Sufan Wang. First-Principles Study on Doping of $SnSe_2$ Monolayers. *ChemPhysChem*, 17(3):375–379, February 2016.

[174] Dmitri K. Efetov and Philip Kim. Controlling Electron-Phonon Interactions in Graphene at Ultrahigh Carrier Densities. *Phys. Rev. Lett.*, 105(25):256805, December 2010.

[175] Bo Peng, Hao Zhang, Hezhu Shao, Yuanfeng Xu, and Heyuan Zhu. Phonon transport properties of two-dimensional group-iv materials from ab initio calculations. *Phys. Rev. B*, 94:245420, Dec 2016.

[176] Te-Huan Liu and Chien-Cheng Chang. Anisotropic thermal transport in phosphorene: effects of crystal orientation. *Nanoscale*, 7(24):10648–10654, June 2015.

[177] Nicolas Mounet and Nicola Marzari. First-principles determination of the structural, vibrational and thermodynamic properties of diamond, graphite, and derivatives. *Phys. Rev. B*, 71:205214, May 2005.

[178] D. T. Morelli and J. P. Heremans. Thermal conductivity of germanium, silicon, and carbon nitrides. *Appl. Phys. Lett.*, 81(27):5126–5128, December 2002.

[179] T. Nakashima and Y. Umakoshi. Anisotropy of electrical resistivity and thermal expansion of single-crystal Ti_5si_3. *Philos. Mag. Lett.*, 66(6):317–321, December 1992.

[180] Giorgia Fugallo, Michele Lazzeri, Lorenzo Paulatto, and Francesco Mauri. *Ab initio* variational approach for evaluating lattice thermal conductivity. *Phys. Rev. B*, 88:045430, Jul 2013.

[181] Alexander Balandin and Kang L. Wang. Significant decrease of the lattice thermal conductivity due to phonon confinement in a free-standing semiconductor quantum well. *Phys. Rev. B*, 58:1544–1549, Jul 1998.

[182] Daisuke Aketo, Takuma Shiga, and Junichiro Shiomi. Scaling laws of cumulative thermal conductivity for short and long phonon mean free paths. *Appl. Phys. Lett.*, 105(13):131901, September 2014.

[183] Samantha Bruzzone and Gianluca Fiori. Ab-initio simulations of deformation potentials and electron mobility in chemically modified graphene and two-dimensional hexagonal boron-nitride. *Appl. Phys. Lett.*, 99(22):222108, November 2011.

[184] Jinyang Xi, Mengqiu Long, Ling Tang, Dong Wang, and Zhigang Shuai. First-principles prediction of charge mobility in carbon and organic nanomaterials. *Nanoscale*, 4(15):4348–4369, July 2012.

[185] Jingsi Qiao, Xianghua Kong, Zhi-Xin Hu, Feng Yang, and Wei Ji. High-mobility transport anisotropy and linear dichroism in few-layer black phosphorus. *Nat. Commun.*, 5:4475, July 2014.

[186] Yuehua Xu, Jun Dai, and Xiao Cheng Zeng. Al_2c Monolayer Sheet and Nanoribbons with Unique Direction-Dependent Acoustic-Phonon-Limited Carrier Mobility and Carrier Polarity. *J. Phys. Chem. Lett.*, 7(2):302–307, January 2016.

[187] Joseph M. Gonzalez and Ivan I. Oleynik. Layer-dependent properties of sns_2 and $snse_2$ two-dimensional materials. *Phys. Rev. B*, 94:125443, September 2016.

[188] David M. Guzman and Alejandro Strachan. Role of strain on electronic and mechanical response of semiconducting transition-metal dichalcogenide monolayers: An ab-initio study. *J. Appl. Phys.*, 115:243701, June 2014.

[189] Xu Zhang, Xudong Zhao, Dihua Wu, Yu Jing, and Zhen Zhou. High and anisotropic carrier mobility in experimentally possible Ti_2co_2 (MXene) monolayers and nanoribbons. *Nanoscale*, 7(38):16020–16025, September 2015.

[190] Jae Hun Seol, Insun Jo, Arden L Moore, Lucas Lindsay, Zachary H Aitken, Michael T Pettes, Xuesong Li, Zhen Yao, Rui Huang, David Broido, et al. Two-dimensional phonon transport in supported graphene. *Sci.*, 328(5975):213–216, 2010.

[191] Jong-Soo Rhyee, Kyu Hyoung Lee, Sang Mock Lee, Eunseog Cho, Sang Il Kim, Eunsung Lee, Yong Seung Kwon, Ji Hoon Shim, and Gabriel Kotliar. Peierls distortion as a route to high thermoelectric performance in in^ sub 4^ se^ sub 3-[delta]^ crystals. *Nat.*, 459(7249):965, 2009.

[192] Zhenzhen Qin, Guangzhao Qin, Xu Zuo, Zhihua Xiong, and Ming Hu. Orbitally driven low thermal conductivity of monolayer gallium nitride (gan) with planar honeycomb structure: a comparative study. *Nanoscale*, 9(12):4295–4309, 2017.

[193] Jesús Carrete, Wu Li, Lucas Lindsay, David A Broido, Luis J Gallego, and Natalio Mingo. Physically founded phonon dispersions of few-layer materials and the case of borophene. *Mater. Resear. Lett.*, 4(4):204–211, 2016.

[194] Jesús Carrete, Luis J Gallego, and Natalio Mingo. Structural complexity and phonon physics in 2d arsenenes. *J. Phys. Chem. Lett.*, 8(7):1375–1380, 2017.

[195] Yongqing Cai, Gang Zhang, and Yong-Wei Zhang. Charge transfer and functionalization of monolayer inse by physisorption of small molecules for gas sensing. *J. Phys. Chem. C*, 121(18):10182–10193, 2017.

[196] Darshana Wickramaratne, Ferdows Zahid, and Roger K Lake. Electronic and thermoelectric properties of van der waals materials with ring-shaped valence bands. *J. Appl. Phys.*, 118(7):075101, 2015.

[197] A Segura, J Bouvier, MV Andrés, FJ Manjón, and V Munoz. Strong optical nonlinearities in gallium and indium selenides related to inter-valence-band transitions induced by light pulses. *Phys. Rev. B*, 56(7):4075, 1997.

[198] OZ Alekperov, MO Godjaev, MZ Zarbaliev, and RA Suleimanov. Interband photoconductivity in layer semiconductors gase, inse and gas. *Solid state communications*, 77(1):65–67, 1991.

[199] C De Blasi, G Micocci, S Mongelli, and A Tepore. Large inse single crystals grown from stoichiometric and non-stoichiometric melts. *J. Crys. Growth*, 57(3):482–486, 1982.

[200] V Zólyomi, ND Drummond, and VI Fal'ko. Electrons and phonons in single layers of hexagonal indium chalcogenides from ab initio calculations. *Phys. Rev. B*, 89(20):205416, 2014.

[201] Ransell D'Souza and Sugata Mukherjee. Length-dependent lattice thermal conductivity of single-layer and multilayer hexagonal boron nitride: A first-principles study using the Callaway-Klemens and real-space supercell methods. *Phys. Rev. B*, 96:205422, November 2017.

[202] Yongqing Cai, Jinghua Lan, Gang Zhang, and Yong-Wei Zhang. Lattice vibrational modes and phonon thermal conductivity of monolayer mos 2. *Phys. Rev. B*, 89(3):035438, 2014.

[203] Arun S Nissimagoudar, Jinlong Ma, Yani Chen, and Wu Li. Thermal transport in monolayer inse. *J. Phys.: Condens. Matter*, 29(33):335702, 2017.

[204] Aamir Shafique, Abdus Samad, and Young-Han Shin. Ultra low lattice thermal conductivity and high carrier mobility of monolayer sns 2 and snse 2: a first principles study. *Phys. Chem. Chem. Phys.*, 19(31):20677–20683, 2017.

[205] Manish Chhowalla, Hyeon Suk Shin, Goki Eda, Lain-Jong Li, Kian Ping Loh, and Hua Zhang. The chemistry of two-dimensional layered transition metal dichalcogenide nanosheets. *Nat. chem.*, 5(4):263–275, 2013.

[206] Deep Jariwala, Vinod K. Sangwan, Lincoln J. Lauhon, Tobin J. Marks, and Mark C. Hersam. Emerging Device Applications for Semiconducting Two-Dimensional Transition Metal Dichalcogenides. *ACS Nano*, 8(2):1102–1120, February 2014.

[207] Qing Hua Wang, Kourosh Kalantar-Zadeh, Andras Kis, Jonathan N. Coleman, and Michael S. Strano. Electronics and optoelectronics of two-dimensional transition metal dichalcogenides. *Nat. Nano.*, 7(11):699–712, November 2012.

[208] Abdus Samad, Aamir Shafique, Hye Jung Kim, and Young-Han Shin. Superionic and electronic conductivity in monolayer w 2 c: ab initio predictions. *J. Mater. Chem. A*, pages 11094–11099, 2017.

[209] Jiwon Chang, Leonard F. Register, and Sanjay K. Banerjee. Ballistic performance comparison of monolayer transition metal dichalcogenide MX2 (M = Mo, W; X = S, Se, Te) metal-oxide-semiconductor field effect transistors. *J. Appl. Phys.*, 115(8):084506, February 2014.

[210] Mahito Yamamoto, Sheng Tsung Wang, Meiyan Ni, Yen-Fu Lin, Song-Lin Li, Shinya Aikawa, Wen-Bin Jian, Keiji Ueno, Katsunori Wakabayashi, and Kazuhito Tsukagoshi. Strong Enhancement of Raman Scattering from a Bulk-Inactive Vibrational Mode in Few-Layer MoTe2. *ACS Nano*, 8(4):3895–3903, April 2014.

[211] Yumeng Shi, Henan Li, and Lain-Jong Li. Recent advances in controlled synthesis of two-dimensional transition metal dichalcogenides via vapour deposition techniques. *Chem. Soc. Rev.*, 44(9):2744–2756, April 2015.

[212] Michael Naguib and Yury Gogotsi. Synthesis of Two-Dimensional Materials by Selective Extraction. *Acc. Chem. Res.*, 48(1):128–135, January 2015.

[213] Claudia Ruppert, Ozgur Burak Aslan, and Tony F. Heinz. Optical Properties and Band Gap of Single- and Few-Layer MoTe2 Crystals. *Nano Lett.*, 14(11):6231–6236, November 2014.

[214] Jiong Yang, Tieyu Lu, Ye Win Myint, Jiajie Pei, Daniel Macdonald, Jin-Cheng Zheng, and Yuerui Lu. Robust Excitons and Trions in Monolayer MoTe2. *ACS Nano*, 9(6):6603–6609, June 2015.

[215] Ashish Arora, Robert Schmidt, Robert Schneider, Maciej R. Molas, Ivan Breslavetz, Marek Potemski, and Rudolf Bratschitsch. Valley Zeeman Splitting and Valley Polarization of Neutral and Charged Excitons in Monolayer MoTe2 at High Magnetic Fields. *Nano Lett.*, 16(6):3624–3629, June 2016.

[216] C. Robert, R. Picard, D. Lagarde, G. Wang, J. P. Echeverry, F. Cadiz, P. Renucci, A. Högele, T. Amand, X. Marie, I. C. Gerber, and B. Urbaszek. Excitonic properties of semiconducting monolayer and bilayer MoTe_2. *Phys. Rev. B*, 94:155425, Oct 2016.

[217] JosephÃ¯Â¿Âœ @ ER. Sootsman, DuckÃ¯Â¿Âœ @ EYoung Chung, and MercouriÃ¯Â¿Âœ @ EG. Kanatzidis. New and Old Concepts in Thermoelectric Materials. *Angew. Chem. Int. Ed.*, 48(46):8616–8639, November 2009.

[218] Ming Hu, Pawel Keblinski, and Baowen Li. Thermal rectification at silicon-amorphous polyethylene interface. *Appl. Phys. Lett.*, 92(21):211908, May 2008.

[219] Winston K. Chan. Thermal Analysis of Power Devices Wafer-Bonded to High Thermal Conductivity Substrates by Epitaxial Lift-Off. *Jpn. J. Appl. Phys.*, 37(3R):813, March 1998.

[220] Atsushi Togo and Isao Tanaka. First principles phonon calculations in materials science. *Scr. Mater.*, 108:1–5, November 2015.

[221] C. Ataca, H. Sahin, and S. Ciraci. Stable, Single-Layer MX2 Transition-Metal Oxides and Dichalcogenides in a Honeycomb-Like Structure. *J. Phys. Chem. C*, 116(16):8983–8999, April 2012.

[222] Min Kan, Hong Gi Nam, Young Hee Lee, and Qiang Sun. Phase stability and Raman vibration of the molybdenum ditelluride (MoTe 2) monolayer. *Phys. Chem. Chem. Phys.*, 17(22):14866–14871, 2015.

[223] S Jiménez Sandoval, D Yang, RF Frindt, and JC Irwin. Raman study and lattice dynamics of single molecular layers of mos 2. *Phys. Rev. B*, 44(8):3955, 1991.

[224] Ying Wang, Jun Xiao, Hanyu Zhu, Yao Li, Yousif Alsaid, King Yan Fong, Yao Zhou, Siqi Wang, Wu Shi, Yuan Wang, et al. Structural phase transition in monolayer mote2 driven by electrostatic doping. *Nat.*, pages 487–491, 2017.

[225] Renteria Jackie D., Ramirez Sylvester, Malekpour Hoda, Alonso Beatriz, Centeno Alba, Zurutuza Amaia, Cocemasov Alexandr I., Nika Denis L., and Balandin Alexander A. Strongly Anisotropic Thermal Conductivity of Free-Standing Reduced Graphene Oxide Films Annealed at High Temperature. *Advanced Functional Materials*, 25(29):4664–4672, June 2015.

[226] Martin Maldovan. Narrow Low-Frequency Spectrum and Heat Management by Thermocrystals. *Phys. Rev. Lett.*, 110(2):025902, January 2013.

[227] Zhong Yan, Guanxiong Liu, Javed M. Khan, and Alexander A. Balandin. Graphene quilts for thermal management of high-power GaN transistors. *Nat. Commun.*, 3:827, May 2012.

[228] S. Kumar, S. Sharma, V. Babar, and U. Schwingenschlögl. Ultralow lattice thermal conductivity in monolayer C3N as compared to graphene. *J. Mater. Chem. A*, 5(38):20407–20411, October 2017.

[229] Giada Basile, Cédric Bernardin, and Stefano Olla. Momentum Conserving Model with Anomalous Thermal Conductivity in Low Dimensional Systems. *Phys. Rev. Lett.*, 96(20):204303, May 2006.

[230] Denis L. Nika and Alexander A. Balandin. Two-dimensional phonon transport in graphene. *J. Phys.: Condens. Matter*, 24(23):233203, 2012.

[231] Khan M. F. Shahil and Alexander A. Balandin. Graphene–Multilayer Graphene Nanocomposites as Highly Efficient Thermal Interface Materials. *Nano Lett.*, 12(2):861–867, February 2012.

[232] H. Bae, H. Seo, S. Jun, H. Choi, J. Ahn, J. Hwang, J. Lee, S. Oh, J. U. Bae, S. J. Choi, D. H. Kim, and D. M. Kim. Fully Current-Based Sub-Bandgap Optoelectronic Differential Ideality Factor Technique and Extraction of Subgap DOS in Amorphous Semiconductor TFTs. *IEEE Trans. Electron Devices*, 61(10):3566–3569, October 2014.

[233] Patrick K. Schelling, Simon R. Phillpot, and Pawel Keblinski. Comparison of atomic-level simulation methods for computing thermal conductivity. *Phys. Rev. B*, 65(14):144306, April 2002.

[234] Ransell D'Souza and Sugata Mukherjee. First-principles study of the electrical and lattice thermal transport in monolayer and bilayer graphene. *Phys. Rev. B*, 95(8):085435, February 2017.

[235] L. Lindsay, Wu Li, Jesús Carrete, Natalio Mingo, D. A. Broido, and T. L. Reinecke. Phonon thermal transport in strained and unstrained graphene from first principles. *Phys. Rev. B*, 89:155426, April 2014.

[236] Teng Ma, Zhibo Liu, Jinxiu Wen, Yang Gao, Xibiao Ren, Huanjun Chen, Chuanhong Jin, Xiu-Liang Ma, Ningsheng Xu, Hui-Ming Cheng, and Wencai Ren. Tailoring the thermal and electrical transport properties of graphene films by grain size engineering. *Nat. Commun.*, 8:14486, February 2017.

[237] Huimin Wang, Guangzhao Qin, Guojian Li, Qiang Wang, and Ming Hu. Unconventional thermal transport enhancement with large atom mass: A comparative study of 2D transition dichalcogenides. *2D Mater.*, 5(1):015022, 2018.

[238] San-Dong Guo and Bang-Gui Liu. Ultrahigh lattice thermal conductivity in topological semimetal TaN caused by a large acoustic-optical gap. *J. Phys.: Condens. Matter*, 30(10):105701, 2018.

[239] Jiafeng Xie, Z. Y. Zhang, D. Z. Yang, D. S. Xue, and M. S. Si. Theoretical Prediction of Carrier Mobility in Few-Layer BC2N. *J. Phys. Chem. Lett.*, 5(23):4073–4077, December 2014.

[240] Lina Jiao, Meng Hu, Yusi Peng, Yanting Luo, Chunmei Li, and Zhiqian Chen. Electronic, elastic, and optical properties of monolayer BC2N. *Journal of Solid State Chemistry*, 244:120–128, December 2016.

[241] Amy Y. Liu, Renata M. Wentzcovitch, and Marvin L. Cohen. Atomic arrangement and electronic structure of bc_2n. *Phys. Rev. B*, 39:1760–1765, Jan 1989.

[242] Sumit Beniwal, James Hooper, Daniel P. Miller, Paulo S. Costa, Gang Chen, Shih-Yuan Liu, Peter A. Dowben, E. Charles H. Sykes, Eva Zurek, and Axel Enders. Graphene-like Boron–Carbon–Nitrogen Monolayers. *ACS Nano*, 11(3):2486–2493, March 2017.

[243] Changpeng Lin, Xiaoliang Zhang, and Zhonghao Rao. Theoretical prediction of thermal transport in BC2N monolayer. *Nano Energy*, 38:249–256, August 2017.

[244] M. O. Watanabe, S. Itoh, T. Sasaki, and K. Mizushima. Visible-light-emitting layered bc$_2$n semiconductor. *Phys. Rev. Lett.*, 77:187–189, Jul 1996.

[245] Aamir Shafique and Young-Han Shin. Strain engineering of phonon thermal transport properties in monolayer 2H-MoTe2. *Phys. Chem. Chem. Phys.*, 19(47):32072–32078, December 2017.

[246] Huimin Wang, Guangzhao Qin, Guojian Li, Qiang Wang, and Ming Hu. Low thermal conductivity of monolayer ZnO and its anomalous temperature dependence. *Phys. Chem. Chem. Phys.*, 19(20):12882–12889, May 2017.

List of publications

1. **Aamir Shafique** and Young-Han Shin,“Thermoelectric and phonon transport properties of two- dimensional IV-VI compounds”, *Scientific Reports*, **7** (2017) 506.
2. Abdus Samad, **Aamir Shafique**, and Young-Han Shin, “Adsorption and diffusion of mono, di, and trivalent ions on two-dimensional TiS_2”, *Nanotechnology*, **28** (2017) 175401.
3. Abdus Samad, **Aamir Shafique**, Hye Jung Kim, and Young-Han Shin, “Superionic and electronic conductivity in monolayer W_2C: ab initio predictions”, *Journal of Materials Chemistry A*, **5** (2017) 11094- 11099.
4. **Aamir Shafique**, Abdus Samad, and Young-Han Shin, “Ultra low lattice thermal conductivity and high carrier mobility of monolayer SnS_2 and $SnSe_2$: a first principles study”, *Physical Chemistry Chemical Physics*, **19** (2017) 20677-20683.
5. **Aamir Shafique** and Young-Han Shin, “Strain engineering of phonon thermal transport properties in monolayer 2H-$MoTe_2$”, *Physical Chemistry Chemical Physics*, **19**, (2017) 32072-32078.
6. **Aamir Shafique** and Young-Han Shin, “Phononic thermal transport in two-dimensional indium chalcogenide compounds (InX, X=S, Se, Te): a first principles study”. (To be submitted)
7. **Aamir Shafique** and Young-Han Shin, “Superior and anisotropic thermal transport in the hybridized monolayer (BC_2N) of boron nitride and graphene: A first-principles study”. (To be submitted)